MEASUREMENT OF THE SURFACE TENSION OF ELECTROMAGNETICALLY-LEVITATED DROPLETS IN MICROGRAVITY

by

Elliot M. Schwartz

Submitted to the Department of Materials Science and Engineering in Partial Fulfillment of the Requirements for the degree of

DOCTOR OF PHILOSOPHY

in Materials Engineering
at the

Massachusetts Institute of Technology

February, 1995

© Massachusetts Institute of Technology 1995
All rights reserved

Signature of Author _____
Department of Materials Science and Engineering
January 13, 1995

Certified by _____
Julian Szekely
Professor of Materials Engineering
Thesis Supervisor

Accepted by _____
Carl V. Thompson II
Professor of Electronic Materials
Chair, Departmental Committee on Graduate Students

MASSACHUSETTS INSTITUTE
OF TECHNOLOGY

JUL 20 1995

LIBRARIES Science

MEASUREMENT OF THE SURFACE TENSION OF ELECTROMAGNETICALLY-LEVITATED DROPLETS IN MICROGRAVITY

by

Elliot M. Schwartz

Submitted to the Department of Materials Science and Engineering on January 13, 1995, in partial fulfillment of the requirements for the degree of Doctor of Philosophy in Materials Engineering

ABSTRACT

The viscosity and surface tension of liquid metals are important properties, both from a scientific and a technological point of view. Conventional techniques involve contact with the liquid whose properties are being measured, resulting in contamination and making undercooling impossible. For these reasons electromagnetic levitation was used to position, heat, and deform the samples in a containerless fashion. In order to eliminate the turbulent fluid flow inherent in earthbound levitation experiments to make viscosity measurement possible and determine the effect of magnetic fields on surface tension measurements, the experiments were performed in microgravity as part of the IML-2 Space Shuttle mission in July 1994. In order to rationally plan these experiments, a substantial mathematical modeling effort was performed. We have developed a computational methodology and calculated the levitation forces, stirring forces, and deformation of the sample through the solution of Maxwell's electromagnetic field equations and the Navier-Stokes equations for fluid flow with due allowance for a boundary condition of normal stress continuity at the free surface. The temperature distribution in a levitated droplet has also been calculated through the solution of the differential thermal energy balance equation including the power induced in the sample and heat lost from the surface by radiation and conduction. These predictive calculations were essential for both the planning of the experiments and for the replanning of experimental runs during the actual Space Shuttle mission. The results of surface tension measurements for three different materials made aboard the Space Shuttle are also presented.

Thesis Supervisor: Professor Julian Szekely

Title: Professor of Materials Engineering

TABLE OF CONTENTS

Abstract 2

Table of Contents 3

List of Figures 5

List of Tables 9

Acknowledgements 11

1. Introduction 13
   - 1.1 Purpose 13
   - 1.2 Viscosity and Surface Tension 15
   - 1.3 Electromagnetic Levitation 21
   - 1.4 Property Measurements Using Levitation 22
   - 1.5 Oscillation of a Freely-Floating Droplet 24
   - 1.6 Need for Microgravity 31
   - 1.7 TEMPUS Containerless Processing Facility 32
   - 1.8 Mathematical Modeling 33
   - 1.9 History and Achievements of the Project 35
   - 1.10 Organization 38
   - 1.11 References 39

2. Electromagnetic Calculations 52
   - 2.1 Introduction 52
   - 2.2 Analytical Calculations 53
   - 2.3 Method of Mutual Inductances 55
   - 2.4 Improvements to Method 61
   - 2.5 Calculation of Electromagnetic Quantities 64
   - 2.6 Results 65
   - 2.7 Acknowledgements 70
   - 2.8 References 70

3. On the Shape of Liquid Metal Droplets in Electromagnetic Levitation Experiments 83
   - Abstract 83
   - 3.1 Introduction 83
   - 3.2 Formulation and Computational Methodology 84
   - 3.3 Experimental Work 91
   - 3.4 Computed Results 93
   - 3.5 Discussion 94
   - 3.6 Acknowledgements 95
   - 3.7 References 95

4. The Free Surface Shape and Temperature Distribution Produced in Liquid Metal Droplets by Heating Coil Pulses in the TEMPUS EML 105
Abstract 105
4.1 Introduction 105
4.2 Formulation and Computational Methodology 107
4.3 Computed Results 114
4.4 Discussion 116
4.5 Acknowledgements 118
4.6 References 118

5. The Shape of Liquid Metal Droplets in Electromagnetic Levitation Experiments Considering Internal Fluid Flow 132
Abstract 132
5.1 Introduction 132
5.2 Formulation and Computational Methodology 134
5.3 Computed Results 139
5.4 Discussion 141
5.5 Acknowledgements 143
5.6 References 143

6. Surface Tension Measurements on Liquid Metals in Microgravity 151
Abstract 151
6.1 Introduction 151
6.2 Experimental 153
6.3 Results 156
6.4 Discussion 157
6.5 Conclusions 159
6.6 Dynamic Nucleation 160
6.7 Acknowledgements 161
6.8 References 162

7. Concluding Remarks 171

Biographical Note 175

LIST OF FIGURES

1.1 Surface tension values for liquid iron near its melting point as a function of year. From Iida and Guthrie [1.2], p. 113. Methods of surface tension measurement: ∘ Sessile drop, ◻ Maximum bubble pressure, Δ Pendant drop, ▼ Oscillating drop, • Drop weight. Data from Allen (1972b); Murarka, Lu, and Hamielec (1975); Kawai and Mori (1979); Ogino, Nogi, and Yamase (1980). p. 44

1.2 Viscosity of liquid iron, as determined by a number of workers. From Iida and Guthrie [1.2], p. 168. ------- Values obtained by workers in the USSR. (1) Arsentiev et al., (2) Barfield and Kitchener, (3) Nobohatskii et al., (4) Romanov and Kochegarov, (5) Samarin, (6) Ogino et al., (7) Ogino et al., (8) Nakanishi et al., (9) Vatolin et al., (10) Frohberg and Cakici, (11) Cavalier, (12) Saito and Watanabe, (13) Lucas, (14) Kawai et al., (15) Thiele, (16) Avaliani et al., (17) Wen Li-shi and Arsentiev, (18) Schenck et al., (19) Frohberg and Weber, (20) Narita and Onoe, (21) Krieger and Trenkler. (after Iida and Morita 1980). p. 45

1.3 Schematic diagram of (a) separate positioning and heating coil systems and (b) coil geometry of TEMPUS electromagnetic containerless processing facility. Figures provided by I. Egry et al. p. 46

1.4 Sketch of (a) quadrupole magnetic field produced by TEMPUS positioning coils and (b) dipole magnetic field produced by TEMPUS heating coils. Figures provided by G. Lohoefer. p. 47

2.1 Discretization of droplet domain, showing exponential grid point distribution and rectangular cross section of annular circuit elements. p. 72

2.2 Illustration of geometrical parameters used in Lyle's method for calculating mutual inductances between rectangular coils. From [11]. p. 73

2.3 Magnetic flux density distribution calculated for test case of the "flux ball", a sphere with windings on its surface that have uniform turns density with respect to the z-axis. p. 74

2.4 Conical coil arrangement used to levitate copper sample at German Aerospace Research Establishment (DLR). p. 75

2.5 Magnetic flux density distribution calculated for actual shape of copper droplet levitated in DLR conical coil arrangement. p. 76

2.6 Electromagnetic force distribution calculated for actual shape of copper droplet levitated in DLR conical coil arrangement. p. 77

2.7 Schematic diagram of coil geometry of TEMPUS electromagnetic containerless processing facility (dimensions in mm). Inner four coils are heating coils and outer eight coils are positioning coils. Figure provided by I. Egry et al. p. 78

2.8 Magnetic flux density distribution calculated for spherical sample of copper in TEMPUS positioning coil field. p. 79

2.9 Magnetic flux density distribution calculated for spherical sample of copper in TEMPUS heating coil field. p. 80

2.10 Electromagnetic force distribution calculated for spherical sample of copper in TEMPUS positioning and heating coil fields. p. 81

3.1 Schematic diagram of TEMPUS system with separate (a) positioning and (b) heating coil systems. Figure provided by I. Egry et al. p. 98

3.2 Discretization of droplet domain, showing exponential grid point distribution and rectangular cross section of annular circuit elements. p. 99

3.3 Conical coil arrangement with field strength and gradient along symmetry axis for peak applied current of I_0=405 A. p. 100

3.4 Fit of spherical harmonics to experimental shape. p. 101

3.5 Comparison of calculated and experimental Cu droplet shapes. p. 102
..... Spherical shape
— Experimentally-determined shape
---- Calculated deformed shape

3.6 Comparison of calculated and experimental Ni droplet shapes. p. 103
..... Spherical shape
— Experimentally-determined shape
---- Calculated deformed shape

4.1 Schematic cut-through of TEMPUS coil geometry (distances in mm). Inner four coils produce dipole field for heating and deforming samples. Outer eight coils produce quadrupole for positioning. Figure provided by I. Egry et al. p. 120

4.2 Geometrical representations of coils as (a) single heating coil band and (b) two cylindrical bands composed of coils above and below sample

for view factor and radiosity calculations to compare absorbed power to emitted power. p. 121

4.3 Calculated equilibrium free surface shapes of 10 mm diameter Cu sample levitated in TEMPUS with heating coil voltages of 0 V (solid line), 2 V (dashed line), 3.5 V (dotted line), and 5 V (dashdot line). Positioning coil voltage is 6 V for all cases. The percentage deformation for each case appears in Table 4.2. p. 122

4.4 Calculated equilibrium free surface shapes of 8 mm diameter $Au_{56}Cu_{44}$ sample levitated in TEMPUS with heating coil voltages of 0 V (solid line), 2 V (dashed line), 3.5 V (dotted line), and 5 V (dashdot line). Positioning coil voltage is 6 V for all cases. The percentage deformation for each case appears in Table 4.2. p. 123

4.5 Calculated equilibrium free surface shapes of 8 mm diameter Au sample levitated in TEMPUS with heating coil voltages of 0 V (solid line), 2 V (dashed line), 3.5 V (dotted line), and 5 V (dashdot line). Positioning coil voltage is 6 V for all cases. The percentage deformation for each case appears in Table 4.2. p. 124

4.6 Calculated equilibrium free surface shapes of 10 mm diameter Ni sample levitated in TEMPUS with heating coil voltages of 0 V (solid line), 2 V (dashed line), 3.5 V (dotted line), and 5 V (dashdot line). Positioning coil voltage is 6 V for all cases. The percentage deformation for each case appears in Table 4.2. p. 125

4.7 Calculated temperature vs. time profiles at center, top, and equator of 10 mm diameter Cu sample during and after 3 V heating coil pulse of 0.1 s duration in TEMPUS. Analytical results provided for comparison. Maximum temperature difference calculated is 2.19°C. p. 126

4.8 Calculated temperature vs. time profiles at center, top, and equator of 8 mm diameter $Au_{56}Cu_{44}$ sample during and after 3 V heating coil pulse of 0.1 s duration in TEMPUS. Analytical results provided for comparison. Maximum temperature difference calculated is 2.81°C. p. 127

4.9 Calculated temperature vs. time profiles at center, top, and equator of 8 mm diameter Au sample during and after 3 V heating coil pulse of 0.1 s duration in TEMPUS. Analytical results provided for comparison. Maximum temperature difference calculated is 3.25°C. p. 128

4.10 Calculated temperature vs. time profiles at center, top, and equator of 10 mm diameter Ni sample during and after 3 V heating coil pulse of 0.1 s duration in TEMPUS. Analytical results provided for comparison. Maximum temperature difference calculated is 5.59°C. p. 129

4.11 Calculated isotherms in 10 mm Ni sample at end of 3 V heating coil pulse of 0.1 s duration in TEMPUS. Maximum temperature is at equator (isotherm J) and minimum temperature is at top and bottom (isotherm A). p. 130

5.1 Conical coil arrangement with field strength and gradient along symmetry axis for peak applied current of I_0=405 A. p. 145

5.2 Streamline pattern (left side) and velocity vector field (right side) for equilibrium shape of Ni droplet calculated using EM-driven flow model with Re=1. Magnitude of maximum velocity is 1.39 cm/s and extent of deformation is 7.55%. p. 146

5.3 Streamline pattern (left side) and velocity vector field (right side) for equilibrium shape of Ni droplet calculated using EM-driven flow model with Re=10. Magnitude of maximum velocity is 14.51 cm/s and extent of deformation is 9.13%. p. 147

5.4 Streamline pattern (left side) and velocity vector field (right side) for equilibrium shape of Ni droplet calculated using EM-driven flow model with Re=25. Magnitude of maximum velocity is 25.48 cm/s and extent of deformation is 12.55%. p. 148

5.5 Comparison of results for Ni droplet shapes. p. 149
—— Experimentally-determined (10.22% def.)
+++ Normal stress balance model (6.84% def.)
----- EM-driven flow model, Re=1 (7.55% def.)
..... EM-driven flow model, Re=10 (9.13% def.)
-.-.- EM-driven flow model, Re=25 (12.55% def.)

6.1 Schematic sketch of the TEMPUS experimental arrangement showing main subsystems. p. 164

6.2 Plot of temperature (jagged line), heating coil control voltage (plot at bottom), and positioning coil control voltage (constant value of 5000 mV) vs. time for cycle 6 of $Zr_{64}Ni_{36}$ experiment. p. 165

6.3 Video still of two frames of the side view of the oscillating $Zr_{64}Ni_{36}$ droplet. The visible portion of the droplet is flat at the top and the bottom because of the obstruction provided by the heating coils. The

obstruction from the sample cage wires causes the vertical lines. The cross hairs come from the camera. p. 166

6.4 Frequency spectrum for surface tension measurement of $Au_{56}Cu_{44}$. The peaks in the region of 0-5 Hz come from translational oscillations. The high peak at about 15 Hz is the surface oscillation peak used to measure the surface tension. The peak at 30 Hz comes from the commercial frame rate. p. 167

6.5 Surface tension data for liquid Au, with linear fit of the data points. For the purpose of comparison, the "1 g-results" are uncorrected data obtained by Sauerland et al. [6.15] in earthbound levitation experiments. The "1 g-results extrapolated to 0 g" are surface tension values obtained using the Cummings and Blackburn correction formula. p. 168

6.6 Surface tension data for liquid $Au_{56}Cu_{44}$, with linear fit of the data points. p. 169

6.7 Surface tension data for liquid $Zr_{64}Ni_{36}$, with linear fit of the data points. p. 170

LIST OF TABLES

1.1 Widely-used models for viscosity of liquid metals p. 48

1.2 Conventional surface tension measurement techniques p. 49

1.3 Conventional viscosity measurement techniques p. 50

1.4 Principal investigators (PIs) and experiments on TEMPUS IML-2 p. 51

2.1 Comparison of versions of code used to calculate Joule heating in Ni sphere p. 82

3.1 Expansion coefficients of $R(\psi)$ for fit of experimental shape with spherical harmonics p. 104

3.2 Comparison of experimental and theoretical splitting of oscillation modes p. 104

3.3 Input parameters used for equilibrium free surface shape calculations p. 104

4.1 Material properties used in calculations p. 131

4.2 Calculated equilibrium free surface shapes p. 131

5.1 Input parameters for equilibrium free surface shape calculations p. 150

5.2 Percentage deformation and magnitude of maximum velocity for actual and calculated Ni droplet shapes p. 150

ACKNOWLEDGEMENTS

I would like to first thank my thesis advisor, Professor Julian Szekely, for providing me with an incredible research project and the opportunity to work on a Space Shuttle experiment. I appreciate the confidence he showed in me by allowing me to travel and participate in all phases of the project. Finally, I would like to thank him for his numerous suggestions throughout the years of my graduate study and for helping me establish contacts in the field.

I would like to thank Professor Markus Zahn of the Department of Electrical Engineering and Computer Science for serving on my thesis committee and his useful suggestions regarding my work as a whole.

I would like to thank Professor Thomas Eagar for agreeing to serve on my thesis committee at such short notice.

I would like to thank Professor Stuart Brown for serving on my thesis committee during most of my time in graduate school. I would like to thank him for his thoughtful suggestions regarding my work and especially for taking an interest in the development of my career.

I would like to thank Professor and Department Chairman Merton Flemings for his interest in my progress throughout my years in the department and especially for providing the financial support that made it possible for me to present my first technical paper at the TMS Annual Meeting in San Diego in 1992.

I would like to thank Prof. Dr. Ivan Egry of the German Aerospace Research Establishment (DLR) in Cologne, Germany, for serving as my host during several visits to his laboratory, for his friendship and interest in my work, and for taking me to my first German soccer game.

I would like to thank Prof. Andreas Alexandrou of WPI for many useful discussions about my work, great assistance in my search for employment, and encouragement in general.

I would like to thank former and present members of the Materials Process Modeling Group for many useful discussions over the years, especially my officemate, Dr. Livia Racz.

I would like to thank my oldest and best friends in Germany, Mrs. Angelika Diefenbach, Dr. Stefan Sauerland, and Dr. Stefan Diefenbach, for their hospitality during my many visits to DLR, collaboration on various projects, encouragement and help in learning German, and especially, their friendship.

I would like to thank Dr. Georg Lohoefer of DLR for many useful discussions and quick responses to my e-mail questions regarding my work, and Mr. Gerd Jacobs and Mr. Jin Kim for their hard work and friendship.

I would like to acknowledge the financial support of the Department of Defense through the National Defense Science and Engineering Graduate Fellowship for the first three years of my graduate study.

I would like to thank the National Aeronautics and Space Administration for their financial support of the research and the opportunity to perform experiments aboard the Space Shuttle Columbia from the ground in Huntsville, as well as personally aboard the KC-135 aircraft.

I would like to thank the approximately forty members of Team TEMPUS throughout the United States and Germany for their cooperation and teamwork, as well as IML-2 Astronaut Dr. Don Thomas for his "greeting from space".

I would like to thank my many students in the course 3.185, "Transport Phenomena in Materials Processing", and in the tutoring program of the Office of Minority Education for providing me with the opportunity to teach, work, and learn with them.

I would like to extend special thanks to Ms. Candace Royer, MIT women's varsity tennis coach, for helping me to develop a love of tennis through hours of lessons and the opportunity to work with her and the players as an assistant coach.

I would like to thank the many residents at Next House, 500 Memorial Drive, especially housemasters Prof. Bora Mikic and Mrs. Liba Mikic, longtime house manager Mr. George Hosker, and fellow Graduate Resident/Tutor Mrs. Linda Becker, for providing a great deal of fun, comfort, and food to the often lonely life of a graduate student.

I extend my thanks to all of my friends who helped give me a life at MIT outside of work: my oldest and best friends from my undergraduate years, Mr. Stephen Pao and Mr. Laird Malamed, my weight training partners, Mr. Stephen Terry and Mr. Michail Tryfonidis, and my friends Mr. Paul Boisselle and Mr. Byron Cortez, for providing much support, many lessons about life, and the realization that the best part of life need not involve schoolwork.

Most importantly I would like to thank my parents, Mr. and Mrs. Gordon and Yvette Schwartz, and my brother, Mr. Jeffrey Schwartz, for their love, understanding, and patience throughout my life and especially during my years at MIT. My parents provided me with the opportunity to attend MIT and the belief that I could persevere and succeed.

CHAPTER 1

INTRODUCTION

1.1 PURPOSE

This research program was undertaken with the goal of using the unique attributes of microgravity to measure the viscosity and surface tension of liquid metals in the superheated and undercooled states. Because of the need to operate in an efficient manner, mathematical models are being increasingly used to predict behavior and intelligently control industrial materials processing operations. The accuracy of the results produced by such mathematical models is limited by the accuracy of thermophysical property data such as the viscosity and surface tension. The property database for liquid metals in the superheated and undercooled states is incomplete and the conventional measurement techniques are not entirely satisfactory, providing motivation for the development and execution of the microgravity experiments.

The thermophysical properties were measured in a containerless fashion with the oscillating drop technique by using electromagnetic levitation. In order to be able to rationally plan the experiments to be performed on the IML-2 Space Shuttle mission in July 1994, a substantial mathematical modeling effort was performed. These predictive calculations were essential for both the planning of the experiments and for the re-planning of experimental runs during the actual Space Shuttle mission [1].

Mathematical modeling is becoming increasingly common in materials processing to obtain a quantitative understanding of the phenomena that govern materials processing operations. Microgravity, or Space Shuttle, experimentation represents a specific case in point; the very high cost of the Space Shuttle flights, the very limited flight opportunities that are available, the tight resources in the Spacelab, and a justifiably skeptical public clearly mandate that these experiments be very precisely planned and that all possible opportunities for mathematical modeling be fully exploited [1].

The contents of this thesis detail the methodology and results of the mathematical modeling effort conducted for the design of a series of Space Shuttle experiments. The major achievement of the work is that we were able to perform the first very accurate surface tension measurements on liquid metals that did not require the used of correction formulae. The fact that we were able to successfully perform these experiments in space with an apparatus that had never previously been used in a Spacelab mission illustrates the strength of the mathematical modeling effort.

The main contributions in the field of process modeling described in this thesis are:

(1) Improvement of a code to calculate the electromagnetic field and forces in an axisymmetric droplet of arbitrary cross-section

(2) Development of a model of the free surface shape of a levitated droplet involving re-calculation of the magnetic pressure distribution as the shape changed

(3) Development of a model of the free surface shape of a levitated droplet that simultaneously considers the internal electromagnetically-driven fluid flow

(4) Development of a model of the heat transfer in a levitated droplet considering the spatially-varying induced power and heat losses at the surface

The mathematical models detailed in this thesis were in large part developed for and applied to the particular electromagnetic levitation device used to perform the microgravity experiments. In addition to being useful for determining the optimal parameter set to run the experiments performed with the TEMPUS EML, the models developed are already being applied to the design of the next generation of EMLs, which may be used to perform thermophysical property measurements aboard the Space Station.

There are is also the potential for this work to make a significant contribution to the optimization and development of industrial processes. The techniques developed for modeling the behavior of levitation-melted metallic droplets could also be readily adapted to tackling a broad range of problems where the surfaces of molten metals are being shaped, deformed, or simply held in

position through the application of electromagnetic forces; some current applications of these techniques include electromagnetic casting, electromagnetic dams in near net shape casting applications, and the moldless melting of titanium. While major advances are being made in the application of electromagnetic theory to advancing our understanding of these systems, it is possible that the techniques described here could find applications in these areas as well [1].

1.2 VISCOSITY AND SURFACE TENSION

Surface tension is defined thermodynamically as the surface free energy required to create a surface of given area and has units of J/m^2. The dynamic definition views the surface as a membrane that exists under a uniform tension, and the surface tension is regarded as the force required to stretch this membrane by a given distance. In this case the surface tension has the SI units of N/m, which is equivalent to the units of the surface free energy [2-3].

Viscosity is a measure of a fluid's resistance to applied motion. The Newtonian definition of viscosity is that it is the constant of proportionality between the shear force exerted per unit area and the velocity gradient in the fluid. On a microscopic level, viscosity is a measure of the friction among atoms within a fluid [3].

The surface tension and viscosity of fluids are important properties, both from a scientific and a technological point of view [4]. Interest in the viscosity and the surface tension of molten metals and alloys stems both from scientific considerations, because understanding these properties is essential to validating the theories of the liquid state, and from practical considerations, such as their applications in processing, chemical, and metallurgical industries [5].

Surface tension and viscosity are critical in casting, molding, and crystal growth operations such as in preparing turbine blades for jet engines [6]. In smelting and refining operations, the surface tension is a key parameter in phenomena such as gas absorption, nucleation of gas bubbles, nucleation and growth of non-metallic inclusions, and slag/metal reactions. Other

metallurgical processes such as casting, brazing, sintering, zone refining, and fiber formation are also greatly influenced by the surface tension of the liquid metal being processed [3]. The surface tension is also interesting for technological reasons because it strongly influences the processing behavior of molten metals. Through doping with surface-active substances such as sulfur, oxygen, selenium, and tellurium the surface tension of liquid metals can be altered, which can create better properties upon welding, soldering, and casting [2].

Viscosity plays an important role in the solution of quantitative problems in fluid flow behavior and the kinetics of reactions in metallurgical processes. For example, the viscosity of a liquid metal is a main factor in determining the speed at which small gas bubbles and non-metallic inclusions rise through it [3]. In undercooled metals and, in particular, in glass-forming systems, the viscosity changes by 14 orders of magnitude in a temperature range of approximately 500 K between melting and glass temperature. For high undercooling the viscosity μ reduces the nucleation rate I drastically because it is inversely proportional to the viscosity [7], as seen from the relationship [8]

$$I \propto \frac{1}{\mu} \exp\left[-\frac{16\pi\gamma_{SL}^3}{3kT(\Delta G_v)^2} \right] \tag{1.1}$$

where γ_{SL} is the solid-liquid interfacial energy, k is Boltzmann's constant, T is the Kelvin temperature, and ΔG_v is the difference in free energies per unit volume of solid and liquid. The reduced nucleation rate makes it possible to produce metallic glasses, materials with amorphous structures, at high undercooling [9].

The surface tension and the viscosity also influence fluid flow processes in the melt. Marangoni convection is driven along the melt surface by gradients in the surface tension. The dimensionless number associated with this phenomenon is the Marangoni number [8]

$$Ma = \frac{\left|\vec{\nabla}T\right| L^2}{\alpha\mu} \frac{\partial\gamma}{\partial T} \tag{1.2}$$

where $\left|\vec{\nabla}T\right|$ is the magnitude of the temperature gradient, L is the characteristic length, $d\gamma/dT$ is the rate of change surface tension with respect to temperature, and α is the thermal diffusivity of the melt. Control of Marangoni convection in the melt is important in such processes as welding and single crystal growth [2].

With the advent of powerful mathematical modeling techniques for metallurgical phenomena, there is renewed interest in reliable data on the physical properties of liquid metals. Presently, the knowledge and accuracy of these data are the limiting factors in the models [10]. Egry et al. [4] used expressions developed by Fowler [11] and Born and Green [12] to derive a simple relation between the surface tension γ and the viscosity μ of a pure liquid. They argued that such a relation exists because the surface tension and the viscosity relate to the same microscopic process. When additional surface is created, the surface atoms are displaced with respect to each other, and work must be done against their pair potential. Egry et al. demonstrated that the integrals in the expressions derived by Fowler and Born and Green were equal and, by forming the ratio γ/μ, obtained the relationship

$$\frac{\gamma}{\mu} = \frac{15}{16}\sqrt{\frac{kT}{m}} \tag{1.3}$$

where k is Boltzmann's constant, T is the Kelvin temperature, and m is the atomic mass.

Egry et al. checked the validity of this relationship by compiling published data for some liquid metals and found that the error was less than 20%, which is about the accuracy of the input data, over a general temperature range of 300 K around the melting point. The relationship developed by Egry has been found by several researchers and works remarkably well for noble and transition metals near their melting points [13]. Egry et al. indicated that the striking feature of their results was that the experimental data seemed to obey

the linear relationship between γ/μ and $T^{1/2}$ very well. This was thought to be surprising because the generally accepted formulae for the temperature dependence of the surface tension and viscosity for liquid metals at temperatures above the melting point

$$\gamma(T) = \gamma(T_m) + (d\gamma / dT)(T - T_m) \tag{1.4}$$

$$\mu(T) = \mu_o e^{A/RT} \tag{1.5}$$

where T_m is the melting temperature, μ_o is the pre-exponential, A is the activation energy, and R is the gas constant, would yield an essentially Arrhenius-type temperature behavior for γ/μ. Egry et al. suggested that their findings could be taken as an argument to support recent mode-coupling theories that predict a power-law behavior of the viscosity at moderate undercoolings [4].

A great deal of research has been done in constructing models of the liquid state, but the viscosity of molten metals has defied predictions from first principles due to inadequate understanding. Most of the currently available theories draw parallels either with solid-like and/or gas-like behavior, and none has been entirely successful. In addition, all models currently in use rely on empirical or semi-empirical formulations rather than proven theory [5].

Numerous relationships have been developed to depict the temperature dependence of the viscosity of liquid metals. Many have been used successfully over narrow ranges of temperature. Chhabra and Sheth [5] discussed and compared three widely-used models under extensive ranges of temperature. These models are summarized in Table 1.1. The Arrhenius equation for viscosity gives excellent fit to the data over a limited temperature range, but significant departures have also been reported. Hildebrand's free volume theory envisions that the fluid flow is simply governed by the extent of free space available. The relationship has been shown to accurately describe the temperature dependence of the viscosity of a wide range of materials including molten metals. Based on a quasi-crystalline model of the liquid state, Andrade proposed an expression for the viscosity of liquid metals that has been found by many investigators to fit experimental

data for liquid metals with a high degree of accuracy. Chhabra and Sheth concluded that the Arrhenius and the Andrade equations were virtually indistinguishable, whereas the Hildebrand fluidity model yielded slightly poorer results, but was thought to be more appropriate for the interpolation of data. They concluded that is was not yet possible to choose one particular predictive equation as the equation because the deviations between the actual and calculated values are well within the limits of experimental uncertainty.

Battezzati and Greer [14] compiled a large body of published data on the viscosity of liquid metals and alloys. With the exception of liquids showing strong association and good glass-formers, they found that the melting-point viscosity is described well by the Andrade formula and that the temperature dependence of the viscosity above the melting point in Arrhenius. They also asserted that for glass-forming systems the temperature dependence of the viscosity is best fitted by the empirical Vogel-Fulcher-Tammann equation. This model is also summarized in Table 1.1.

The measurement of thermophysical properties of liquid metals is an active field of research. However, almost all existing data concern the liquid state above the melting temperature. Information on the temperature dependence of viscosity and surface tension of liquid metals in the undercooled regime is not available to date and it would complement existing data on liquid metals at and above their melting point. Data on thermophysical properties of undercooled metallic melts is very poor, largely because standard invasive measurement techniques usually induce nucleation of the stable solid phase, making it extremely difficult to work with this metastable state. There are also experimental difficulties posed by the high degree of chemical reactivity of these melts [7].

The surface tensions of most liquid metals have been measured, but due to the aforementioned difficulties in measurement, there is much scatter among the available data [15]. According to Iida and Guthrie [3], mercury is the only metal whose surface tension is accurately known. The surface tensions of liquid metals, particularly those with high melting points and/or those which are chemically reactive, have yet to be established. For example, surface tension data for liquid iron still exhibit considerable scatter, as indicated in

Figure 1.1. In general the surface tension values for liquid metals near their melting points tends to increase over a period of years, presumably approaching their true values. This is supported by the fact that the extent of scatter, which is attributed mainly to reduced impurities and surface contamination, decreases with time. Reviews have been given by Keene [16] for iron and its binary alloys and by Nogi et al. [17] for transition metals.

Published surface tension data for the undercooled state of pure Fe, Ni, and Au were found to be linear extrapolations of the data obtained for the liquid phase. Mills et al. [18] measured surface tension values for undercoolings of up to 300 K for nickel and found that the temperature dependence of the surface tension in the undercooled state appeared to be identical with that recorded for the liquid phase. This was also found to be the case for measurements with iron and gold. Values of the surface tension and its temperature dependence obtained in the investigation performed by Sauerland et al. [19] for Fe, Ni, and Au were in good agreement with the results obtained by conventional techniques. Although this suggested that contamination of the samples in conventional methods from metal/ceramic reactions was not large for these metals, this may not be the case for more reactive metals such as Si or Ti.

Numerous experimental measurements of liquid metal viscosities have been made, but accurate and reliable data have been difficult to obtain. As can be seen in Figure 1.2, which shows experimental viscosity data for liquid iron, discrepancies as large as thirty to fifty per cent exist between the experimental results of different researchers. A major reason for large discrepancies among viscosity data obtained using the oscillating-vessel method, which has been used most extensively for liquid metals and alloys, is the result of approximations in the working formulae used to calculate the viscosity of the liquid from the observed damping of oscillations and dimensions of the apparatus. Additional difficulties in obtaining reliable viscosity data for liquid metals are the same as for the surface tension--high reactivity of liquid metals and the technical difficulty of taking precise measurements at high temperatures [3].

1.3 ELECTROMAGNETIC LEVITATION

Electromagnetic processing of materials can be utilized to process electrically-conducting materials in a clean containerless environment. Electromagnetic fields are used to control the shape of a body of molten metal through magnetic pressure on the free surface in processes such as vertical continuous casting, the cold crucible technique, and in making thin films of molten metal. Application of electromagnetic fields is also used in such diverse processes as driving fluid flow and fluid flow suppression (electromagnetic valves), as a non-intrusive velocity sensor, and as an alternative to mechanical stirring [20].

Levitation melting has been part of the process metallurgist's repertoire for several decades. In this process a metallic droplet, usually 5-10 mm in diameter, is suspended by electromagnetic forces generated by the passage of a radio-frequency current through induction coils which are located above and below the droplet. The electromagnetic (Lorentz) force is generated by the interaction of the currents that are induced in the droplet with the applied magnetic field. The irrotational component of the electromagnetic force provides the lifting force, while the rotational component provides stirring and internal fluid flow if the sample is molten. The induced current also provides Joule heating through Ohmic losses, hence the commonly-used term "levitation melting".

The electromagnetic levitation technique is a widespread method for containerless processing of liquid metals. A major advantage of the method is the avoidance of sample contamination through the use of high-purity processing gas and contact-free measuring techniques. Work with very reactive molten metals is thereby possible without concern for falsification of measured results due to chemical reaction with the crucible material. A further advantage comes from the avoidance of heterogeneous nucleation on container walls, making it possible to work in the metastable regime of undercooled melts [2].

1.4 PROPERTY MEASUREMENTS USING LEVITATION

Surface tension measurements have traditionally been performed using the sessile-drop and pendant-drop techniques, both of which are based on the determination of the non-spherical equilibrium shapes of drops due to surface tension and gravity [21]. These techniques are based on the measurement of the shape or size of a droplet that is located on a substrate or suspended on a wire. The surface tension is then determined from the numerical solution of a differential equation expressing a force balance at the free surface of the sessile drop. In the maximum bubble pressure method the pressure needed to make bubbles against the surface tension in the melt is measured. In all of these conventional methods, the melt is always in contact with a substrate, which presents the following disadvantages [2]:

(1) Because of the high chemical reactivity of metals at high temperatures, contamination of the sample surface by the substrate is virtually impossible to avoid.

(2) Investigation of undercooled melts is impossible because the substrate serves as a nucleation site for solidification.

(3) Evaluation of the measured data requires knowledge of the density, but reliable density data currently exist only for common low-melting-point metals and their alloys [3].

In addition, the precision of measurements made using the sessile drop and pendant drop methods are limited by the accuracy and reproducibility in reading the coordinates of the drop profile [22]. A list of the conventional surface tension measurement techniques, summarized from a comprehensive account by Iida and Guthrie [3], is given in Table 1.2.

There are few suitable techniques for determination of the viscosity of liquid metals and alloys because of their low viscosities, high chemical reactivities, and high melting points. According to Iida and Guthrie [3], it is very difficult to state definitely the accuracy of viscosity measurements for liquid metals and errors range from one per cent to twenty per cent for all but a few metals. As a result, there are not many well-established data for liquid metal viscosities.

Conventional measurement techniques, including the oscillating-vessel method and the oscillating-plate method, use observation of the oscillations of a vessel containing the fluid of interest about a vertical axis. A list of these techniques, condensed from Iida and Guthrie, is given in Table 1.3. In addition to the mathematical difficulty of solving the differential equation of motion for the system, the contact of the liquid metal with a container presents the same problems as do conventional surface tension measurement techniques [3].

In 1971 Fraser et al. [23] developed a method to measure the surface tension of liquid metals in a containerless fashion, the oscillating drop technique using electromagnetic levitation. Further developments were made by Soda et al. [24], Keene et al. [25], and Egry et al. [8]. In this technique, the oscillations of a levitated droplet about its equilibrium shape are observed. The restoring force for surface oscillations is the surface tension, which can be related to the frequency of the oscillations [26]. In the levitated drop technique the solid sample is placed in a high-frequency, inhomogeneous magnetic field which is chosen in such a way that it simultaneously melts the sample by induction and compensates for gravity through the applied Lorentz force [15,19].

This method has the advantage of eliminating persistent sources of contamination which arise through the use of substrates and/or capillary tubes associated with the sessile drop, the capillary rise, and the maximum bubble pressure methods [3]. It avoids any contact with a crucible and thus reduces not only systematic errors due to surface contamination but also allows deep undercooling of the liquid metal [27].

Surface tensions of metals are markedly dependent on the concentrations of surface-active elements such as the group VI elements, O, S, Se, and Te. For example, 50 ppm O causes a 30% increase in the surface tension of iron. With conventional methods the reaction of the liquid metal with oxide ceramic containers leads to oxygen contamination of the melt and subsequently to low values for the surface tension. Since the levitated drop method eliminates this source of contamination, it obviously has distinct advantages over conventional methods of measuring surface tension [18].

There has been some skepticism about the results obtained by the levitated drop method since this method tends to yield higher values for the surface tension than those from conventional techniques. Although some authors have attributed this to the better purity of the sample's surface, it may also be a systematic error due to the presence of the electromagnetic levitation field. This field produces a magnetic pressure at the surface and leads to an apparent increase of the surface tension. Measurements were carried out at two establishments, the German Aerospace Research Establishment (DLR) in Cologne, Germany, and the National Physical Laboratory (NPL) in Teddington, England, in order to investigate the effects of variations in the magnetic field and the sample weight on surface tension values with the intention of presenting an improved evaluation scheme that would eliminate this false magnetic pressure effect. Corrections for the effect of magnetic pressure on the apparent surface tension obtained using a relation derived by Cummings and Blackburn [28] gave surface tension values which were independent of sample mass and in agreement with values derived by conventional techniques [19]. Their work demonstrated that the levitated drop method could produce very accurate results and would be the preferred method for determining the surface tensions of reactive metals [15].

1.5 OSCILLATION OF A FREELY-FLOATING DROPLET

Viscosity and surface tension can be measured by exciting and detecting surface oscillations of a levitated droplet [29]. The theory of oscillations of viscous spheroids is a classical problem in hydrodynamics which has received considerable attention over the years. The surface tension of the sample is related to the oscillation frequency, and the viscosity is related to the damping of the oscillations [29].

The radius of a spherical droplet undergoes damped oscillations of the form [26]

$$R_{n,m}(\theta,\phi,t) \sim \cos(2\pi\nu_{n,m}t)e^{-\Gamma_{n,m}t}P_n^m(\cos\theta)\cos[m(\phi-\phi_o)] \tag{1.6}$$

where n is the index of the fundamental oscillation modes, m is the index of

one of the 2n-1 possible modes ($|m| \leq n$), θ is the angle with respect to the symmetry axis, ϕ is the azimuthal angle, $\nu_{n,m}$ and $\Gamma_{n,m}$ are the frequency and damping constant for the given mode, P_n^m is an associated Legendre function, and ϕ_0 is an arbitrary symmetry direction [21].

Lord Rayleigh calculated the frequencies of small-amplitude oscillations of an inviscid spherical liquid droplet of mass m due to surface tension γ. The relationship between the frequency of mode n and the surface tension is given by [30]

$$\nu_n = \sqrt{\frac{1}{3\pi} n(n-1)(n+2)\frac{\gamma}{m}} \tag{1.7}$$

Due to the spherical symmetry of the droplet considered in his derivation, Rayleigh predicted a complete degeneration of the states, whereby oscillation mode n has exactly 2n+1 possible oscillation modes with the same frequency. Equation 1.7 was confirmed by Lamb [31], who calculated the influence of "small" viscosity on the oscillations. He concluded that the oscillation frequencies were not changed and that a damping of the oscillations appeared. The damping constant is given by

$$\Gamma_n = (n-1)(2n+1)\frac{\mu}{R^2\rho} \tag{1.8}$$

where R is the radius of the spherical droplet.

There is only one oscillation mode corresponding to the index n=0. For m=0

$$R_{0,0}(\theta,\phi,t) = a_0(t) \tag{1.9}$$

This oscillation mode consists of isotropic expansion or contraction of the sphere and is known as the "breathing mode". Because of the conservation of volume associated with incompressible fluids, this oscillation mode is not observed in the case of liquid metal droplets.

For the index n=1 the three possible distortions of the sphere correspond to the indices m = -1, 0, +1. The expressions for the shape for each mode are given by

$$R_{1,0}(\theta,\phi,t) = a_0 + a_{1,0}(t)\cos\theta \tag{1.10}$$

$$R_{1,+1}(\theta,\phi,t) = a_0 + a_{1,+1}(t)\sin\theta\cos\phi \tag{1.11}$$

$$R_{1,-1}(\theta,\phi,t) = a_0 + a_{1,-1}(t)\sin\theta\sin\phi \tag{1.12}$$

By considering the expressions for the Cartesian coordinates x, y, and z in spherical coordinates

$$z = r\cos\theta \tag{1.13}$$

$$x = r\sin\theta\cos\phi \tag{1.14}$$

$$y = r\sin\theta\sin\phi \tag{1.15}$$

it can be realized that the distortions expressed mathematically in Equations 1.10-1.12 represent movement of the entire sample in each of the coordinate directions and are therefore translational oscillations.

There are five possible deformations of a sphere for the index n=2. In all cases the equilibrium shape is a sphere. The expressions for the droplet shape in the cases of m = -2, -1, 0, +1, +2 are given by

$$R_{2,0}(\theta,\phi,t) = a_0 + \frac{1}{2}a_{2,0}(t)(3\cos^2\theta - 1) \tag{1.16}$$

$$R_{2,+1}(\theta,\phi,t) = a_0 + 3a_{2,+1}(t)\sin\theta\cos\theta\cos\phi \tag{1.17}$$

$$R_{2,-1}(\theta,\phi,t) = a_0 + 3a_{2,-1}(t)\sin\theta\cos\theta\sin\phi \tag{1.18}$$

$$R_{2,+2}(\theta,\phi,t) = a_0 + 3a_{2,+2}(t)\sin^2\theta\cos(2\phi) \tag{1.19}$$

$$R_{2,-2}(\theta,\phi,t) = a_0 + 3a_{2,-2}(t)\sin^2\theta\sin(2\phi) \tag{1.20}$$

In one half-period of the n=2, m=0 mode the sample expands in the z-direction and contracts at the equator, and in the other half-period the sample contracts in the z-direction and expands at the equator. The main characteristic of this mode is that it is perfectly symmetric to the z-axis. The top view of the projection of this mode is fully axisymmetric and each plane

through the z-axis in the side view is a mirror plane. The plane perpendicular to the z-axis, which passes through the center of mass, is also a mirror plane.

The n=2, m=+1 and n=2, m=-1 modes are nicknamed the "peanut modes" or the "tumbling modes" because from the side view the droplet swings back and forth between the diagonals. This mode is not symmetric with respect to the z-axis. In the top view the projection has no rotational symmetry, while in the side view only the x-z plane is a mirror plane.

Like the n=2, m=0 mode, the n=2, m=+2 and n=2, m=-2 modes are symmetric with respect to the z-axis. In the top view of the sample there is no rotational symmetry, but in the side view the x-z and y-z planes are mirror planes. In particular, the z-axis is a mirror axis for every side view of the sample [2].

From Equation 1.7 it can be seen that the surface tension γ is related to the minimum possible natural oscillation frequency ν (mode n=2) by the expression

$$\gamma = \frac{3}{8}\pi m \nu_2^2 \tag{1.21}$$

The viscosity of the melt μ is related to the oscillation amplitude decay constant Γ for the mode n=2 through the expression

$$\mu = \frac{1}{5}R^2\rho\Gamma_2 \tag{1.22}$$

For a non-rotating spherical droplet, the n=2 modes are five-fold degenerate. If the equilibrium shape is not spherical but still axisymmetric and the sample does not rotate, the frequencies depend on $|m|$ only, and the spectrum has three peaks which correspond to m = 0, ± 1, ± 2 [21]. For the case of small axisymmetric deviations from a spherical shape Cummings and Blackburn [28] derived expressions for the oscillation frequencies of n=2 modes m=0, m=± 1, and m=± 2

$$\nu_{2,0} = \nu_R(1 - 0.6758\varepsilon_2 - 2.176\varepsilon_4) \tag{1.23}$$

$$\nu_{2,\pm1} = \nu_R(1 - 0.3379\varepsilon_2 + 1.4507\varepsilon_4) \tag{1.24}$$

$$\nu_{2,\pm2} = \nu_R(1 + 0.6758\varepsilon_2 - 0.3627\varepsilon_4) \tag{1.25}$$

where ν_R is the Rayleigh frequency, which can be obtained by setting n=2 in Equation 1.7 [2]. The terms ε_2 and ε_4 are coefficients in the series of spherical harmonics used to fit the curve that describes the shape of the levitated droplet, which is given by [32]

$$R(\theta) = R_0\left(1 + \sum_{n=1} \varepsilon_n Y_n^0(\theta)\right) \tag{1.26}$$

According to Cummings and Blackburn, for observations of the droplet down the z-axis ("side view"), the intensity of the n=2, m=0 and n=2, m=$\pm$2 modes will be greater than that for the n=2, m=$\pm$1 modes. They also predicted that the spacings between the three bands in the frequency spectrum are in the ratio of 3:1 when the deformation of the droplet has only a second-spherical-harmonic (Y_2^0) component. From Equations 1.23-1.25 it can be calculated that for a purely second-spherical-harmonic extent of deformation of 10%, as was approximately the case in the microgravity experiment, the maximum frequency shift relative to the undistorted sphere is about 10.7%.

A rotating and/or non-axisymmetric sample exhibits all five peaks, corresponding to modes m=-2, -1, 0, +1, and +2 [21]. In practice the rotational symmetry of the magnetic field is not perfect because it is impossible to produce perfectly symmetric coils. The resulting inhomogeneity of the magnetic field and the fact that the sample shape is not spherical create additional external forces on the sample that can lead to sample rotation. Busse [33] derived a simple formula for the splitting of oscillation modes in a rotating inviscid incompressible fluid caused by sample rotations to first order in the rotational frequency Ω. According to Busse, rotation influences only $m \neq 0$ modes, as seen from the relation

$$\nu_{n,m}^{\Omega} = \nu_{n,m}^{0} + \frac{m}{2}\frac{\Omega}{2\pi} \tag{1.27}$$

where $\nu^{\Omega}_{n,m}$ is the oscillation frequency considering rotation of the sample. Equation 1.27 predicts that the splitting of the oscillation frequencies is symmetric, with the difference in frequency between the frequency in the case of no rotation and that considering rotation depending on the rotational frequency and the index of the oscillation mode [2].

In order to determine the correct Rayleigh frequency, which is needed to calculate the surface tension from the measured oscillation frequencies, Cummings and Blackburn [28] and Suryanarayana and Bayazitoglu [34] have developed summation rules and corrections to account for the magnetic field. Cummings and Blackburn have calculated the effect of asphericity, gravity, magnetic field, and sample rotation on the frequency of the n=2 modes of an incompressible and inviscid droplet. The main result of their calculation is that the frequency of the fundamental n=2 mode is split into up to five sidebands.

In order to derive an expression for the Rayleigh frequency in terms of the surface and translational oscillation frequencies that would account for the magnetic field, Cummings and Blackburn assumed that the z-component of the magnetic field strength varied linearly with z. Based on the equation derived by Egry and Sauerland [13] from the work of Cummings and Blackburn, the correction formula

$$\nu_R^2 = \frac{1}{5}\left(\nu_{2,0}^2 + 2\nu_{2,\pm1}^2 + 2\nu_{2,\pm2}^2\right) - 1.9\overline{\nu_1^2} - 1.92\times10^{-4}\frac{1}{\overline{\nu_1^2}}\left(\frac{g}{R}\right)^2 \tag{1.28}$$

allows the corresponding Rayleigh frequency to be evaluated from the observed frequencies of the fundamental and translational modes. Subtraction of the terms including the mean-square translational frequency

$$\overline{\nu_1^2} = \frac{1}{3}\left(2\nu_{1,\pm1}^2 + \nu_{1,0}^2\right) \tag{1.29}$$

accounts for the apparent increase in surface tension due to the action of the applied magnetic field. The magnetic field correction in the formula presented by Cummings and Blackburn has two effects. It eliminates a false

mass dependence of the surface tension inherent in previous results obtained by the oscillating drop technique, and it reduces the absolute value of the surface tension [13].

If the field strength is chosen correctly, there is an equilibrium point along the symmetry axis at which the Lorentz force cancels the gravitational force exactly. This is the equilibrium position of the droplet. In an electromagnetic quadrupole field, the droplet experiences a restoring force as soon as it deviates from its equilibrium position. This leads to translational oscillations of the droplet as a whole, that is, to the appearance of the n=1 mode [19].

Rayleigh's approach does not account for translational (n=1) oscillations because such a distortion is connected to movement of the center of gravity of the sphere, which comes from an external potential rather than surface tension and is not considered in Rayleigh's Lagrange formulation. In order to derive an expression for the frequency of n=1 oscillation modes, Rayleigh's approach must be extended. This is done by introducing a potential energy term that corresponds to the restoring force with spring constant k into the Lagrange formulation [2]. For a sample of mass m the oscillation frequency ν_1 is given by [21]

$$\nu_1 = \frac{1}{2\pi}\sqrt{\frac{k}{m}} \tag{1.30}$$

The spring constant k is proportional to the magnitude of the gradient of the electromagnetic force field. When the magnetic field varies linearly in the z-direction, the translational frequency in that direction will always be exactly twice that of the translations in the x- and y-directions [28].

Bratz and Egry [35] derived a correction formula to account for the effect of gravity the electromagnetic field on the damping of the n=2 oscillation modes in an axisymmetric droplet. The corrections for individual n=2 modes are on the order of 5-10%, but the important result was that the average damping constant for the n=2 oscillation modes is the same as that derived by Lamb [31].

1.6 NEED FOR MICROGRAVITY

Surface tension measurements made with the oscillating drop technique using electromagnetic levitation can be improved by performing the experiments in a microgravity environment. Residual accelerations aboard the Space Shuttle are on the order of one thousand to one hundred thousand times less than the magnitude of gravitational acceleration on the earth, therefore, much weaker electromagnetic fields are necessary. This offers three primary benefits to surface tension measurements.

(1) The sample remains nearly spherical, which greatly facilitates the analysis of the oscillations. As discussed above, non-sphericity results in splitting of the n=2 oscillation modes, which complicates the analysis.

(2) The magnetic pressure on the surface of the sample, which leads to an apparent increase in the surface tension and has often been neglected in surface tension measurements made using the oscillating drop technique, is reduced.

(3) The induced currents in the sample are reduced, which makes it possible to minimize the heat induced in the sample, thereby making processing in ultra-high vacuum and at lower temperatures feasible [7,21].

Microgravity is necessary for the performance of viscosity measurements using the oscillating drop technique. The need to operate in a microgravity environment can be justified by the consideration that under earthbound conditions, quite strong electromagnetic lifting forces are needed to overcome gravity; under these conditions the stirring forces are also strong and result in turbulent or transitional fluid flow within the droplet. Turbulence makes the measurement of the viscosity impossible because momentum transfer and the decay of the oscillations are then governed by the turbulent eddies rather than by the molecular viscosity. Furthermore, the minimization of the magnetic positioning fields made possible by experimentation in microgravity greatly reduces the magnetic damping of oscillations which dominates viscous damping in ground-based experiments [7].

1.7 TEMPUS CONTAINERLESS PROCESSING FACILITY

The experiments run to measure the viscosity and surface tension at various temperatures in the stable liquid and undercooled liquid states were conducted using TEMPUS (Tiegelfreies Elektromagnetisches Prozessieren Unter Schwerelosigkeit), the electromagnetic containerless processing facility. TEMPUS uses electromagnetic levitation for containerless positioning and heating of metal samples and can be used under microgravity conditions. Schematic sketches of the TEMPUS facility and the coil geometry are shown in Figures 1.3(a) and 1.3(b), respectively. TEMPUS was designed to process 8 mm and 10 mm diameter spherical metal samples within two sets of induction coils. The outer (positioning) coils, which operate at a frequency of about 140 kHz and create a quadrupole magnetic field, illustrated in Figure 1.4(a), position the sample. The inner (heating) coils, which operate at a frequency of about 400 kHz and create a dipole magnetic field, illustrated in Figure 1.4(b), provide most of the thermal energy to the sample through induction (Joule) heating [36].

By switching off or reducing the heating field, the power input into the sample can be greatly reduced, thereby allowing undercooling without forced gas cooling of the sample. In addition, a short voltage pulse through the heating coil can be used to excite the surface oscillations. Most metals can be positioned against 0.01 g_0 and heated up to 2500°C with only 1.5 kW. TEMPUS is equipped with a two-color pyrometer measuring between 300 and 2500°C with a sampling rate of 1 MHz. Two video cameras (standard CCIR monochrome) offer top and side views of the sample. The facility can operate under inert purified gas atmosphere (Ar, He) and ultra-high vacuum (10^{-9} mbar) [21].

TEMPUS was built by Dornier, a company based in Friedrichshafen, Germany, under contract from DARA, the German space agency. Some of the hardware and software in TEMPUS were designed based on the inputs of the eight teams of investigators, including our team, but the Space Shuttle experiments were essentially performed using an apparatus that we did not build. As a result, a significant part of our work prior to the mission was the

determination of the set of parameters which configured the generic main process flow for the performance of our particular experiments. The parameter set included such variables as the emissivity for temperature measurement, inert gas pressure, heating and positioning coil voltages, heating times, maximum and minimum allowable sample temperatures, and heating coil pulse voltage and duration. This preparation consisted of the mathematical modeling effort detailed in this thesis and experimentation with the Development Model of TEMPUS at the Microgravity User Support Centre in Cologne, Germany.

In the experiment, the solid sample was introduced from below into the space within the coils. The positioning coils were turned on first, and once the sample rested in a stable position, the heating coils were turned on to melt the sample and bring it to a predetermined, desired temperature above the melting point. The current through the heating coils was then substantially reduced to allow the sample to cool for a predetermined amount of time. The sample was squeezed and deformed by applying a significantly higher current through the heating coils for 0.1 s. After the heating coil was switched off again, the damped oscillations of the droplet were observed and recorded on video for a period of 5 s, during which time the sample continued to cool by conduction to the surrounding inert gas and by radiation. The pulsing and observation procedure was repeated until the droplet solidified in order to obtain thermophysical property measurements over a temperature range which would include temperatures in both the superheated and undercooled states [1].

1.8 MATHEMATICAL MODELING

Because TEMPUS is not able to levitate and process samples under earthbound conditions, the amount of experimental preparation for the Space Shuttle experiments was greatly limited. For this reason, a comprehensive mathematical modeling effort was essential. Electromagnetic levitation of liquid metals presents three coupled problems--the determination of the magnetic field, the unknown free surface shape, and the internal fluid motion [37].

The first mathematical descriptions of this method, based on the theory of Okress [38] and Rony [39], depended on the assumption that the external magnetic field in the area of the sample only varies slightly. The expressions for the time-averaged force and time-averaged absorbed power that they derived are only applicable when the diameter of the sample is small compared to the dimensions of the coil system [2].

The exact description of the force and absorbed power of a metal sample in an alternating magnetic field involves solution of the quasistatic Maxwell equations with infinite series expansions. With this type of solution the induced eddy currents and the time-averaged levitation force and absorbed power distributions can be calculated [2]. Lohoefer [40-41] developed analytical expressions for the total power absorption and forces produced in an electromagnetically-levitated metal sphere. El-Kaddah and Szekely [42] presented a mathematical representation for the electromagnetic force field, fluid flow field, and temperature field in a levitation-melted metal droplet.

Sneyd and Moffatt [37] attempted to solve the coupled problem for two-dimensional liquid metal cylinders, but only in situations where one of the three phenomena could be neglected. Mestel [43] treated the coupled problem for the single-frequency case by considering cases in which one of the three phenomena could be neglected. Gagnoud, Etay, and Garnier [44] presented two iterative methods for computing the equilibrium free surface shape, one based on satisfying a stress equilibrium condition at the free surface, the other based on energy minimization, but both of these methods considered only the surface of the droplet and ignored the interior. El-Kaddah and Acosta-Gonzalez [45] presented a mathematical model for the coupled problem of determination of the electromagnetic force field and free surface shape, but also neglected the interior. Gagnoud and Leclercq [46] decoupled the velocity field and the equilibrium free surface shape.

Zong, Li, and Szekely [47] combined a numerical technique for calculating the electromagnetic force field with a commercial fluid flow package to calculate the steady-state melt velocities. Zong, Li, and Szekely [48] subsequently presented results describing the transient evolution of the velocity and

temperature fields in a sample levitated in the TEMPUS EML after the application of the heating coil pulse.

Numerical studies of cases involving arbitrary viscosity and small-amplitude oscillations [49], small-to-moderate inviscid oscillations [50], large-amplitude inviscid oscillations [51], and large-amplitude oscillations [52] have been performed.

The mathematical modeling effort that we used to rationally plan the successful Space Shuttle experiments addressed the following issues:

(i) calculation of the lifting and stirring forces and power dissipation from first principles

(ii) calculation of the internal fluid flow fields

(iii) calculation of the sample deformation when the squeezing force is applied

(iv) calculation of the transient development of the temperature fields within the sample, as affected by power dissipation and heat transfer to the surroundings

As the subsequent chapters will show, the modeling effort was vital to our ability to plan and replan the successful experiments performed during the IML-2 Space Shuttle mission. In addition to the fundamental significance of the research, the computational methodology and tools developed to model the electromagnetic fields and forces, internal fluid flow, free surface shape, and heat transfer of samples processed in TEMPUS is readily applicable to emerging electromagnetic materials processing operations [20].

1.9 HISTORY AND ACHIEVEMENTS OF THE PROJECT

The funding for this project began in February 1990, but the conception of the experiment and initial preparation began several years before that. The author of the thesis first became involved in this project in January 1988 through the Undergraduate Research Opportunities Program (UROP) at MIT, initially performing a literature search to confirm the feasibility of measuring the surface tension and viscosity of molten metals through the oscillating drop technique.

In addition to the mathematical modeling effort performed at MIT, the preparation for the Space Shuttle experiment involved work with NASA and cooperation with the various parties involved with TEMPUS, including members from NASA, DARA, Dornier, MUSC, and the other Principal Investigator (PI) teams, a group including about forty people from the United States and Germany. The eight PIs, their affiliations, and the experiments are listed in Table 1.4.

Throughout the project we have collaborated most closely with Prof. Ivan Egry and his research group at the German Aerospace Research Establishment (DLR) in Cologne, Germany. Members of each research group have spent significant periods of time in the laboratories of the other group. The author of the thesis had the opportunity to spend two months at DLR in the summer of 1990 working on the development of image processing techniques for the evaluation of the oscillations of levitated molten metal droplets. Through practice with the German members of the TEMPUS team and study at MIT, it was possible for the author to communicate entirely in German during the month in the fall of 1994 spent at DLR evaluating the data obtained from the Space Shuttle experiments.

In May 1994 the author had the opportunity to participate in experiments with the Development Model of TEMPUS aboard NASA's KC-135 parabolic flight aircraft, which provides about twenty seconds of low-gravity conditions for each parabolic maneuver. In addition to gaining valuable knowledge about the behavior of the levitated samples and the apparatus in a reduced gravity environment prior to the IML-2 mission, the author had the chance to experience weightlessness with the astronauts who would be conducting the TEMPUS experiments aboard the Space Shuttle Columbia.

The experiments took place from July 8 to July 23, 1994, aboard the Space Shuttle Columbia as part of the Spacelab IML-2 (Second International Microgravity Laboratory) mission. During that time we monitored our experiments from the Payload Operations Command Center (POCC) at NASA's Marshall Space Flight Center in Huntsville, Alabama. From there, we telecommanded our experiments and coordinated experimental runs with the other TEMPUS PI teams [53].

Collaboration among the scientists assembled at the POCC was an especially gratifying aspect of the trip. From the very beginning, the PI teams combined their efforts and resources to maximize the science output of the mission. In particular, we shared samples and performed experiments of different types on the same sample. During the mission, this spirit of cooperation was vital to overcoming the problems that we encountered. The two primary problems faced were heavy contamination of the samples, which greatly limited the amount of undercooling that could be attained, and sample instability, as off-center positioning of the samples due to imperfect electromagnetic field alignment caused many of the molten samples to collide with the surrounding sample cage. leading to premature termination of many experiments [54].

All of the TEMPUS experiments pertaining to thermophysical property measurements were performed jointly by the Szekely and Egry groups. Prior to the mission experiments on noble metals Au and Cu, the alloy AuCu, and Ni had been planned. The experiments on Au and AuCu were performed successfully based on the preparation before the mission, much of which was based on the knowledge gained from the mathematical modeling effort. A successful experiment was also conducted on a ZrNi sample previously used by one of the other PI teams for heat capacity measurements. The experiment was entirely planned during the mission based on the experience and teamwork of the two groups.

At the time of the submission of this thesis, surface tension values for Au, AuCu, and ZrNi had been obtained, and plots of surface tension vs. temperature in the superheated state were generated. These results appear in Chapter 6. The results agree very well with available data and theoretical predictions and suggested that microgravity experimentation is the optimal platform for thermophysical property measurements.

Viscosity results had not yet been attained, due to the time necessary to perfect the data evaluation technique. Preliminary results suggested that the damping of the oscillations was an order of magnitude greater than what should have come from the molecular viscosity. The source of this result was being investigated, but it is possible that the brief heating coil pulses used

to squeeze the molten samples induced transitional or turbulent fluid flow in the samples, which would account for the enhanced damping.

An unexpected side result also obtained from the ZrNi experiment was the suggestion of a phenomenon known as dynamic nucleation. In order to excite oscillations from which the properties could be measured, brief current pulses were applied to the molten sample. In many cycles during the ZrNi experiment, the first current pulse in the undercooled state coincided with the onset of nucleation (solidification), indicating that the current pulses may have triggered nucleation without any contact with the sample. More analysis is required to confirm the occurrence of this phenomenon, but it seems that we have proven the existence of this effect [54].

The overall program was very successful, especially in light of the fact that IML-2 was the first Space Shuttle mission for the experimental apparatus TEMPUS. The success of the experiment is a testimony to the power of mathematical modeling, which made it possible to properly plan key aspects of the experiment and to re-plan experiments during the mission in response to the problems that were faced. The very accurate surface tension results show that the Space Shuttle provides the optimal environment for high-quality thermophysical property measurements. The work leading up to the mission, participating in testing of TEMPUS in microgravity on KC-135 parabolic flights, and commanding experiments from the NASA Payload Operations Command Center during the mission was truly a once-in-a-lifetime experience.

1.10 ORGANIZATION

Each of the following five chapters details one portion of the mathematical modeling effort. It is intended that each chapter can stand on its own and that each can be useful without reading the entire thesis from beginning to end. It is hoped that this will be useful to readers with interest in a particular aspect of the work presented.

In Chapter 2 we discuss the modifications made to an existing code used to calculate the electromagnetic fields and forces and power dissipated in an

axisymmetric sample. The formulation and results of the normal stress balance model, a mathematical model developed to calculate the equilibrium free surface shape effected by the brief squeezing pulse, are detailed in Chapter 3. In Chapter 4 we present the results of free surface shape and heat transfer calculations intended to assess the effects of the squeezing pulse on various samples. In Chapter 5 we discuss the formulation and results of the electromagnetically-driven flow model, which was used to simultaneously calculate the internal fluid flow field and free surface shape. In Chapter 6 we describe the series of IML-2 Space Shuttle experiments performed in July 1994, in particular, the results of the surface tension measurements. Concluding remarks and recommendations for continuing the work described in Chapters 1-6 are presented in Chapter 7.

Chapter 3, with minor differences, has been published, with co-authors S. Sauerland, J. Szekely, and I. Egry, in the proceedings of the symposium Containerless Processing: Techniques and Applications, which was held at the 1993 TMS Annual Meeting. Chapter 5, with minor differences, has been published, with co-author J. Szekely, in the proceedings of the symposium Experimental Methods for Microgravity Materials Science, which was held at the 1994 TMS Annual Meeting. Chapters 4 and 6 will be submitted for publication in refereed journals.

1.11 REFERENCES

[1] E. Schwartz and J. Szekely, "Mathematical Modeling: An Essential Component of the Design of Space Experiments", to be published in proceedings of Materials Processing in the Computer Age II, TMS, Las Vegas (1995).

[2] S. Sauerland, Messung der Oberflaechenspannung an levitierten fluessigen Metalltropfen, Ph.D. Thesis, DLR Cologne/University of Aachen, Germany (1993).

[3] T. Iida and R. I. L. Guthrie, The Physical Properties of Liquid Metals, Clarendon Press, Oxford, England (1988).

[4] I. Egry, G. Lohoefer, and S. Sauerland, "Surface tension and viscosity of liquid metals", Journal of Non-Crystalline Solids, 156-158 (1993), 830-832.

[5] R. P. Chhabra and D. P. Sheth, "Viscosity of Molten Metals and its Temperature Dependence", Zeitschrift fuer Metallkunde, 81 (1990) 264-271.

[6] J. L. Margrave, "Determination of thermophysical properties of liquid metals at high temperatures by levitation methods", Materials Science and Engineering, A178 (1994), 83-88.

[7] I. Egry and J. Szekely, "The Measurement of Thermophysical Properties in Microgravity Using Electromagnetic Levitation", Adv. Space Res., 11(7) (1991), 263-266.

[8] I. Egry, G. Lohoefer, P. Neuhaus, and S. Sauerland, "Surface Tension Measurements of Liquid Metals Using Levitation, Microgravity, and Image Processing", International Journal of Thermophysics, 13(1) (1992), 65-74.

[9] D. Turnbull, "Under What Conditions can a Glass be Formed?", Contemp. Phys., 10(5) (1969), 473-488.

[10] I. Egry, "On the Relation between Surface Tension and Viscosity for Liquid Metals", Scripta Metallurgica et Materialia, 28 (1993) 1273-1276.

[11] R. H. Fowler, "A Tentative Statistical Theory of Macleod's Equation for Surface Tension, and the Parachor", Proceedings of the Royal Society of London, A159 (1937), 229-246.

[12] M. Born and H. S. Green, "A general kinetic theory of liquids--III. Dynamical properties", Proceedings of the Royal Society of London, A190 (1947), 455-474.

[13] I. Egry and S. Sauerland, "Containerless processing of undercooled metals: measurements of surface tension and viscosity", Materials Science and Engineering, A178 (1994), 73-76.

[14] L. Battezzati and A. L. Greer, "The Viscosity of Liquid Metals and Alloys", Acta Metallurgica, 37(7) (1989), 1791-1802.

[15] S. Sauerland, G. Lohoefer, and I. Egry, "Surface Tension Measurements on Levitated Aspherical Liquid Nickel Drops", 11th Symposium on Thermophysical Properties, Boulder, Colorado, 1991.

[16] B. J. Keene, "Review of data for the surface tension of iron and its binary alloys", International Materials Reviews, 33(1) (1988), 1-37.

[17] K. Nogi, K. Ogino, A. McLean, and W. A. Miller, "The Temperature Coefficient of the Surface Tension of Pure Liquid Metals", Metallurgical Transactions, 17B (1986), 163-170.

[18] K. C. Mills and R. F. Brooks, "Measurements of thermophysical properties in high temperature melts", Materials Science and Engineering, A178 (1994), 77-81.

[19] S. Sauerland, R. F. Brooks, I. Egry, and K. Mills, "Magnetic Field Effects on the Oscillation Spectrum of Levitated Drops", Containerless Processing: Techniques and Applications, TMS, Denver (1993), 65-69.

[20] E. Schwartz, Measurement of Viscosity of Undercooled Melts Under Microgravity Conditions, Doctoral Thesis Proposal, 1991.

[21] I. Egry, "Surface tension measurements of liquid metals by the oscillating drop technique", Journal of Materials Science, 26 (1991), 2997-3003.

[22] R. Sangiorgi, G. Caracciolo, and A. Passerone, "Factors limiting the accuracy of measurements of surface tension by the sessile drop method", Journal of Materials Science, 17 (1982), 2895-2901.

[23] M. E. Fraser, W-K. Lu, A. E. Hamielec, and R. Murarka, "Surface Tension Measurements on Pure Liquid Iron and Nickel by an Oscillating Drop Technique", Metallurgical Transactions, 2 (1971), 817-823.

[24] H. Soda, A. McLean, and W. A. Miller, "The Influence of Oscillation Amplitude on Liquid Surface Tension Measurements with Levitated Metal Droplets", Metallurgical Transactions, 9B (1978), 145-147.

[25] B. J. Keene, The use of a Fourier Analyser for Determination of the Surface Tension of Liquid Metals by the Levitating Drop Technique, NPL Report DMA(A) 56, NPL, Teddington, UK (1982).

[26] W. H. Reid, "The Oscillations of a Viscous Liquid Drop", Quarterly of Applied Mathematics, 18 (1960), 86-89.

[27] R. Willnecker, D. M. Herlach, and B. Feuerbacher, "Containerless processing of bulk Fe-Ni melts", Applied Physics Letters, 49(20) (1986), 1339-1341.

[28] D. L. Cummings and D. A. Blackburn, "Oscillations of magnetically levitated aspherical droplets", Journal of Fluid Mechanics, 224 (1991) 395-416.

[29] I. Egry, B. Feuerbacher, G. Lohoefer, and P. Neuhaus, "Viscosity Measurement in Undercooled Metallic Melts", VIIth European Symposium on Materials and Fluid Sciences in Microgravity, Oxford, UK (1989).

[30] J. W. S. Rayleigh, "On the Capillary Phenomena of Jets", Proceedings of the Royal Society of London, 29 (1879), 71-97.

[31] H. Lamb, "On the Oscillations of a Viscous Liquid Globe", Proceedings of the London Math. Society, 13(1) (1881), 51-66.

[32] E. Schwartz and J. Szekely, "The Shape of Liquid Metal Droplets in Electromagnetic Levitation Experiments Considering Internal Fluid Flow", Experimental Methods for Microgravity Materials Science, TMS, San Francisco (1994), 73-79.

[33] F. H. Busse, "Oscillations of a rotating liquid drop", Journal of Fluid Mechanics, 142 (1984), 1-8.

[34] P. V. R. Suryanarayana and Y. Bayazitoglu, "Effect of static deformation and external forces on the oscillations of levitated droplets", Physics of Fluids A, 3(5) (1991), 967-977.

[35] A. Bratz and I. Egry, "Surface Oscillations of Electromagnetically Levitated Viscous Metal Droplets", submitted to Journal of Fluid Mechanics.

[36] J. H. Zong, J. Szekely, and G. Lohoefer, "Calculations and Experiments Concerning Lifting Force and Power in TEMPUS", Acta Astronautica, 29(5) (1993), 371-378.

[37] A. D. Sneyd and H. K. Moffatt, "Fluid Dynamical Aspects of the Levitation-Melting Process", Journal of Fluid Mechanics, 117 (1982), 45-70.

[38] E. C. Okress, D. M. Wroughton, G. Comenetz, P. H. Brace, and J. C. R. Kelly, "Electromagnetic Levitation of Solid and Molten Metals", Journal of Applied Physics, 23 (1952), 545-552.

[39] P. R. Rony, "The Electromagnetic Levitation of Metals", Trans. Vacuum Met. Conference, Am. Vacuum Society, Boston (1965), 55-135.

[40] G. Lohoefer, "Theory of an Electromagnetically Levitated Metal Sphere I: Absorbed Power", SIAM Journal of Applied Mathematics, 49(2) (1989), 567-581.

[41] G. Lohoefer, "Force and Torque of an Electromagnetically Levitated Metal Sphere", Quarterly of Applied Mathematics, 51 (1993), 495-518.

[42] N. El-Kaddah and J. Szekely, "The Electromagnetic Force Field, Fluid Flow Field, and Temperature Profiles in Levitated Metal Droplets", Metallurgical Transactions, 14B (1983), 401-410.

[43] A. J. Mestel, "Magnetic Levitation of Liquid Metals", Journal of Fluid Mechanics, 117 (1982), 27-43.

[44] A. Gagnoud, J. Etay, and M. Garnier, "The Levitation Melting Process Using Cold Crucible Technique", Transactions ISIJ, 28 (1988), 36-40.

[45] N. El-Kaddah and F. A. Acosta-Gonzalez, "Mathematical Model for the Shaping of Molten Metal by an Electromagnetic Field", Casting of Near Net Shape Products, TMS, Warrendale (1988), 423-437.

[46] A. Gagnoud and I. Leclercq, "Free Boundary Problem in Electromagnetic Levitation Melting and Continuous Casting", IEEE Transactions on Magnetics, 24(1) (1988), 256-268.

[47] J. H. Zong, B. Li, and J. Szekely, "The Electrodynamic and Hydrodynamic Phenomena in Magnetically-Levitated Molten Droplets--I. Steady State Behavior", Acta Astronautica, 26(6) (1992), 435-449.

[48] J. H. Zong, B. Li, and J. Szekely, "The Electrodynamic and Hydrodynamic Phenomena in Magnetically-Levitated Molten Droplets--II. Transient Behavior and Heat Transfer Considerations", Acta Astronautica, 29(4) (1993), 305-311.

[49] A. Prosperetti, "Normal-mode analysis for the oscillations of a viscous liquid drop in an immiscible liquid", Journal de Mecanique, 19 (1980), 149-182.

[50] J. A. Tsamopoulos and R. A. Brown, "Nonlinear oscillations of inviscid drops and bubbles", Journal of Fluid Mechanics, 127 (1983), 519-537.

[51] T. S. Lundgren and N. N. Mansour, "Oscillations of drops in zero gravity with weak viscous effects", Journal of Fluid Mechanics, 194 (1988), 479-510.

[52] O. A. Basaran, "Nonlinear oscillations of viscous liquid drops", Journal of Fluid Mechanics, 241 (1992), 169-198.

[53] E. Downing, "MPC Researchers Conduct Pioneering Experiments Aboard Space Shuttle Columbia", Industry Collegium Report, 11(3) (1994), Materials Processing Center, MIT, 4-5.

[54] Team TEMPUS, "Materials Sciences on IML-2: The results of the TEMPUS Team", to be published.

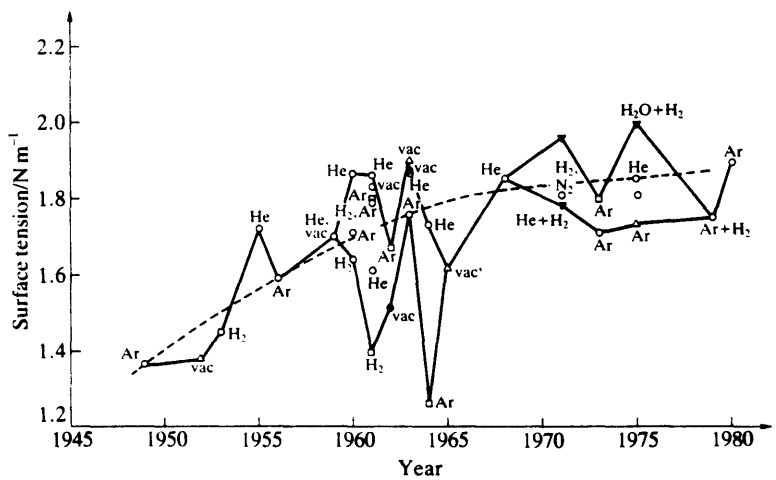

Figure 1.1 Surface tension values for liquid iron near its melting point as a function of year. From Iida and Guthrie [2], p. 113. Methods of surface tension measurement: ∘ Sessile drop, ◻ Maximum bubble pressure, Δ Pendant drop, ▼ Oscillating drop, • Drop weight. Data from Allen (1972b); Murarka, Lu, and Hamielec (1975); Kawai and Mori (1979); Ogino, Nogi, and Yamase (1980).

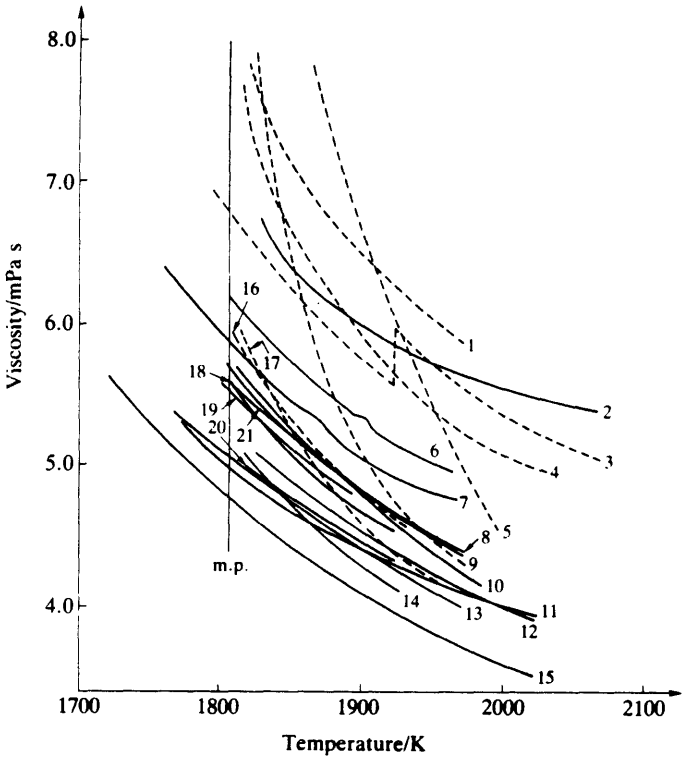

Figure 1.2 Viscosity of liquid iron, as determined by a number of workers. From Iida and Guthrie [2], p. 168. ------- Values obtained by workers in the USSR. (1) Arsentiev et al., (2) Barfield and Kitchener, (3) Nobohatskii et al., (4) Romanov and Kochegarov, (5) Samarin, (6) Ogino et al., (7) Ogino et al., (8) Nakanishi et al., (9) Vatolin et al., (10) Frohberg and Cakici, (11) Cavalier, (12) Saito and Watanabe, (13) Lucas, (14) Kawai et al., (15) Thiele, (16) Avaliani et al., (17) Wen Li-shi and Arsentiev, (18) Schenck et al., (19) Frohberg and Weber, (20) Narita and Onoe, (21) Krieger and Trenkler. (after Iida and Morita 1980).

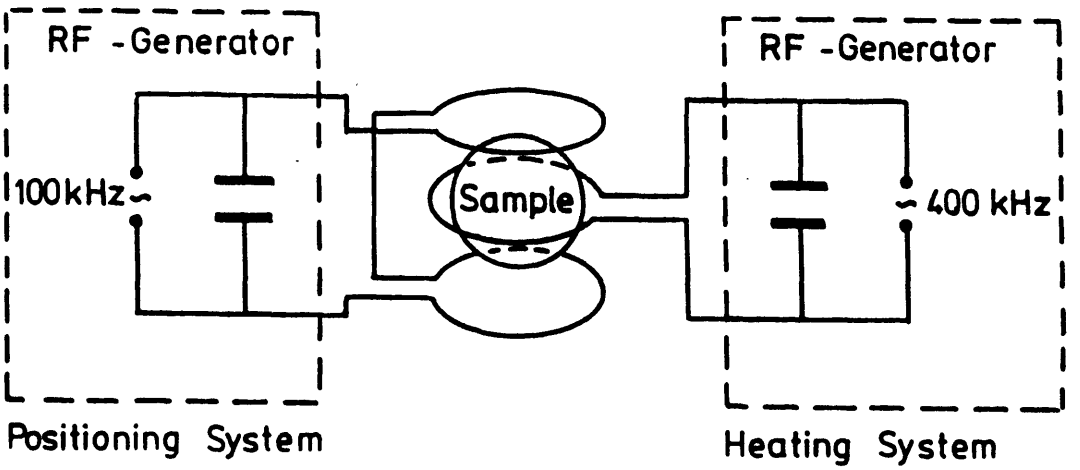

(a)

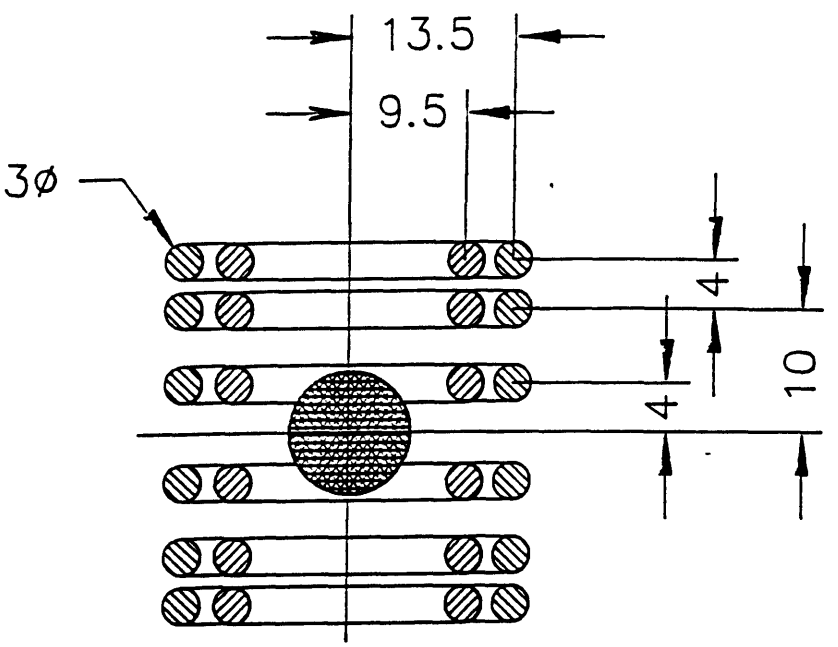

(b)

Figure 1.3 Schematic diagram of (a) separate positioning and heating coil systems and (b) coil geometry of TEMPUS electromagnetic containerless processing facility. Figures provided by I. Egry et al.

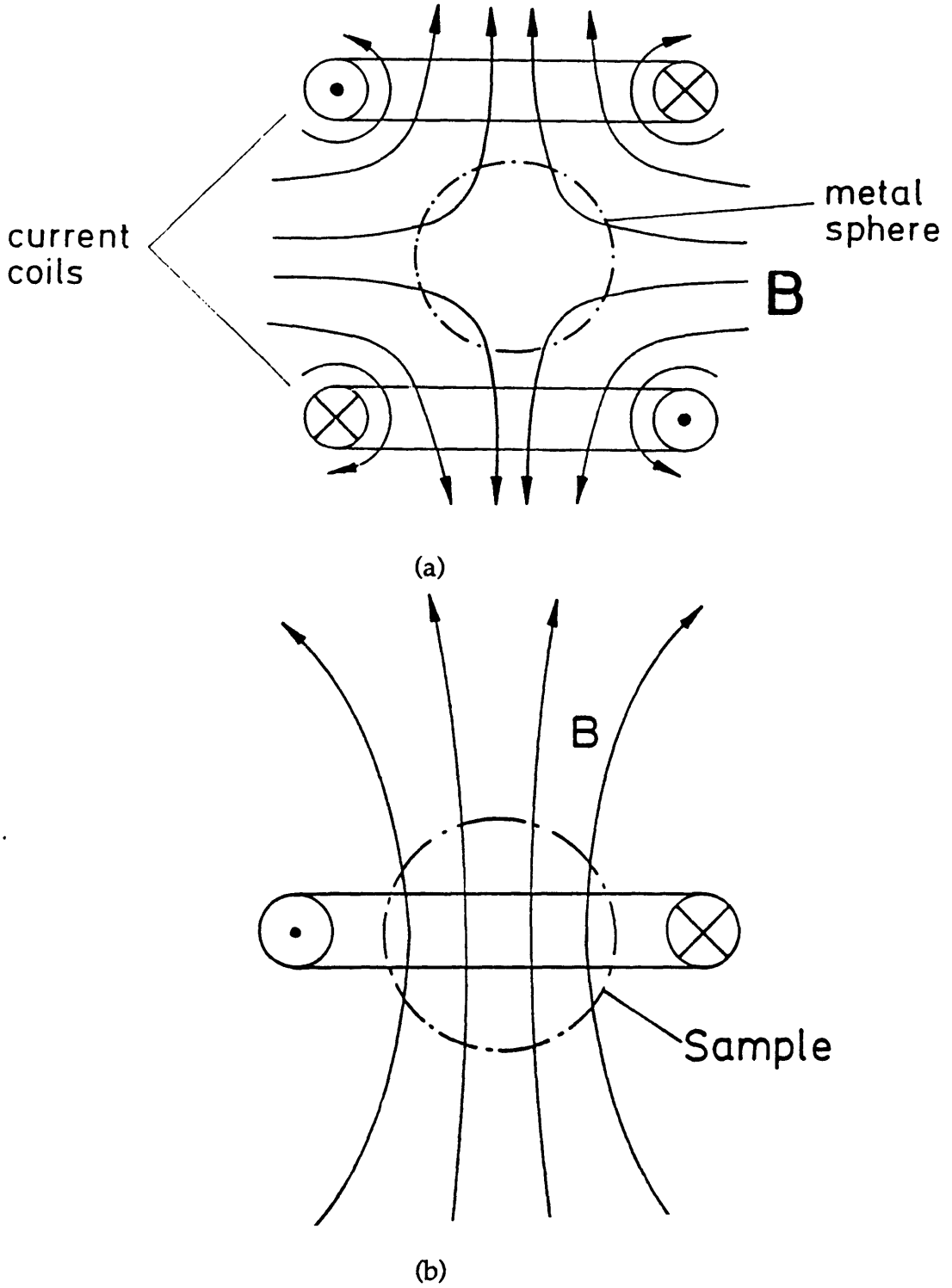

Figure 1.4 Sketch of (a) quadrupole magnetic field produced by TEMPUS positioning coils and (b) dipole magnetic field produced by TEMPUS heating coils. Figures provided by G. Lohoefer.

Table 1.1 Widely-used models for viscosity of liquid metals

Model	Equation for Viscosity	Adjustable Parameters
Arrhenius	$\mu = A\exp\left(\frac{E}{RT}\right)$	2
Hildebrand	$\mu = \frac{V_0}{B(V - V_0)}$	2
Andrade	$\mu = \frac{A}{V^{1/3}}\exp\left(\frac{C}{VT}\right)$	2
Vogel-Fulcher-Tammann	$\mu = A\exp\left(\frac{D}{T - T_0}\right)$	3

Table 1.2 Conventional surface tension measurement techniques

Method	Notes
Sessile Drop	Most extensively used for liquid metals and alloys, mathematical treatment and equipment relatively simple, difficult to completely eliminate contamination
Maximum Bubble Pressure	Frequently used for liquid metals and alloys, particularly suitable for metals which are very sensitive to surface contamination, correction factor needed in data analysis
Pendant Drop	Sometimes used for high-T_m refractory metals, not suitable for determining temperature variation of surface tension, similar to sessile drop method
Drop Weight	Sometimes used for high-T_m refractory metals, not suitable for determining temperature variation of surface tension, great care must be taken not to shake drops during experiment
Maximum Drop Pressure	Free of theoretical uncertainty, used for highly-reactive, low-T_m metals, limited to about 1000 K because of difficulties associated with design of equipment for high temperatures
Capillary Rise	Used for some low-T_m metals, not commonly used for liquid metals, simple theory but requires an exact knowledge of contact angles

Table 1.3 Conventional viscosity measurement techniques

Method	Notes
Oscillating-vessel	Most frequently used for elevated temperatures, simple apparatus and closed vessel, difficulty in solving equation of motion for system leads to large errors
Capillary	Reliable for low-T_m (below 1400 K) metals, usually for relative, rather than absolute, measurements, simple procedure
Rotational	Application to liquid metals difficult because of technical difficulty, simple mathematical analysis
Oscillating-plate	Has been used for liquid iron, unsuitable for measurements with low-viscosity liquid metal, construction and operation simple

Table 1.4 Principal Investigators (PIs) and experiments on TEMPUS IML-2

PI	Affiliation	Experiment
R. Bayuzick	Vanderbilt U.	Effects of Nucleation by Containerless Processing
I. Egry	DLR	Viscosity and Surface Tension of Undercooled Metallic Melts
H. Fecht	TU Berlin	Thermodynamics and Glass Formation of Undercooled Metallic Melts
M. Flemings	MIT	Alloy Undercooling Experiments
D. Herlach	DLR	Non-Equilibrium Solidification of Deeply Undercooled Melts
W. Johnson	Caltech	Thermophysical Properties of Metallic Glasses and Undercooled Alloys
J. Szekely	MIT	Measurement of the Viscosity and Surface Tension of Undercooled Melts and Supporting MHD Calculations
K. Urban	KFA Juelich	Structure and Solidification of Deeply Undercooled Melts of Quasicrystal-Forming Alloys

CHAPTER 2

ELECTROMAGNETIC CALCULATIONS

2.1 INTRODUCTION

In order to intelligently design the Space Shuttle experiments utilizing the TEMPUS electromagnetic levitation device, the development and testing of a code that could be used to calculate the lifting, positioning, stirring, and shaping forces and power absorbed by the sample was essential. Analytical closed-form expressions for the lifting force and power absorptions in levitated samples exist, but these solutions are confined to spherical samples and do not provide information about the local values of the forces or power absorbed, which are needed for any models of the internal fluid flow and heat transfer in the samples [1].

The electromagnetics code is used in subsequent chapters of this thesis, in other words, in every aspect of the mathematical modeling effort. The magnetic pressure distribution was recalculated as the free surface shape changed in each iteration of the model used to calculate the shape of levitated liquid metal droplets in Chapter 3. The spatial distribution of the Joule heating in levitated droplets was used in Chapter 4 to model the heat transfer in droplets during and after the application of heating coil pulses. The spatial distribution of electromagnetic (Lorentz) forces was used as the body force term in the numerical solution of the Navier-Stokes equations the calculate the electromagnetically-driven fluid flow pattern and free surface shape in Chapter 5.

The program used to calculate the electromagnetic phenomena has been developed by various members of the Materials Process Modeling Group over a number of years. The method of mutual inductances (also known as the coupled circuit or volume integral method), with a coordinate transformation method that allows for efficient treatment of axisymmetric bodies of arbitrary cross section, is used to calculate the distribution of induced currents in the sample. The coordinate transformation also makes it possible to accurately model cases with a broad range of skin depth-to-sample radius

ratio. The work which is specific to this thesis is the improvement of the formulae used to calculate the mutual inductances and self inductances and testing of the code.

2.2 ANALYTICAL CALCULATIONS

Calculation of the characteristic times of the system is a useful first step to understanding which physical processes are dominant [2]. The electroquasistatic charge relaxation time is given by [2]

$$\tau_e = \frac{\varepsilon_0}{\sigma_{el}} \tag{2.1}$$

where ε_0 is the electrical permittivity and σ_{el} is the electrical conductivity of the material. The magnetoquasistatic magnetic diffusion time is given by [2]

$$\tau_m = \mu_0 \sigma_{el} L^2 \tag{2.2}$$

where μ_0 is the magnetic permeability and L is the characteristic length, which in this case is the radius of the droplet. The electromagnetic wave transit time is the geometric mean of the charge relaxation and magnetic diffusion times [2]

$$\tau_{em} = \sqrt{\tau_e \tau_m} \tag{2.3}$$

The characteristic times τ_e, τ_m, and τ_{em} are approximately 10^{-18} s, 10^{-4} s, and 10^{-11} s, respectively. Comparison of the reciprocals of these times with the applied frequency for typical metals indicates that the magnetoquasistatic (MQS) laws apply for samples processed in TEMPUS. The applied frequencies, which are greater than 10^5 Hz, are greater than the reciprocal of the magnetic diffusion time and less than the electromagnetic wave transit time.

The MQS form of Maxwell's equations is given by [2]

$$\vec{\nabla} \times \vec{H} = \vec{J} \tag{2.4}$$

$$\vec{\nabla} \cdot \vec{B} = 0 \tag{2.5}$$

$$\vec{\nabla} \times \vec{E} = -\frac{\partial \vec{B}}{\partial t} \tag{2.6}$$

where $\vec{H}$ is the magnetic field intensity, $\vec{J}$ is the current density, $\vec{B}$ is the magnetic flux density, and $\vec{E}$ is the electric field intensity.

For a system excited sinusoidally at the angular frequency ω [3], the shielding parameter indicates the degree to which the conducting material resists diffusion of the magnetic field. The shielding parameter, which is equal to the ratio of the characteristic time for magnetic diffusion τ_m to the characteristic dynamical time for the applied field $\tau = 1/\omega$, is given by [3]

$$R_\omega = \frac{\tau_m}{\tau} = \mu_o \sigma_{el} \omega L^2 \tag{2.7}$$

For samples processed in TEMPUS, this parameter is of order 10^2, indicating that the conductors are largely able to resist diffusion of the applied field in TEMPUS.

The electromagnetic skin depth

$$\delta = \sqrt{\frac{2}{\mu_o \sigma_{el} \omega}} \tag{2.8}$$

quantifies the distance into a conducting material that an applied magnetic field of angular frequency ω diffuses. This distance is called a "skin" depth because the currents induced in the conducting material to create a magnetic field to oppose the external magnetic field are concentrated in a region near the surface of the material, a phenomenon known as the "skin effect". The ratio of electromagnetic skin depth to the characteristic length (droplet radius) indicates the portion of the droplet that is exposed to significant electromagnetic phenomena. For the samples processed in TEMPUS, the skin depth is on the order of 10% of the droplet radius, indicating, like the value of

the shielding parameter, that the applied field is shielded from much of the interior of the droplet.

The magnetic Reynolds number is analogous to the Reynolds number in fluid mechanics in that the magnetic Reynolds number indicates whether the magnetic field distribution is largely determined by convection or diffusion in the electrically-conducting fluid. The magnetic Reynolds number, equal to the ratio of the characteristic time for convection τ_{conv} to the characteristic time for magnetic field diffusion τ_m, is given by [3]

$$\mathrm{Re}_m = \frac{\tau_{conv}}{\tau_m} = \mu_o \sigma_{el} UL \tag{2.9}$$

where U is the characteristic velocity. At the end of the TEMPUS heating coil pulse, when the magnitude of the fluid velocity is greatest, the magnetic Reynolds number is still less than 0.01. This indicates that the internal fluid flow does not influence the magnetic field distribution, making it possible to neglect fluid flow in electromagnetic calculations.

2.3 METHOD OF MUTUAL INDUCTANCES

The distributions of induced current density $\vec{J}$ and magnetic flux density $\vec{B}$ for a given coil geometry, coil current, sample shape, and sample properties can be calculated in two different ways. Rather than starting with the differential Maxwell's equations, solving for the magnetic field, then computing the induced current, the method of mutual inductances is used. In this technique the axisymmetric droplet is discretized into a set of annular elemental circuits and one solves for the induced current flowing through each circuit [1,4-5]. It is assumed that the current flowing through each circuit is constant across the cross-section of the circuit.

As can be seen in Equation 2.5, the magnetic flux density $\vec{B}$ is divergenceless and can therefore be expressed in terms of a vector potential $\vec{A}$, as given by [2]

$$\vec{B} = \vec{\nabla} \times \vec{A} \tag{2.10}$$

The vector potential at the position $\vec{r}$ can be expressed by a superposition law. The applied current travels only in the ϕ-direction and there are no ferromagnetic materials, therefore [2]

$$A_\phi(\vec{r}) = \frac{\mu_0}{4\pi}\int_{V'} \frac{J'_\phi(\vec{r}')dv'(\vec{r}')}{|\vec{r}-\vec{r}'|} \tag{2.11}$$

where the primed quantities indicate the current source and the unprimed quantities indicate the point of observation, the position $\vec{r}$.

Omitting the coordinate ϕ, the vector potential in a given elemental circuit, indicated by position $\vec{r}$, comes from induced current flowing through the N elemental circuits (including the one being considered) and from the applied current in the M induction coils. For a given coil frequency, the vector potential in circuit i is then given by [1,4,6]

$$A_i(\vec{r}) = \frac{\mu_0}{4\pi}\left\{\sum_{j=1}^{N}\oint_{C_j}\int_{S_j}\frac{J_j dS_j dl_j}{r_{ij}} + \sum_{k=1}^{M}\oint_{C_k}\frac{I_k dl_k}{r_{ik}}\right\} \tag{2.12}$$

where J_j is the current density in circuit j, dS_j and dl_j are the differential area and line elements for circuit j, r_{ij} is the distance between circuits i and j, I_k is the applied current in coil k, dl_k is the differential line element for coil k, and r_{ik} is the distance between circuit i and coil k.

The current density in circuit i can be expressed in phasor and complex notation as

$$J_i = J_0 \exp j(\omega t - \alpha) = J_i^R + jJ_i^I \tag{2.13}$$

where J_0 is the amplitude, ω is the angular frequency of the applied current, α is the phase, R and I denote the real and imaginary parts of the current density, and j is the imaginary number $\sqrt{-1}$.

Using Ohm's Law, Faraday's Law (Equation 2.6), and the definition of vector potential, the current density can be expressed in terms of the vector potential as

$$J_\phi = \sigma_{el} E_\phi = -\sigma_{el} \frac{\partial A_\phi}{\partial t} \tag{2.14}$$

Expressing the vector potential in phasor notation and omitting the coordinate ϕ yields

$$-\sigma_{el} \frac{\partial A_i}{\partial t} = -j\sigma_{el}\omega A_i \tag{2.15}$$

Using Equations 2.13-2.15,

$$J_i^R + jJ_i^I = -j\sigma_{el}\omega A_i^R + \sigma_{el}\omega A_i^I \tag{2.16}$$

Equating the real and imaginary parts of Equation 2.16 yields the equations

$$A_i^R = -\frac{1}{\sigma_{el}\omega} J_i^I \tag{2.17}$$

$$A_i^I = \frac{1}{\sigma_{el}\omega} J_i^R \tag{2.18}$$

Equation 2.12 can be separated into two equations, which account for the real and imaginary parts of the vector potential

$$A_i^R = \frac{\mu_0}{4\pi}\left\{\sum_{j=1}^{N} \oint_{C_j} \int_{S_j} \frac{J_j^R dS_j dl_j}{r_{ij}} + \sum_{k=1}^{M} \oint_{C_k} \frac{I_k^R dl_k}{r_{ik}}\right\} \tag{2.19}$$

$$A_i^I = \frac{\mu_0}{4\pi}\left\{\sum_{j=1}^{N} \oint_{C_j} \int_{S_j} \frac{J_j^I dS_j dl_j}{r_{ij}} + \sum_{k=1}^{M} \oint_{C_k} \frac{I_k^I dl_k}{r_{ik}}\right\} \tag{2.20}$$

Substituting Equations 2.17 and 2.18 into Equations 2.19 and 2.20 gives

$$-\frac{1}{\sigma_{el}\omega}J_i^I = \frac{\mu_0}{4\pi}\left\{\sum_{j=1}^{N}\oint_{C_j}\int_{S_j}\frac{J_j^R dS_j dl_j}{r_{ij}} + \sum_{k=1}^{M}\oint_{C_k}\frac{I_k^R dl_k}{r_{ik}}\right\} \tag{2.21}$$

$$\frac{1}{\sigma_{el}\omega}J_i^R = \frac{\mu_0}{4\pi}\left\{\sum_{j=1}^{N}\oint_{C_j}\int_{S_j}\frac{J_j^I dS_j dl_j}{r_{ij}} + \sum_{k=1}^{M}\oint_{C_k}\frac{I_k^I dl_k}{r_{ik}}\right\} \tag{2.22}$$

Taking the line integrals of Equations 2.21 and 2.22 over the curve C_i, the length of circuit i, yields the equations

$$-\frac{1}{\sigma_{el}\omega}\oint_{C_i}J_i^I dl_i = \frac{\mu_0}{4\pi}\left\{\oint_{C_i}\sum_{j=1}^{N}\oint_{C_j}\int_{S_j}\frac{J_j^R dS_j dl_j}{r_{ij}}dl_i + \oint_{C_i}\sum_{k=1}^{M}\oint_{C_k}\frac{I_k^R dl_k}{r_{ik}}dl_i\right\} \tag{2.23}$$

$$\frac{1}{\sigma_{el}\omega}\oint_{C_i}J_i^R dl_i = \frac{\mu_0}{4\pi}\left\{\oint_{C_i}\sum_{j=1}^{N}\oint_{C_j}\int_{S_j}\frac{J_j^I dS_j dl_j}{r_{ij}}dl_i + \oint_{C_i}\sum_{k=1}^{M}\oint_{C_k}\frac{I_k^I dl_k}{r_{ik}}dl_i\right\} \tag{2.24}$$

Because the current density is taken to be constant across the cross section of a given circuit and the order the integration over C_i and summation can be interchanged,

$$-\frac{1}{\sigma_{el}\omega}\oint_{C_i}J_i^I dl_i = \sum_{j=1}^{N}\left(J_j^R A_j\right)\frac{\mu_0}{4\pi}\oint_{C_i}\oint_{C_j}\frac{dl_j dl_i}{r_{ij}} + \sum_{k=1}^{M}I_k^R\frac{\mu_0}{4\pi}\oint_{C_i}\oint_{C_k}\frac{dl_k dl_i}{r_{ik}} \tag{2.25}$$

$$\frac{1}{\sigma_{el}\omega}\oint_{C_i}J_i^R dl_i = \sum_{j=1}^{N}\left(J_j^I A_j\right)\frac{\mu_0}{4\pi}\oint_{C_i}\oint_{C_j}\frac{dl_j dl_i}{r_{ij}} + \sum_{k=1}^{M}I_k^I\frac{\mu_0}{4\pi}\oint_{C_i}\oint_{C_k}\frac{dl_k dl_i}{r_{ik}} \tag{2.26}$$

The terms on the right hand sides of Equations 2.25 and 2.26 include Neumann's formula for mutual inductances between circuits i and j and between circuits i and k [7]

$$M_{ij} = \frac{\mu_0}{4\pi}\oint_{C_i}\oint_{C_j}\frac{dl_j dl_i}{r_{ij}} \tag{2.27}$$

$$M_{ik} = \frac{\mu_0}{4\pi}\oint_{C_i}\oint_{C_k}\frac{dl_k dl_i}{r_{ik}} \tag{2.28}$$

Rearranging and expressing the current density in terms of current (J=I/A),

$$\frac{1}{\sigma_{el}}\oint_{C_i}\frac{I_i^I}{A_i}dl_i = -\omega\sum_{j=1}^{N}I_j^R M_{ij} - \omega\sum_{k=1}^{M}I_k^R M_{ik} \tag{2.29}$$

$$\frac{1}{\sigma_{el}}\oint_{C_i}\frac{I_i^R}{A_i}dl_i = \omega\sum_{j=1}^{N}I_j^I M_{ij} + \omega\sum_{k=1}^{M}I_k^I M_{ik} \tag{2.30}$$

The resistance of a circuit is expressed as [8]

$$R = \frac{L}{\sigma_{el}A} \tag{2.31}$$

The current flowing in a given elemental circuit is constant around the circulation loop, therefore,

$$I_i^I R_i = -\omega\sum_{j=1}^{N}I_j^R M_{ij} - \omega\sum_{k=1}^{M}I_k^R M_{ik} \tag{2.32}$$

$$I_i^R R_i = \omega\sum_{j=1}^{N}I_j^I M_{ij} + \omega\sum_{k=1}^{M}I_k^I M_{ik} \tag{2.33}$$

From basic electromagnetic theory [2], the magnetic flux Φ from the current source is the sum of the products of inductance and current through each induction coil, therefore,

$$R_i I_i^I + \omega\sum_{j=1}^{N}M_{ij}I_j^R = -\omega\Phi^R \tag{2.34}$$

$$R_i I_i^R - \omega\sum_{j=1}^{N}M_{ij}I_j^I = \omega\Phi^I \tag{2.35}$$

Changing the indices i and j in Equation 2.34 to indices m and n yields

$$R_m I_m^I + \omega\sum_{n=1}^{N}M_{mn}I_n^R = -\omega\Phi^R \tag{2.36}$$

Solving for I_m^I,

$$I_m^I = -\frac{\omega}{R_m}\sum_{n=1}^{N}M_{mn}I_n^R - \frac{\omega}{R_m}\Phi^R \tag{2.37}$$

Changing indices m and n to j and i and using the fact that $M_{ji}=M_{ij}$,

$$I_j^I = -\frac{\omega}{R_j}\sum_{i=1}^{N} M_{ij} I_i^R - \frac{\omega}{R_j}\Phi^R \tag{2.38}$$

Substitution of Equation 2.38 into Equation 2.35 yields

$$R_i I_i^R - \omega \sum_{j=1}^{N} M_{ij}\left[-\frac{\omega}{R_j}\sum_{i=1}^{N} M_{ij} I_i^R - \frac{\omega}{R_j}\Phi^R\right] = \omega\Phi^I \tag{2.39}$$

Rearranging terms,

$$\left[R_i + \omega^2 \sum_{j=1}^{N} \frac{M_{ij}}{R_j}\sum_{i=1}^{N} M_{ij}\right] I_i^R = \omega\Phi^I - \omega^2 \sum_{j=1}^{N} \frac{M_{ij}}{R_j}\Phi^R \tag{2.40}$$

The equation can be expressed as a matrix equation

$$[R+X]I = C \tag{2.41}$$

where R is the diagonal matrix of resistances of the elemental circuits, X is the full matrix containing the self and mutual inductances, I is the vector (Nx1 matrix) of unknown currents through the elemental circuits, and C is the vector of applied sources from the induction coils.

By calculating the terms in matrices R, X, and C, and multiplying the inverse of the sum of the matrices R and X by the vector C, the induced current in each elemental circuit for a given applied frequency can be determined. To find the total induced current for all applied frequencies the induced current in that circuit for each frequency is summed. Dividing the induced current by the cross-sectional area for each circuit yields the induced current density distribution $\vec{J}$.

2.4 IMPROVEMENTS TO METHOD

Maxwell's formula for the mutual inductance M_{12} between two coaxial current loops [9],

$$M_{12} = \mu_o \sqrt{r_1 r_2}\left[\left(\frac{2}{k} - k\right)K(k) - \frac{2}{k}E(k)\right] \tag{2.42}$$

$$k = 2\sqrt{\frac{r_1 r_2}{d^2 + (r_1 + r_2)^2}} \tag{2.43}$$

where r_1 and r_2 are the radii of the loops, d is the perpendicular distance between the planes containing the loops, and K(k) and E(k) are the complete elliptic integrals of the first and second kind to modulus k, assumes that the cross section of the current loops is circular. This was the formula used in the original version of the code.

As can be seen in Figure 2.1, the cross section of the annular circuit elements is better approximated by a rectangle than by a circle. To calculate the mutual inductance between circuits of rectangular cross section, Lyle's method was used [10]. By this method each rectangular element was replaced with two representative locations called filaments at which Maxwell's formula could be applied [5]. These locations are given by the expressions below.

For an element such as element A in Figure 2.2, in which the element is longer in the axial than in the radial direction,

$$r_{A1} = r_{A2} = a_A\left(1 + \frac{c_A^2}{24a_A^2}\right) \tag{2.44}$$

$$z_{A1} = z_A + \beta \tag{2.45}$$

$$z_{A2} = z_A - \beta \tag{2.46}$$

$$\beta^2 = \frac{b_A^2 - c_A^2}{12} \tag{2.47}$$

where distances r_{A1}, r_{A2}, a_A, b_A, c_A, and β are illustrated in Figure 2.2.

For an element such as element B in Figure 2.2, in which the element is longer in the radial than in the axial direction,

$$r_{B3} = a_B\left(1+\frac{b_B^2}{24a_B^2}\right)+\delta \tag{2.48}$$

$$r_{B4} = a_B\left(1+\frac{b_B^2}{24a_B^2}\right)-\delta \tag{2.49}$$

$$z_{B3} = z_{B4} = z_B \tag{2.50}$$

$$\delta^2 = \frac{c_B^2 - b_B^2}{12} \tag{2.51}$$

where r_{B3}, r_{B4}, a_B, b_B, c_B, and δ are illustrated in Figure 2.2.

As an example, the mutual inductance between elements A and B is given by

$$M_{AB} = \frac{M_{13}+M_{14}+M_{23}+M_{24}}{4} \tag{2.52}$$

where M_{13} is the mutual inductance between filament 1 in element A and filament 3 in filament B. M_{14}, M_{23}, and M_{24} are similarly defined, and all are found using Maxwell's formula for the mutual inductance between two coaxial circles, given in Equation 2.42.

Lyle's method was further adapted to account for the fact that the sides of the approximately rectangular elements were not always oriented parallel and perpendicular to the axis of symmetry (z-axis). In the case of an element like A, Equations 2.44-2.47 become

$$r_{A1} = a_A\left(1+\frac{c_A^2}{24a_A^2}\right)+\beta\sin\theta \tag{2.53}$$

$$r_{A2} = a_A\left(1+\frac{c_A^2}{24a_A^2}\right)-\beta\sin\theta \tag{2.54}$$

$$z_{A1} = z_A+\beta\cos\theta \tag{2.55}$$

$$z_{A2} = z_A-\beta\cos\theta \tag{2.56}$$

where θ is the angle of declination ($0 \le \theta \le \pi$) from the positive z-axis in spherical coordinates for the given element. In the case of an element like B, Equations 2.48-2.51 become

$$r_{B3} = a_B\left(1+\frac{b_B^2}{24a_B^2}\right)+\delta\cos\theta \tag{2.57}$$

$$r_{B4} = a_B\left(1+\frac{b_B^2}{24a_B^2}\right)-\delta\cos\theta \tag{2.58}$$

$$z_{B3} = z_B - \delta\sin\theta \tag{2.59}$$

$$z_{B4} = z_B + \delta\sin\theta \tag{2.60}$$

In the original version of the code, the self inductance of an elemental circuit was calculated using the formula for a circular wire loop. For a non-ferromagnetic wire of cross-sectional radius R with ring radius a [9],

$$L = \mu_0 a\left(\ln\frac{8a}{R}-1.75\right) \tag{2.61}$$

As were the mutual inductances, the formula for the self inductances in the modified code was changed to account for the approximately rectangular cross section of the annular circuit elements. The self inductance of a rectangular conductor is given by [11]

$$L = \mu_0 a\left[\ln\frac{8a}{R}\left(1+\frac{3R^2}{16a^2}\right)-\left(2+\frac{R^2}{16a^2}\right)\right] \tag{2.62}$$

where a is now the mean radius of the rectangular conductor and R is the geometrical mean distance of the cross section of the conductor. For cross section dimensions b and c, R is defined by [11]

$$\ln R = \ln\sqrt{c^2+b^2}-\frac{1}{6}\frac{c^2}{b^2}\ln\sqrt{1+\frac{b^2}{c^2}}-\frac{1}{6}\frac{b^2}{c^2}\ln\sqrt{1+\frac{c^2}{b^2}}+\frac{2}{3}\frac{c}{b}\tan^{-1}\frac{b}{c}+\frac{2}{3}\frac{b}{c}\tan^{-1}\frac{c}{b}+\frac{25}{12} \tag{2.63}$$

Note that Equation 2.63 is symmetric in b and c. Substituting Equation 2.62 and 2.63 for Equation 2.61 in the calculation of the self inductance is an important improvement because the self inductances largely determine the

matrix of inductances in the matrix equation, Equation 2.41, used to solve for the unknown induced currents.

2.5 CALCULATION OF ELECTROMAGNETIC QUANTITIES

Equations 2.17 and 2.18 have been used to calculate the real and imaginary parts of the vector potential $\vec{A}$ from the induced current density $\vec{J}$, and Equation 2.10 has been used to calculate the distribution of magnetic flux density $\vec{B}$ from the vector potential. For multiple frequencies, the total induced current density and magnetic flux density are summed from the components calculated for each frequency. Because the induced current density and magnetic flux density are sinusoidal functions of time, the phase and amplitude of each field at a given location can be represented by a complex amplitude. The induced current and magnetic flux densities can be written as [2]

$$\vec{J} = \mathrm{Re}\,\hat{\vec{J}}e^{j\omega t} \tag{2.64}$$

$$\vec{B} = \mathrm{Re}\,\hat{\vec{B}}e^{j\omega t} \tag{2.65}$$

where Re indicates the real part of a complex quantity.

The applied current in the induction coils travels in the azimuthal, or ϕ-direction, therefore, the complex vector $\hat{\vec{J}}$ only has the one complex scalar component $\hat{J}_\phi$. Considering Ampere's Law, Equation 2.4, the applied current in the ϕ-direction induces a magnetic flux density vector field with components in the r- and θ-directions. The complex vector $\hat{\vec{B}}$ then has complex scalar components $\hat{B}_r$ and $\hat{B}_\theta$. Using the time average theorem [2], the time-averaged Lorentz force and power absorption per unit volume are given by

$$\vec{F}(r,\theta) = \frac{1}{\tau}\int_0^\tau \vec{J}\times\vec{B}dt = \frac{1}{2}\mathrm{Re}\,\hat{\vec{J}}\times\hat{\vec{B}}^* \tag{2.66}$$

$$Q(r,\theta) = \frac{1}{\tau}\int_0^\tau \frac{\vec{J}\cdot\vec{J}}{\sigma_{el}}dt = \frac{1}{2}\mathrm{Re}\frac{\hat{\vec{J}}\cdot\hat{\vec{J}}^*}{\sigma_{el}} \tag{2.67}$$

where τ is the period of the applied alternating current and an asterisk designates the complex conjugate. Integration of the Lorentz force and power absorption per unit volume over the volume of the sample yield the total time-averaged lifting force and power absorbed.

2.6 RESULTS

In order to confirm the accuracy of the results obtained from the electromagnetics code, the classical problem of a "flux ball" consisting of a sphere with windings on its surface that have uniform turns density with respect to the z-axis was used. This lossless sphere problem was selected because the magnetic field intensity produced inside a properly wound spherical coil has the important property of being uniform [2]. This would provide a clear indication of whether the results produced by the code were accurate. To approximate the DC field problem presented by Haus and Melcher [2], the electrical conductivity of the sample and the coil frequency in the set of input parameters for the code were selected so that the electromagnetic skin depth would be much larger than the radius of the sphere. In this limit the applied field nearly completely penetrates the sphere.

The graphical results of the calculations are shown in Figure 2.3. As can be seen, the magnetic flux density $\vec{B}$ at all points within the sphere is directed upward, and the magnitude is uniform throughout. The magnitude of the vectors is within 1% of the theoretical value for the given case. Note that because axisymmetric samples and rotationally symmetric coils are considered, the computational domain consists of a semicircle.

Lohoefer [12] presented an analytical solution for the total power absorption of a spherical sample in a rotationally symmetric coil system. The time-averaged total power absorbed is given by

$$Q = \frac{\pi}{2R_s\sigma_s}\sum_{n}\sum_{l=1}^{\infty} H_l(q_n)\left(I_{n,l}^2 + 2\sum_{n'>n}\delta_{\omega_n,\omega_{n'}}\cos(\alpha_n - \alpha_{n'})I_{n,l}I_{n',l}\right) \tag{2.68}$$

where

$$H_l(q_n) = \sum_{k=1}^{\infty} \frac{8q_n^4}{4q_n^4 + x_{l+1/2,k}^4} \tag{2.69}$$

$$q_n = \frac{R_s}{\delta_n} \tag{2.70}$$

$$I_{n,l} = \sqrt{\frac{2l+1}{l(l+1)}} I_n \left(\frac{R_s}{R_n}\right)^l \sin\theta_n P_l^1(\cos\theta_n) \tag{2.71}$$

where R_s and R_n are the radii of the sample and coil, σ_s is the electrical conductivity of the sample, n and n' are indices for different coils, δ with two indices is the Kronecker delta, ω is the angular frequency, δ_n is the skin depth, given by Equation 2.8, for coil n, α_n is the phase of the current through coil n, x indicates the zeroes of the spherical Bessel function, k and l are summation indices, I_n is the applied current in coil n, θ_n is the angle of declination from the z-axis for the position of coil n, and P is the associated Legendre polynomial.

This analytical solution was used to compare the accuracy of calculations of the induced current density distribution $\vec{J}$ made using Maxwell's formula for current loops of circular cross section and that of calculations made using the improved technique involving Lyle's method for rectangular conductors. The total Joule heating in a nickel sphere levitated in a conical coil arrangement was calculated using the two different versions of the code and compared with the value obtained using Lohoefer's analytical formula. With each version of the code, various numbers of mesh elements were used in order to investigate grid sensitivity. The calculations were performed with a DEC VAX 3100.

The calculated power absorbed (Joule heating), percentage error from the value obtained using Lohoefer's formula, and CPU time required for the calculation are presented in Table 2.1. As can be seen, the percentage error obtained using the old version of the code is not alarmingly high, but is clearly not negligible. The accuracy obtained using the version of the code with the improvements described above is markedly better, even when the grid is relatively coarse, as illustrated by the 0.3% error obtained with the 10x10 grid. Moreover, the calculation of the induced current distribution,

Joule heating, magnetic field distribution, and electromagnetic force distribution using the improved code and the 10x10 grid required less than one minute, while a calculation using the old code yielding comparable accuracy (0.5%) required a 40x40 grid and more than twelve hours of CPU time.

The old version of the code requires such a fine grid in order to substantially reduce the percentage error because only when the mesh is very fine does the cross sectional shape of the circuit element approximate the circular shape that use of Maxwell's formulas for the mutual inductance and self inductance assumes. The improved version of the code using Lyle's method considers the circuit elements to be approximately rectangular in shape, therefore, excellent accuracy is obtained with both coarse and fine meshes.

Once the accuracy of the computational methodology had been confirmed, we calculated the distributions of magnetic flux density and electromagnetic forces in samples levitated in conical and cylindrical coil arrangements. The conical coil geometry used to levitate a copper sample at the German Aerospace Research Establishment (DLR) is illustrated in Figure 2.4. It can be seen that the six lower coil windings, which supply the current that levitates the sample, are 180° out of phase with the two upper windings, which simply provide a cap to prevent the sample from escaping from the coil arrangement.

The magnetic flux density distribution calculated for the actual shape obtained in the experiments is shown in Figure 2.5. The magnitude of the magnetic flux density vectors is greatest at the surface and decays exponentially with normal distance into the sample, as would be expected from the fact that the skin depth is 13.08% of the radius of the unperturbed droplet. The magnitude of the magnetic flux density within the droplet is much higher in the bottom half of the droplet, with a maximum value of about 0.05 T for the applied current of 310 A, because of the six lower coil windings below the center of mass of the sample, which is at about z=0, and the fact that these windings are closer to the sample than are the upper windings. The vectors are oriented almost entirely tangential to the free surface because the high electrical conductivity of the copper sample almost

entirely eliminates the normal component of the applied field. The vectors are directed downward because the applied current in the lower windings is directed out of the plane of the paper along the right side of the droplet.

The distribution of electromagnetic forces $\vec{F}$ calculated in the same sample is shown in Figure 2.6. As with the magnetic flux density, the magnitude is greatest at the surface and in the lower half of the droplet, with a maximum value of about 2×10^6 N/m^3. The vectors are in the inward direction normal to the free surface of the droplet. As given in Equation 2.64, the electromagnetic force is mathematically expressed as the cross product of the induced current density and the magnetic flux density. The induced current in the right hemisphere of the droplet travels in the direction opposite to that of the applied current, into the plane of the paper (positive ϕ-direction). This interacts with the magnetic flux density traveling in the positive θ-direction to produce the force in the negative r-direction, the inward normal direction. The location along the free surface where the magnitude of the force is greatest corresponds to the stagnation point between recirculation loops in the fluid flow pattern. The location of the longest vector in Figure 2.6 can be seen to correspond to the location of the flow separation in the calculated velocity profile shown in Figure 5.3.

The coil geometry of the TEMPUS electromagnetic levitation device, which can only levitate samples in microgravity, is shown in Figure 2.7. The eight outer coil windings, which are called the positioning coils, create a quadrupole magnetic field to hold the sample in a stable position. This is accomplished by using applied current in the upper positioning coil windings that is 180° out of phase with the current in the lower positioning coil windings. The four inner coil windings, which are called the heating coils, create a dipole magnetic field.

The results of calculations of the magnetic flux density distribution produced by the TEMPUS positioning coils in a spherical sample of copper are shown in Figure 2.8. The magnitude is again seen to be greatest at the surface, with a maximum value of about 0.02 T for a positioning coil current of 185 A (control voltage of 6 V), and decrease exponentially with normal distance into the sample. The magnitude can be seen to be zero at the equator of the

sample, where the magnetic fields produced by the upper and lower positioning coil windings cancel each other. The magnetic flux density is again tangential to the surface of the sample due to the high electrical conductivity of copper. The vectors in the upper half of the sample travel in the negative θ–direction, while the vectors in the lower half can be seen to point in the positive θ-direction. These results are correct for applied current traveling in the positive ϕ–direction in the upper positioning coils and in the negative ϕ-direction in the lower positioning coils.

The results of calculations of the magnetic flux density distribution produced by the TEMPUS heating coils in the same spherical sample of copper are shown in Figure 2.9. The magnitude is greatest at the surface, with a maximum value of about 0.045 T for a heating coil current of 179 A (control voltage of 5 V), and decrease exponentially with normal distance into the sample. The magnitude can be seen to be highest at the equator of the sample, which is the part of the sample which is closest to the heating coils. The magnetic flux density is again tangential to the surface of the sample due to the high electrical conductivity of copper. The vectors throughout the sample point in the negative θ-direction due to the current applied in the positive ϕ–direction.

The calculation of the distribution of electromagnetic forces produced by the TEMPUS heating and positioning coils, with approximately the same applied current in each, is shown graphically in Figure 2.10. Because the magnetic fields produced by the upper and lower positioning coils cancel each other, the magnetic field produced by the heating coils is dominant. The magnitude of the forces is greatest at the surface and at the equator, with a maximum value of about 2.5×10^6 N/m^3, due to maximum magnetic field strength at the location closest to the heating coils. Once again the applied current in the positive ϕ-direction interacts with the magnetic flux density traveling in the positive θ-direction to produce the force in the negative r-direction, the inward normal direction. In this case the maximum force at the equator would cause the fluid flow pattern of samples levitated in TEMPUS in microgravity to be characterized by two symmetrical recirculation loops.

2.7 ACKNOWLEDGEMENTS

The author would like to gratefully acknowledge the assistance of Mr. Robert Hyers in producing the plots presented in this chapter and the interpretation of the results.

2.8 REFERENCES

[1] J.-H. Zong, J. Szekely, and E. Schwartz, "An Improved Computational Technique for Calculating Electromagnetic Forces and Power Absorptions Generated in Spherical and Deformed Body in Levitation Melting Devices", IEEE Transactions on Magnetics, 28(3) (1992), 1833-1842.

[2] H. A. Haus and J. R. Melcher, Electromagnetic Fields and Energy, Prentice Hall, Englewood Cliffs, NJ, 1989.

[3] J. R. Melcher, Continuum Electromechanics, MIT Press, Cambridge, MA, 1981.

[4] N. El-Kaddah and J. Szekely, "The Electromagnetic Force Field, Fluid Flow Field, and Temperature Profiles in Levitated Metal Droplets", Metallurgical Transactions, 14B (1983), 401-410.

[5] E. Schwartz, S. Sauerland, J. Szekely, and I. Egry, "On the Shape of Liquid Metal Droplets in Electromagnetic Levitation Experiments", Containerless Processing: Techniques and Applications, TMS, Denver, 1993, 57-64.

[6] J.-H. Zong, B. Li, and J. Szekely, "The Electrodynamic and Hydrodynamic Phenomena in Magnetically-Levitated Molten Droplets--I. Steady State Behavior", Acta Astronautica, 26(6) (1992), 435-449.

[7] W. K. H. Panofsky and M. Phillips, Classical Electricity and Magnetism, Addison-Wesley Publishing Company, Inc., Reading, MA, 1962.

[8] D. Halliday and R. Resnick, Fundamentals of Physics, John Wiley & Sons, Inc., New York, 1974.

[9] E. Hallen, Electromagnetic Theory, John Wiley & Sons, Inc., New York, 1962.

[10] R. Dudley and P. E. Burke, "The Prediction of Current Distribution in Induction Heating Installations", IEEE Transactions on Industry Applications, IA-8(5) (1972), 565-571.

[11] P. E. Burke, P. P. Biringer, P. F. Ryff, and E. Solger, "The Prediction and Measurement of Current Distribution in Coaxial Circular Geometries", 6th PICA Conference Proceedings, (1969), 464-482.

[12] G. Lohoefer, "Theory of an Electromagnetically Levitated Metal Sphere I: Absorbed Power", SIAM Journal of Applied Mathematics, 49(2) (1989), 567-581.

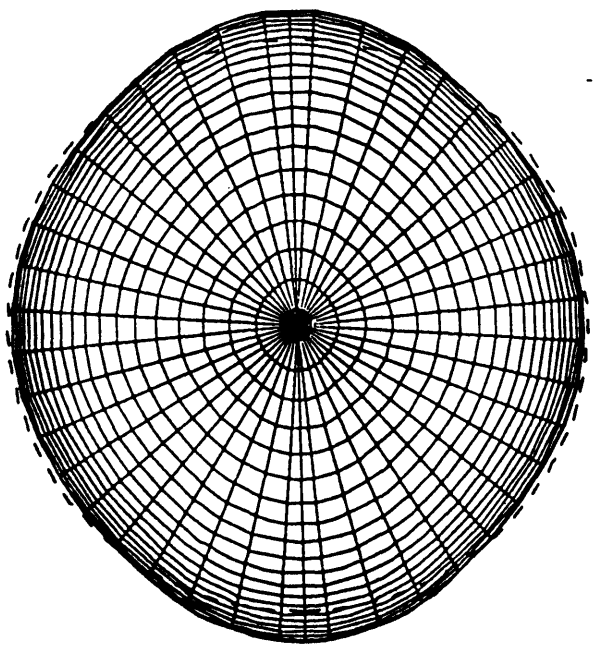

Figure 2.1 Discretization of droplet domain, showing exponential grid point distribution and rectangular cross section of annular circuit elements.

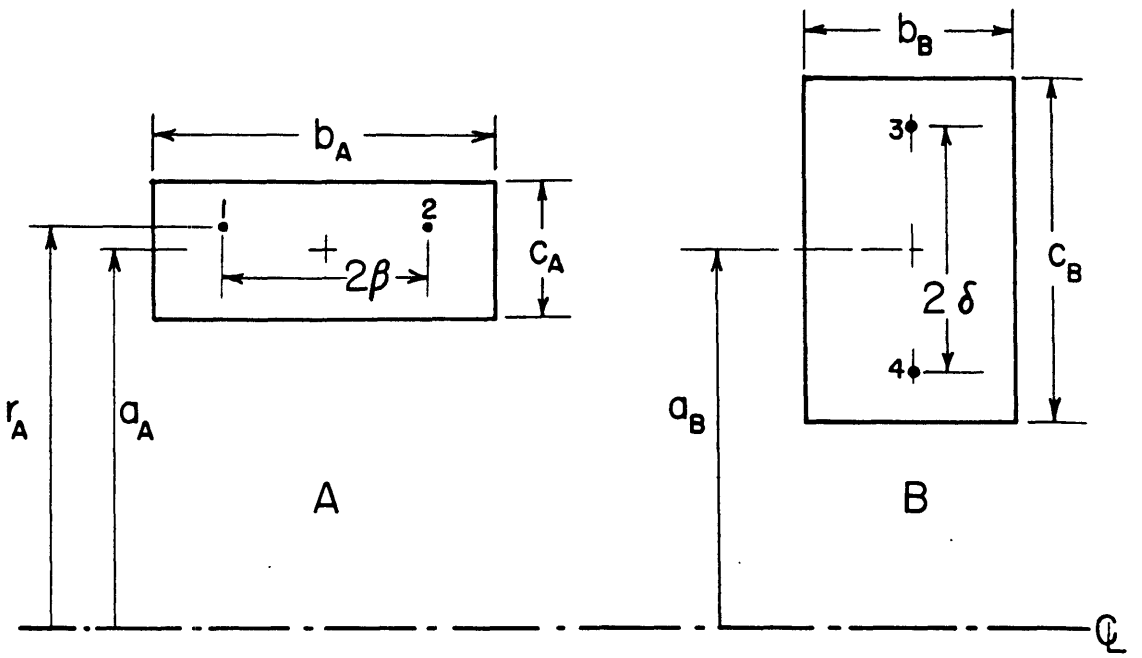

Figure 2.2 Illustration of geometrical parameters used in Lyle's method for calculating mutual inductances between rectangular coils. From [11].

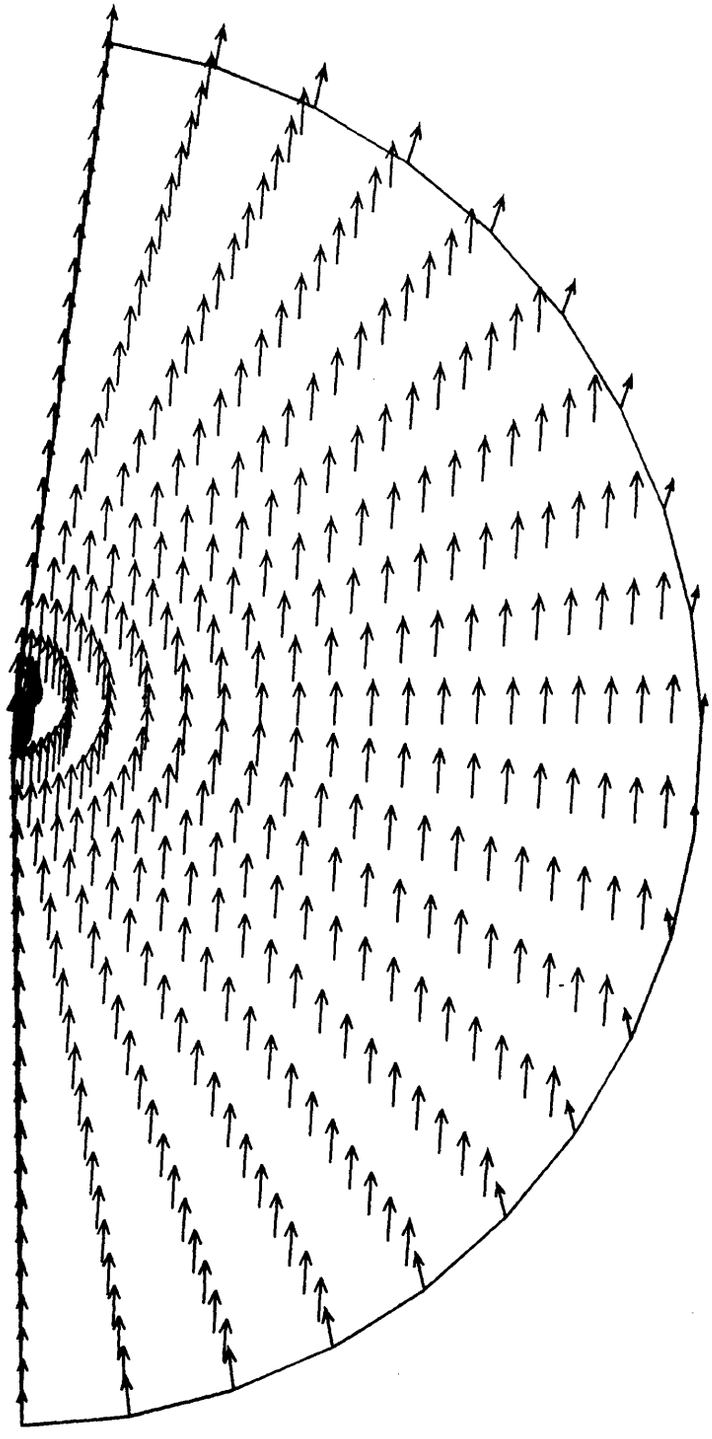

Figure 2.3 Magnetic flux density distribution calculated for test case of the "flux ball", a sphere with windings on its surface that have uniform turns density with respect to the z-axis.

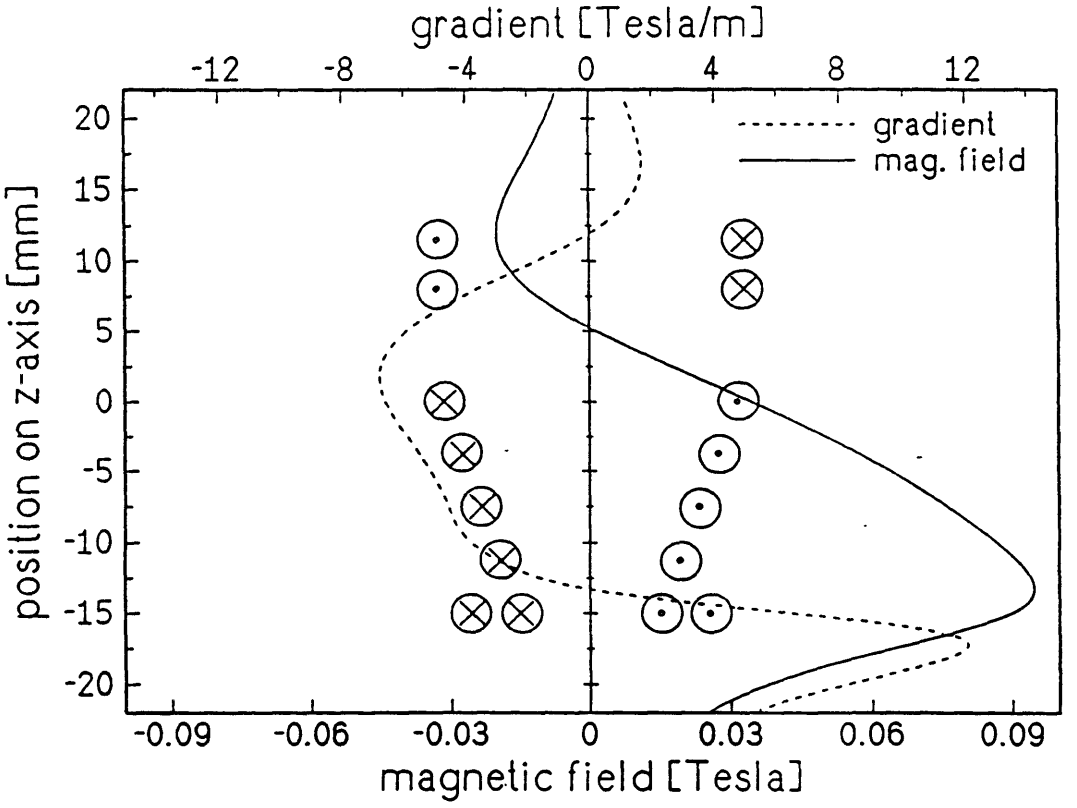

Figure 2.4 Conical coil arrangement used to levitate copper sample at German Aerospace Research Establishment (DLR).

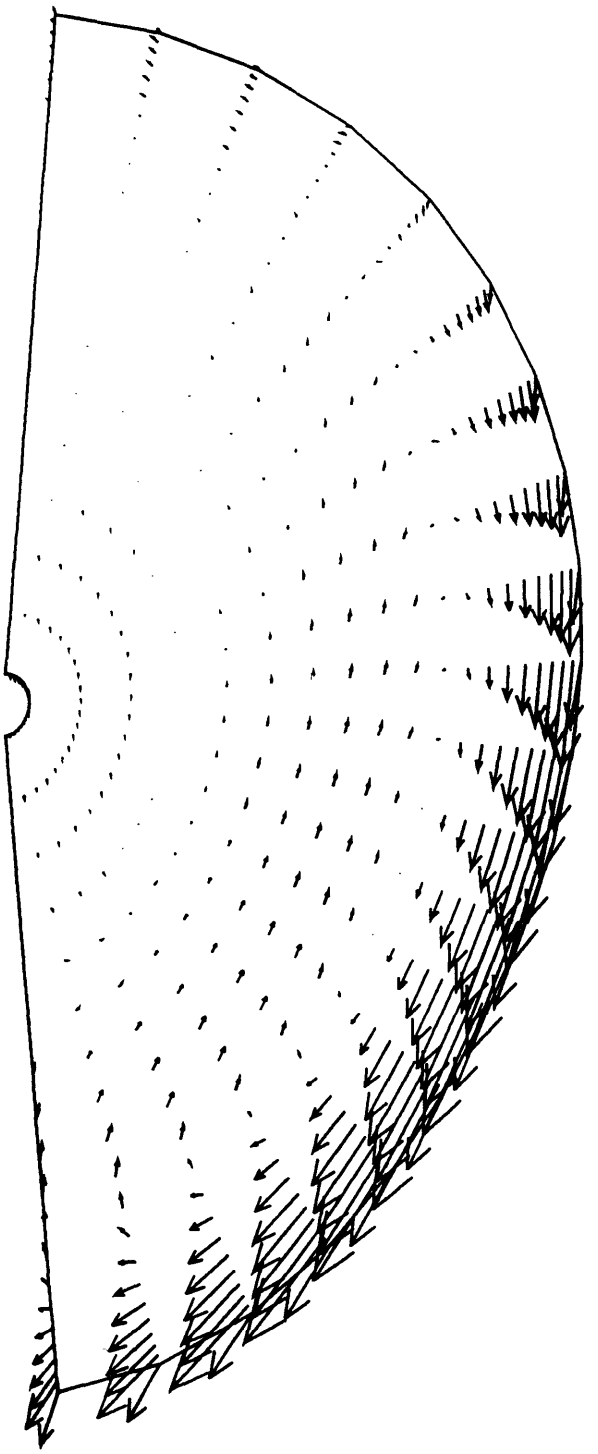

Figure 2.5 Magnetic flux density distribution calculated for actual shape of copper droplet levitated in DLR conical coil arrangement.

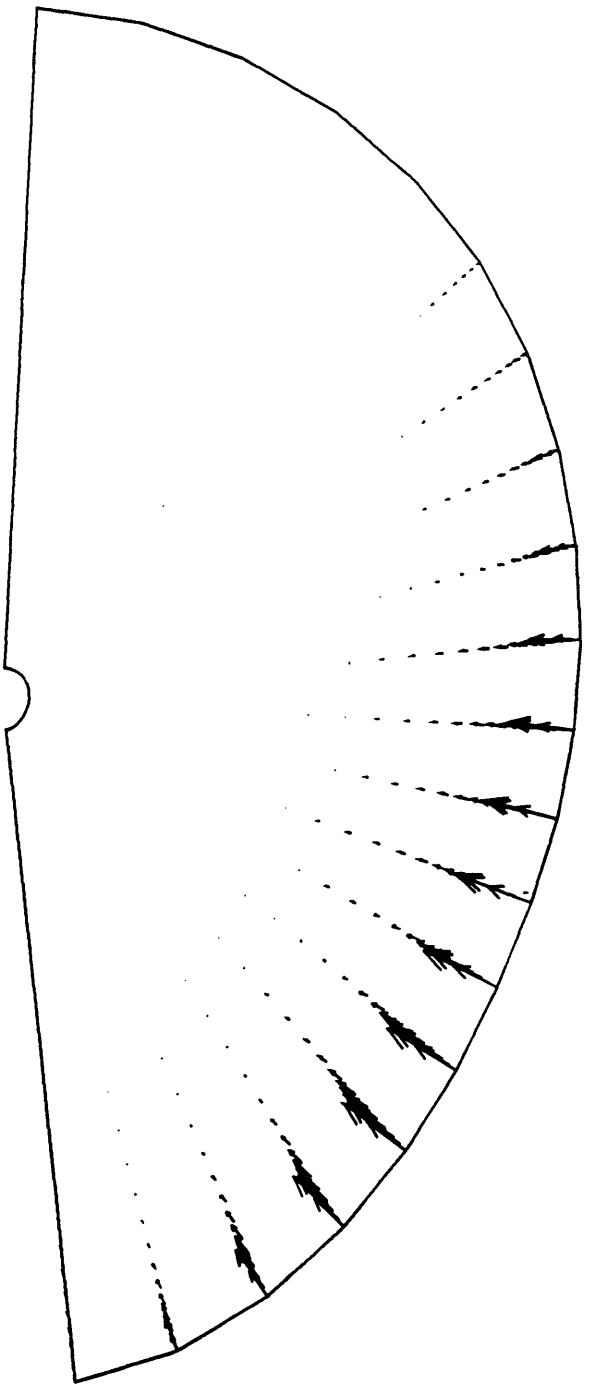

Figure 2.6 Electromagnetic force distribution calculated for actual shape of copper droplet levitated in DLR conical coil arrangement.

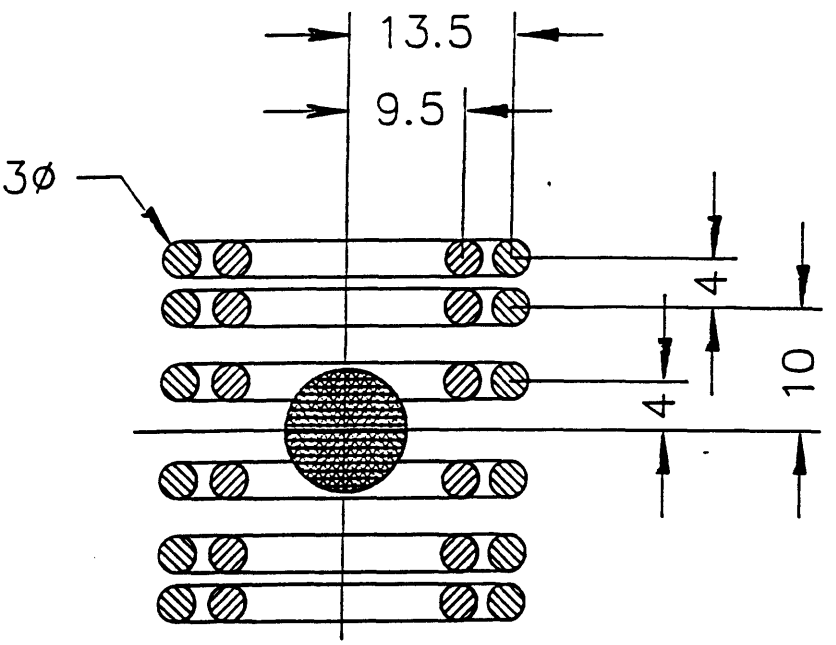

Figure 2.7 Schematic diagram of coil geometry of TEMPUS electromagnetic containerless processing facility (dimensions in mm). Inner four coils are heating coils and outer eight coils are positioning coils. Figure provided by I. Egry et al.

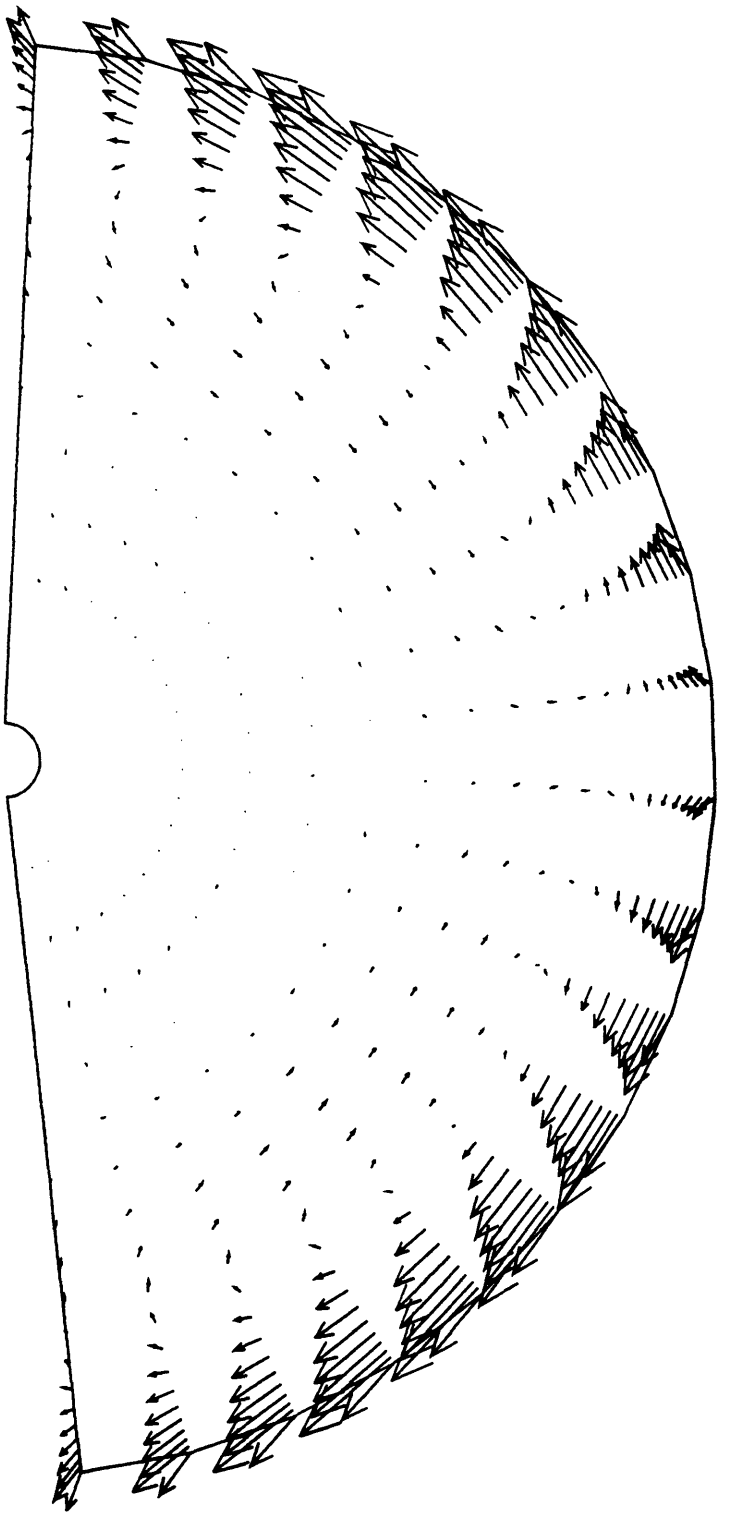

Figure 2.8 Magnetic flux density distribution calculated for spherical sample of copper in TEMPUS positioning coil field.

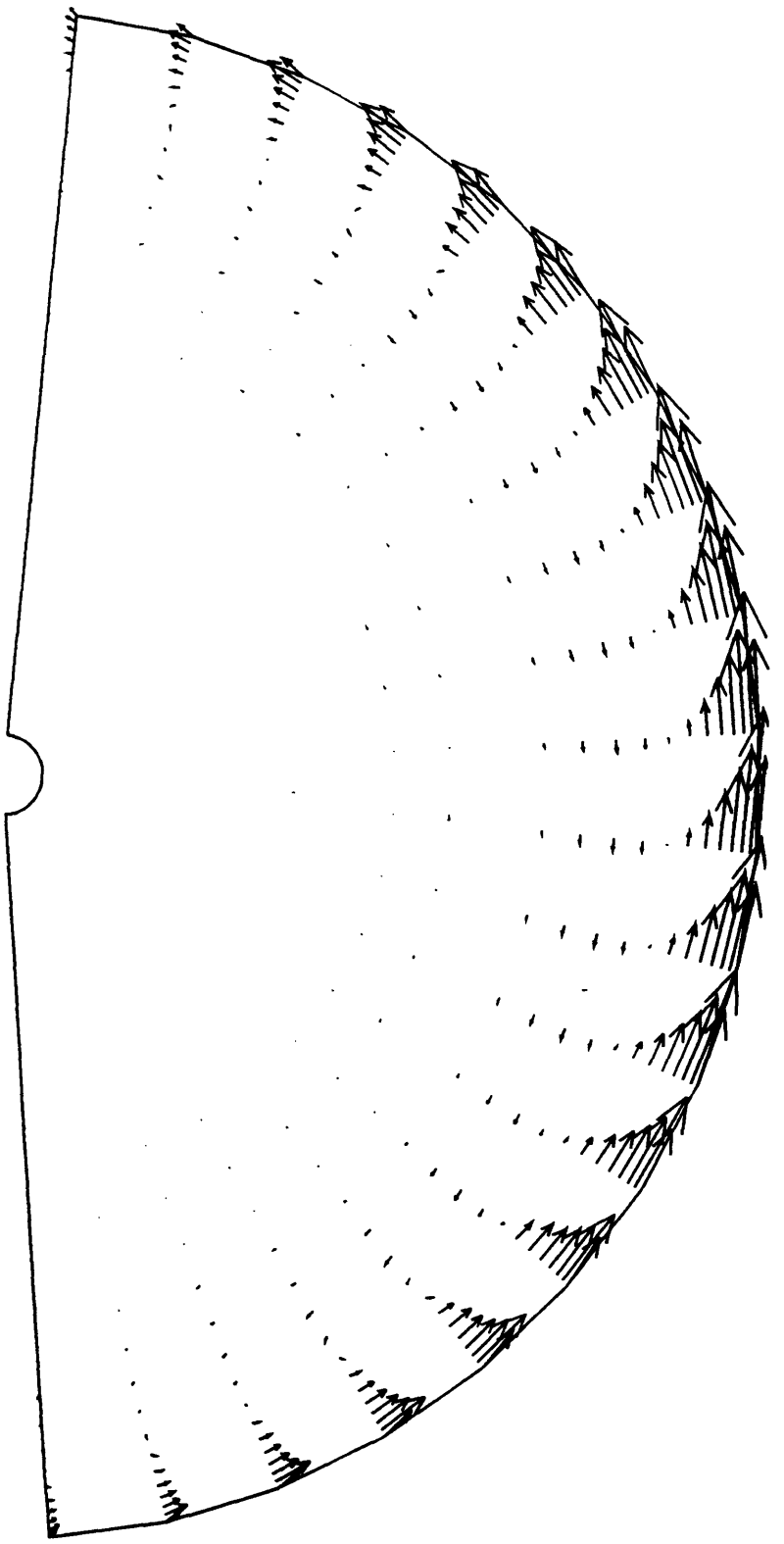

Figure 2.9 Magnetic flux density distribution calculated for spherical sample of copper in TEMPUS heating coil field.

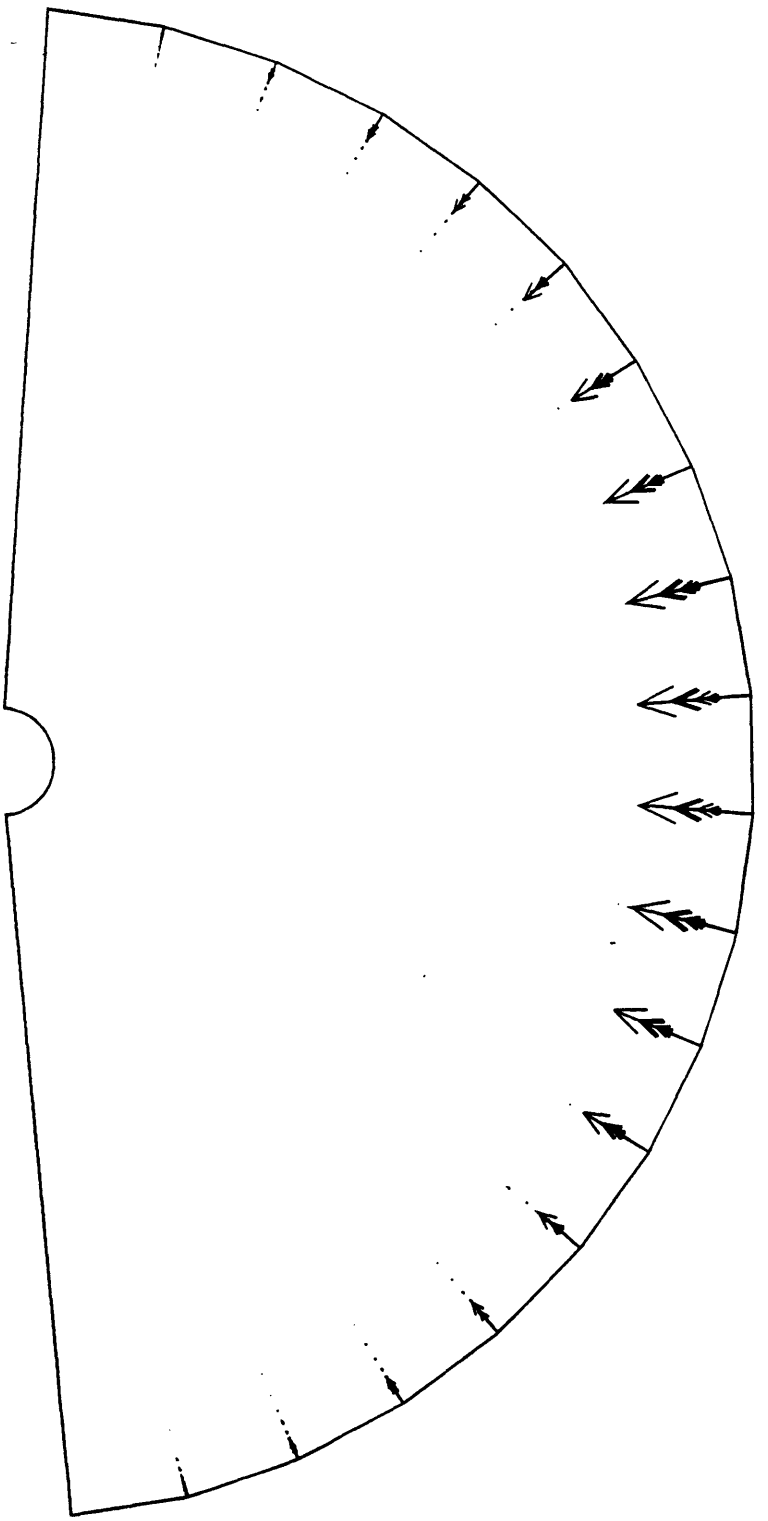

Figure 2.10 Electromagnetic force distribution calculated for spherical sample of copper in TEMPUS positioning and heating coil fields.

Table 2.1 Comparison of versions of code used to calculate Joule heating in Ni sphere

Method	Grid	Power (W)	Error (%)	CPU time
Analytical	N/A	74.5651	N/A	N/A
Old	10x10	69.9387	6.2	0:18.88
Old	15x15	72.2163	3.1	2:02.27
Old	20x20	73.1557	1.9	9:50.60
Old	40x40	74.1787	0.5	12:08:52.13
New	10x10	74.3502	0.3	0:36.60
New	20x20	74.4876	0.1	14:56.12

CHAPTER 3

ON THE SHAPE OF LIQUID METAL DROPLETS IN ELECTROMAGNETIC LEVITATION EXPERIMENTS

ABSTRACT

We present calculations and measurements on the shape of liquid metal droplets in electromagnetic levitation experiments. A normal stress balance model was developed to predict the shapes of liquid metal droplets that will be obtained in a microgravity experiment to measure the viscosity and surface tension of undercooled metals. This model was tested by calculating the droplet shapes in containerless experiments conducted to determine the surface tension of liquid metals. The computational results of the mathematical model are compared with the results of ground-based experiments for two different metals. The importance of the ratio of electromagnetic skin depth-to-droplet radius to the accuracy of the mathematical model is discussed. As an example of an application, the influence of the shape on the splitting of the surface oscillation modes of levitated liquid metal droplets is discussed.

3.1 INTRODUCTION

In recent years electromagnetic levitation has become both a widely-used experimental technique and an important part of the field of materials processing. Levitation of liquid metal droplets provides a clean, containerless environment that makes it possible to perform high-precision experiments and process reactive metals with high melting points.

Electromagnetic levitation provides the opportunity to perform experiments on undercooled liquid metals in such areas as the study of nucleation and recalescence and measurement of thermophysical properties such as heat capacity, surface tension, and viscosity. The behavior of undercooled melts has both fundamental and practical interest. Undercooled melts are now being processed in technologies such as near net shape casting and rapid solidification. This requires increased knowledge about the melt-solid phase transition and the temperature dependence of thermophysical properties [1].

For most thermophysical property measurements, the shape of the liquid metal droplet must be known for the interpretation of the results. This is one reason why it is desirable to have the ability to predict these shapes for a given coil geometry, applied current, and sample material. Development of a mathematical model of the shape of liquid metal droplets in electromagnetic levitation experiments also makes it possible to optimize the experiment parameters in order to achieve desired sample shapes and positions.

The surface tension and viscosity of selected undercooled metals will be measured in a microgravity experiment during the NASA IML-2 mission, which is scheduled to fly in 1994. The TEMPUS system is the electromagnetic levitation device that will be used to position and excite oscillations in the liquid metal droplets. A schematic sketch of the TEMPUS system is provided in Figure 3.1. Prediction of the sample shapes that will occur in the flight experiment will enable the precise measurement of thermophysical properties. A comparison of experimentally-determined and calculated shapes for two different metals is presented. This paper is designed to be a report on our progress in modeling the shape of levitated metal droplets, and discusses how we are addressing the complex issues involved.

3.2 FORMULATION AND COMPUTATIONAL METHODOLOGY

The two major computational tasks associated with modeling the equilibrium shape of an electromagnetically-levitated molten metal droplet are calculation of the magnetic field distribution in the droplet and calculation of the shape, which is determined by equilibrium of the component of stress normal to the surface of the droplet.

(i) Electromagnetic calculations

The magnetic field distribution in the levitated droplet is calculated using the method of mutual inductances presented by, among others, El-Kaddah and Szekely [3] and Zong et al. [4]. The axisymmetric levitated droplet is discretized into a set of annular electrical circuits through which induced current flows. Once the induced current distribution is calculated, the distribution of magnetic flux density can be calculated by taking the curl of the

distribution of vector potential, or by using the Biot-Savart law. Use of the Biot-Savart Law is preferable because it utilizes numerical integration as opposed to numerical differentiation, which is prone to numerical errors. The Biot-Savart Law was used in the calculations that provided the results presented here. This represents an improvement over the previous model.

The discretization of the droplet domain and the shape of the cross section of the annular circuits can be seen in Figure 3.2. Also visible is the exponential distribution of grid points used to better represent the distribution of magnetic flux density, which decays exponentially from the magnitude at the surface with distance into the droplet. In this paper an important modification to the calculation of mutual inductances between each pair of annular circuit elements, which have an approximately rectangular cross section, is made.

Maxwell's formula for the mutual inductance between two coaxial wires assumes that the cross section of the wires is circular. Following Dudley and Burke [5] and Burke et al. [6], Lyle's method is used to replace the approximately rectangular circuit elements with two representative locations at which Maxwell's formula can be applied. The mutual inductance between a pair of rectangular circuit elements is then found by averaging the mutual inductances calculated with Maxwell's formula at these locations. The method was further adapted to account for the fact that the sides of the approximately rectangular cross sections were not always oriented parallel and perpendicular to the axis of symmetry, as can be seen in Figure 3.2. Furthermore, a formula from Burke et al. [6] is used to calculate the self-inductance of the annular circuit elements of approximately rectangular cross section.

(ii) Free surface shape calculations

There are two self-consistent methods by which the equilibrium shape of an electromagnetically-levitated molten metal droplet has been modeled. The equilibrium shape is calculated either by balancing the normal stresses at each point on the free surface (known as the local method) [2,7-9] or by minimizing the total energy of the system (global method) [8,10-15].

Both models assume that the electromagnetic skin depth

$$\delta = \sqrt{\frac{2}{\omega\mu_o\sigma}} = \sqrt{\frac{1}{\pi\nu\mu_o\sigma}} \tag{3.1}$$

which characterizes the distance into the droplet of electrical conductivity σ that the external magnetic field of frequency ν can penetrate, is much smaller than the radius of the droplet, allowing the conclusion that internal fluid flow does not influence the free surface shape and can be ignored. In the case of very thin skin depth, the molten metal droplet behaves like a perfect conductor into which the magnetic field would not penetrate and in which no fluid flow would be driven.

In other words, it is assumed either that the flow is inviscid ($\mu = 0$) or non-existent ($\vec{u} = \vec{0}$). Either one of these assumptions is sufficient to eliminate the normal viscous stress from the free surface boundary condition.

Differences between the two modeling approaches largely concern the rate of convergence to the equilibrium shape. According to Bhamidipati and El-Kaddah [16], in the energy minimization technique, the displacement of the melt free surface from non-equilibrium to equilibrium shape is precisely defined in terms of the derivative of the variational statement of the energy functional of the system, thus ensuring rapid convergence. The local stress balance method, though simpler to implement, relies on arbitrary choice of displacement, and requires more iterations to obtain a converged solution.

(a) Normal stress balance method (Local method)

This method is the technique most frequently used in developing mathematical models of electromagnetic shaping operations, such as the shape of the meniscus in electromagnetic casting [16-22].

At equilibrium the net normal stress at all points along the free surface is zero. The normal component of the stress balance is given by

$$(p - p_a) + T_{nn} - \gamma\left(\frac{1}{R_1} + \frac{1}{R_2}\right) = 0 \tag{3.2}$$

Before considering the shape determination algorithm, it is useful to consider how the various physical phenomena contribute to the normal stress balance by examining the terms in Equation 3.2.

(1) Fluid pressure

The first term represents the difference between the pressure p and the atmospheric pressure. The contribution to the pressure due to gravity at any point in the droplet depends on the pressure at the top of the sample, the depth of the point, and the specific weight (ρg) of the fluid [23]. Pressure always acts from the liquid in the direction normal to a surface [23], therefore, the pressure exerts a normal force per unit area on the surface in the outward direction.

(2) Magnetic pressure

The second term is the normal stress component of the Maxwell stress tensor, representing the force per unit area exerted by the external magnetic field on the surface. Using index notation, the Maxwell stress tensor for incompressible and electrically linear media is given by [17]

$$T_{ij} = \mu H_i H_j - \frac{\mu}{2}\delta_{ij} H_k H_k \tag{3.3}$$

where μ is the magnetic permeability, H_i is the ith component of the magnetic field intensity, and δ_{ij} is the Kronecker delta. Using the summation convention and the fact that $\vec{B} = \mu_0 \vec{H}$ for the materials being studied, setting i and j equal to the normal coordinate n yields the magnetic pressure. The magnetic pressure only depends on the tangential component of the magnetic field because there is no component of magnetic field normal to the surface in the small skin depth approximation. In terms of the magnetic flux density, the magnetic pressure is [4]

$$p_m = T_{nn} = \frac{-B_t^2}{2\mu_o} \tag{3.4}$$

where B_t is the root-mean-square of the tangential component of the time-dependent magnetic flux density. For the case of the copper droplet levitated in the DLR conical coil arrangement considered in Section 2.6 and to be considered here, the maximum value of the magnetic pressure is about 1000 Pa for a magnetic flux density magnitude of about 0.05 T.

(3) Surface tension surface force density

The final term in the normal stress balance represents the surface force density due to surface tension [17]. The surface tension of the droplet is γ, and the two principal radii of curvature of the surface R_1 and R_2 are defined as positive for the outward-bulging surface [24]. The formulas used to calculate the principal radii of curvature in axisymmetric spherical coordinates are presented in [2]. The effect of surface tension at a given point is directed inward and normal to the surface.

The pressure contributes a normal force per unit area outward from the surface, while the magnetic pressure and surface tension surface force density exert an inward normal force per unit area.

The equilibrium free surface shape is calculated as follows [2,4]:

(i) The magnetic flux density distribution inside the droplet is calculated using the method of mutual inductances and the Biot-Savart law, as described above, for the initial shape, a sphere.

(ii) The magnetic pressure and surface tension surface force density are calculated at a finite number of points on the surface. From these contributions, a stress imbalance at each of these points is calculated. Based on the algebraic sign conventions used above, this value will be negative at all points on the surface. (Note that this value will vary along the surface until the free surface shape which satisfies the equilibrium condition, Equation 3.2, is found.)

(iii) The surface-area weighted average stress imbalance for the surface is then calculated, after which the difference from this weighted average at each point on the surface is calculated. The difference will be positive at some points and negative at others. If the value is negative, this indicates that the magnitude of the stress imbalance at that point is greater than the magnitude of the weighted average stress imbalance, and the point should be moved inward (toward the center of the droplet).

(iv) Each point on the surface is moved in the radial direction along a line of constant angle (sometimes called a spine) by an amount proportional to the difference between the stress imbalance and the surface-area weighted average at that point. This ensures that the volume of the droplet will be conserved. A new shape is determined by these displacements of the surface.

(v) The sum of the squares of the differences between the stress imbalance and the weighted average at all points along the surface is calculated as an indicator of how much the current free surface shape deviates from the equilibrium shape. A sum of squares is used to prevent positive and negative values from canceling each other and falsely suggesting that equilibrium has been achieved. When this sum of squares is less than a critical value, the equilibrium shape has been found to within a given tolerance. If this condition is not satisfied, then the procedure is repeated.

The results presented in this paper were obtained using the normal stress balance method.

(b) Energy minimization (Global method)

The equilibrium shape of the free surface, resulting from a balance among magnetic pressure, surface tension, and gravity forces, is governed by the equation [11]

$$\frac{B^2}{2\mu_o} + \gamma K + \rho g z = const. \tag{3.5}$$

where B is the root-mean-square magnitude of the local magnetic field, and K is the sum of the principal radii of curvature of the droplet.

An energy functional for the variational technique is defined which represents the total energy of the system. For droplet domain Ω and free surface boundary $\partial\Omega$, the energy functional is [11]

$$\phi(\Omega) = -\iiint_{R^3} \frac{B^2}{2\mu_o} dv + \iint_{\partial\Omega} \gamma ds + \iiint_{\Omega} \rho g z dv \tag{3.6}$$

In order to minimize the total energy with respect to the constant volume constraint on the droplet, a new functional using the Lagrange multiplier λ is defined. It is given by [12]

$$\psi(\Omega) = \phi(\Omega) - \lambda \iiint_{\Omega} dv \tag{3.7}$$

where λ is expressed as [12]

$$\lambda = \frac{\iint_{\partial\Omega} \left(\frac{B^2}{2\mu_o} + \gamma K + \rho g z \right) ds}{\iint_{\partial\Omega} ds} \tag{3.8}$$

Using the global method, the equilibrium free surface shape is calculated as follows [8]:

(i) The magnetic flux density distribution at the surface of the droplet is calculated by considering elements at the surface and the region outside the droplet, which is made possible by the assumption of small or zero skin depth. The initial shape is a sphere.

(ii) The magnetic energy, surface energy, and gravitational energy are calculated along $\partial\Omega$.

(iii) The Lagrange multiplier for the surface is calculated using Equation 3.8. Note that λ is the surface-area weighted average free energy for the surface, and is completely analogous to the surface-area weighted stress imbalance calculated in step (iii) of the normal stress balance method above.

(iv) The displacement of the surface effected reduces $\psi(\Omega)$ with magnitude determined by an adjustable coefficient that permits rapid convergence.

(v) If the derivative of the functional with respect to the domain, $\partial\psi / \partial\Omega$, is not sufficiently small, then the procedure is repeated.

3.3 EXPERIMENTAL WORK

The experiments were performed on pure nickel and copper droplets (Johnson Matthey, 99.99%) with mass of approximately 1 g. A detailed description of the levitation facility at DLR is given in [25]. A conical coil arrangement that provided stable levitation of the droplets was used. A sketch of the coil geometry, as well as the strength of the external magnetic field and magnetic field gradient on the symmetry axis of the coils for a peak applied current of I_0 = 405 A, which was used in the case of the nickel sample, is shown in Figure 3.3.

The RF-generator was operated at a frequency of 333 kHz. The peak applied coil currents were 405 A, in the case of nickel, and 310 A, in the case of copper. The samples were convectively cooled by He gas. Non-contact temperature measurement was performed with a standard two-color ratio pyrometer.

Experiments with nickel and copper droplets were performed in the same way. The droplet was levitated with the coil current given above. During levitation, the translational oscillation frequencies and the surface oscillation frequencies were measured using a method explained in [26] and [27]. The samples were then rapidly solidified by cooling with He gas. The volume

change upon solidification was assumed to be isotropic and, therefore, shape-preserving. Figure 3.4 shows a picture of a sample processed in this way. Next to this is a shape measured from a projection onto a grid and a fit of spherical harmonics

$$R(\psi) = R_o\left(1 + \sum_{l=1}^{n} \varepsilon_l Y_l^0(\psi)\right) \tag{3.9}$$

at the contour is shown to give an image of the distortion from spherical shape.

In order to eliminate the effect of "frozen-in" oscillations on the shape of the rapidly-solidified droplet, the mean values of measurements made on many levitated and solidified droplets were used to determine the experimentally-determined equilibrium shape. The measured coefficients of the spherical harmonics ε_l (with errors $\Delta\varepsilon_l$) are listed in Table 3.1.

An important application of the knowledge of the distortion of a levitated droplet is the influence on the surface oscillation modes of levitated droplets. In the oscillating drop technique, the frequencies of the surface oscillations are used to determine the surface tension of liquid metals. Due to gravity and a lack of spherical symmetry, the fundamental oscillation mode is split into a number of modes, each with its own frequency. The measurements then yield spectra with multiple peaks, with a maximum of five. Cummings et al. [28] and Suryanarayana et al. [29] have recently calculated the effect of distortion of the sample from a spherical shape on individual frequencies. According to Cummings [28] the frequencies of the five modes are expressed in terms of the Rayleigh frequency $\nu_R = \sqrt{8\gamma / 3\pi m}$ as

$$\begin{aligned}
\nu_{2,0} &= \nu_R(1 - 0.6758\varepsilon_2 - 2.1760\varepsilon_4) \\
\nu_{2,\pm1} &= \nu_R(1 - 0.3379\varepsilon_2 + 1.4507\varepsilon_4) \\
\nu_{2,\pm2} &= \nu_R(1 + 0.6758\varepsilon_2 - 0.3627\varepsilon_4)
\end{aligned} \tag{3.10}$$

with the coefficients ε_l defined in Equation 3.9. Both groups indicated that assignment of the modes is essential to obtaining precise results in the measurement of surface tension by this technique.

These results have been experimentally verified by Sauerland et al. [27] using digital image processing methods. Table 3.2 shows the good agreement between the splitting of the modes for the nickel sample in Figure 3.4 as predicted by Equation 3.10 and the measured oscillation frequencies.

To summarize, there is significant interest in having a tool to predict the deformation of droplets in levitation experiments because it would allow them to apply the theories of Cummings et al. and Suryanarayana et al. directly. This would enable prediction of the mode splitting that would result, facilitating assignment of oscillation modes and increasing the precision of surface tension measurements.

3.4 COMPUTED RESULTS

The equilibrium free surface shapes of molten liquid copper and nickel droplets were calculated using the input parameters listed in Table 3.3, which correspond to the experimental conditions described above. Plots of the experimentally-determined shape, indicated by a solid line, and the calculated shape, indicated by a dashed line, are provided for copper and nickel in Figures 3.5 and 3.6, respectively. In each figure the dotted line represents the shape of a sphere of equal volume.

From the figures it can be seen that the calculated shapes agree quite well with the experimentally-determined shapes, but it is important to realize that the visual comparison is quite flattering because the deformation of the droplet is relatively small. In each case the calculated shape correctly depicts the teardrop shape produced due to gravity in samples levitated under earthbound conditions.

3.5 DISCUSSION

The ability to predict, through mathematical modeling, the equilibrium free surface shape of electromagnetically-levitated droplets is important to the performance of surface tension measurements by the oscillating drop technique. This is quite a substantial undertaking due to the coupling of many complex phenomena, principally electromagnetic phenomena, free surface phenomena, and internal fluid flow.

In the normal stress balance model presented here, the small skin depth approximation was used in order to calculate the free surface shape of the sample by considering only the surface and neglecting the interior of the droplet. The ideal case for this model would then involve a sample of infinite conductivity (zero skin depth). However, in the cases of the copper and nickel droplets considered here, the skin depth is 13.08% of the radius for the copper droplet, and 25.55% of the radius for the nickel droplet. Both of these thereby constitute a deviation from the ideal case for this model.

This helps to interpret the results shown in Figures 3.5 and 3.6. In both cases, the calculated shape is less deformed than the experimentally-determined shape. The reason for this is that, since the sample has finite conductivity (and a nonzero skin depth to droplet radius ratio), there is some penetration of the field into the interior of the droplet. As a result, the magnitude of the magnetic pressure, calculated from the magnitude of magnetic flux density at the surface provides a lower bound estimate of the deforming effect of the magnetic field. A consideration of the skin depth-to-radius ratios for the two cases predicts the result that the calculated shape matches the experimental shape better in the case of copper than in the case of nickel.

Figures 3.5 and 3.6 show that the normal stress balance model provides a good estimate of the equilibrium free surface shape of levitated metal droplets. In order to achieve even better agreement, the computed results herein suggest that, when the ratio of skin depth to sample radius is not negligible, the interior of the sample must be considered. This finding is also useful for modeling the shapes of electromagnetically-shaped liquid metals in general. In order to model the free surface shape of a large pool of molten metal

subjected to electromagnetic forces, consideration of the surface is sufficient, however, in cases where the sample dimensions are small, as is often the case with meniscus control, the interior of the droplet must be considered.

3.6 ACKNOWLEDGEMENTS

The authors acknowledge the financial support provided by the National Aeronautic and Space Administration under contract number NAG8-815 and DARA, the German Aeronautics and Space Agency. One of the authors would like to acknowledge the financial support provided by the Department of Defense in the form of a National Defense Science and Engineering Fellowship. One of the authors acknowledges very useful discussions with many members of the MIT community, especially Prof. Markus Zahn, Prof. Alar Toomre, Mr. Robert Hyers, and Ms. Livia Racz.

3.7 REFERENCES

[1] I. Egry and J. Szekely, "The Measurement of Thermophysical Properties in Microgravity Using Electromagnetic Levitation," Adv. Space Res., 11(7)(1991), 263-266.

[2] E. Schwartz, J. Szekely, O.J. Ilegbusi, J-H. Zong, and I. Egry, "The Computation of the Electromagnetic Force Fields and Transport Phenomena in Levitated Metallic Droplets in the Microgravity Environment", MHD Symposium, 1992 TMS Meeting, San Diego, 81-87.

[3] N. El-Kaddah and J. Szekely, "The Electromagnetic Force Field, Fluid Flow Field, and Temperature Profiles in Levitated Metal Droplets", Metallurgical Transactions B, 14(1983), 401-410.

[4] J-H. Zong, J. Szekely, and E. Schwartz, "An Improved Computational Technique for Calculating Electromagnetic Forces and Power Absorptions Generated in Spherical and Deformed Body in Levitation Melting Devices", IEEE Transactions on Magnetics, 28(3)(1992), 1833-1842.

[5] R. Dudley and P.E. Burke, "The Prediction of Current Distribution in Induction Heating Installations", IEEE Transactions on Industry Applications, IA-8(5)(1972), 565-571.

[6] P.E. Burke, P.P. Biringer, P.F. Ryff, and E. Solger, "The Prediction and Measurement of Current Distribution in Coaxial Circular Geometries", 6th PICA Conference Proceedings (1969), 464-482.

[7] A.J. Mestel, "Magnetic Levitation of Liquid Metals", Journal of Fluid Mechanics, 117(1982), 27-43.

[8] A. Gagnoud, J. Etay, and M. Garnier, "The Levitation Melting Process Using Cold Crucible Technique", Transactions ISIJ, 28(1988), 36-40.

[9] D.W. Fugate and J.F. Hoburg, "Shape and Stability Comparisons of Electromagnetically Confined Liquid Metal Boundaries", Metallurgical Transactions B, 24(1993), 171-178.

[10] A.D. Sneyd and H.K. Moffatt, "Fluid Dynamical Aspects of the Levitation-Melting Process", Journal of Fluid Mechanics, 117(1982), 45-70.

[11] A. Gagnoud and M. Garnier, "Physical Analysis and Modelization of Phenomena in Electromagnetic Levitation in Conical Conductor", IEEE Transactions on Magnetics, 21(5)(1985), 1886-1888.

[12] A. Gagnoud and J.P. Brancher, "Modelling of Coupled Phenomena in Electromagnetic Levitation", IEEE Transactions on Magnetics, 21(6)(1985), 2424-2427.

[13] A. Gagnoud and I. Leclercq, "Free Boundary Problem in Electromagnetic Levitation Melting and Continuous Casting", IEEE Transactions on Magnetics, 24(1)(1988), 256-268.

[14] N. El-Kaddah and F.A. Acosta-Gonzalez, "Mathematical Model for the Shaping of Molten Metal by an Electromagnetic Field", Casting of Near Net Shape Products, Warrendale, PA, TMS, 1988, 423-437.

[15] N. El-Kaddah and T.T. Natarajan, "The Influence of Coil Design on Melt Shape in Electromagnetic Levitation Melting", Proceedings of the Sixth International Iron and Steel Congress, Nagoya, Japan, ISIJ, 1990, 380-387.

[16] J.R. Bhamidipati and N. El-Kaddah, "Calculation of Electromagnetic Field and Melt Shape in the Magnetic Suspension Melting Process", MHD Symposium, 1992 TMS Meeting, San Diego, 69-74.

[17] J. R. Melcher, Continuum Electromechanics, MIT Press, Cambridge, MA, 1981.

[18] D.N. Riahi and J.S. Walker, "Float Zone Shape and Stability with the Electromagnetic Body Force Due to a Radio-Frequency Coil", Journal of Crystal Growth, 94(1989), 635-642.

[19] B.Q. Li and J.W. Evans, "Computation of Shapes of Electromagnetically Supported Menisci in Electromagnetic Casters--Part I: Calculations in Two Dimensions", IEEE Transactions on Magnetics, 25(6)(1989), 4443-4448.

[20] T. Sato, S. Sugiyama, A. Yada, M. Nakada, K. Mori, and T. Osako, "Analytical and Experimental Investigation on Control of Molten Metal Surface in Continuous Casters under Magnetic Pressure", 1991 1st ASME-JSME Fluids Engineering Conference, Portland, Oregon.

[21] J.W. Evans, D.P. Cook, and S. Nishioka, "Mathematical and Physical Modeling of Electromagnetically Supported Melts in Three Dimensions", MHD Symposium, 1992 TMS Meeting, San Diego, 35-44.

[22] D.P. Cook, J.W. Evans, and J. Grandfield, "Application of a Mathematical Model in Thin Strip Electromagnetic Casting", MHD Symposium, 1992 TMS Meeting, San Diego, 145-149.

[23] P. Gerhart, R. Gross, and S. Hochstein, Fundamentals of Fluid Mechanics, Addison-Wesley Publishing Company, Reading, MA, 1992.

[24] L.M. Racz, J. Szekely, and K.A. Brakke, "A General Statement of the Problem and Description of a Proposed Method of Calculation for Some Meniscus Problems in Materials Processing", ISIJ International, 33(2)(1993).

[25] D.M. Herlach, R. Willnecker, and F. Gillessen, ESA SP-222 (1984), 399.

[26] I. Egry, "Surface Tension Measurements of Liquid Metals by the Oscillating Drop Technique", J. Mat. Science, 26(1991), 2997-3003.

[27] S. Sauerland, K. Eckler, and I. Egry, "High Precision Surface Tension Measurements on Levitated Aspherical Liquid Nickel Droplets by Digital Image Processing", Journal of Mat. Sci. Letters, 11(1992), 330.

[28] D.L. Cummings and D.A. Blackburn, "Oscillations of Magnetically Levitated Aspherical Droplets", J. Fluid Mech., 224(1991), 395.

[29] P.V.R. Suryanarayana and Y. Bayazitoglu, "Effect of Static Deformation and External Forces on the Oscillations of Levitated Droplets", Phys. Fluids A, 3(5)(1991), 967.

[30] H. Fukumoto, Y. Hosokawa, K. Ayata, and M. Morishita, "Numerical Simulation of Meniscus Shape Considering Internal Flow Effects", MHD Symposium, 1992 TMS Meeting, San Diego, 21-26.

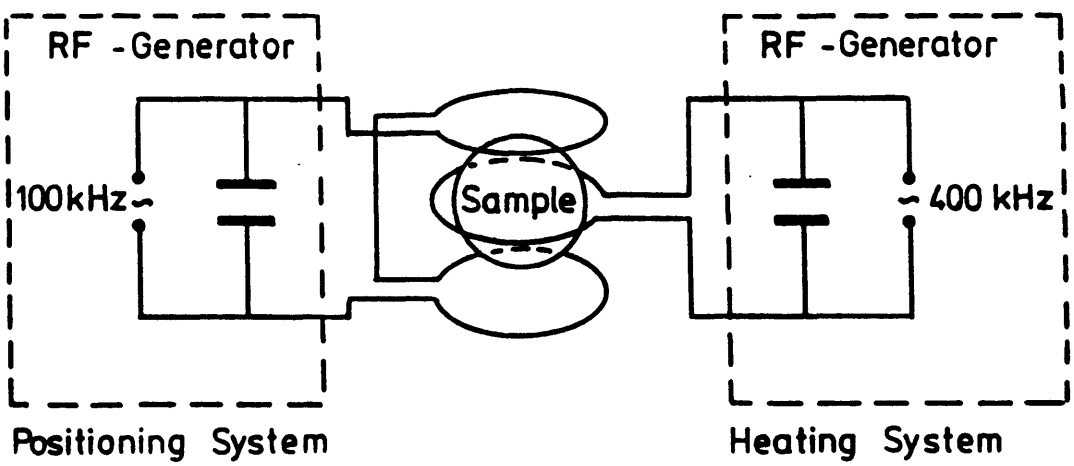

Figure 3.1 Schematic diagram of TEMPUS system with separate (a) positioning and (b) heating coil systems. Figure provided by I. Egry et al.

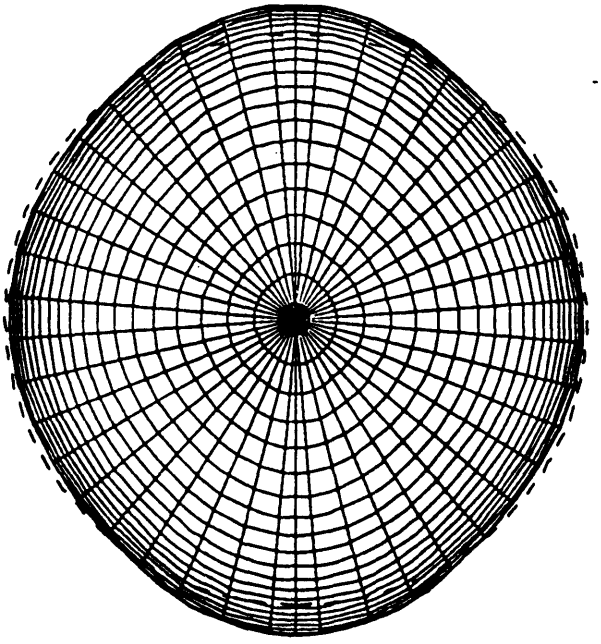

Figure 3.2 Discretization of droplet domain, showing exponential grid point distribution and rectangular cross section of annular circuit elements.

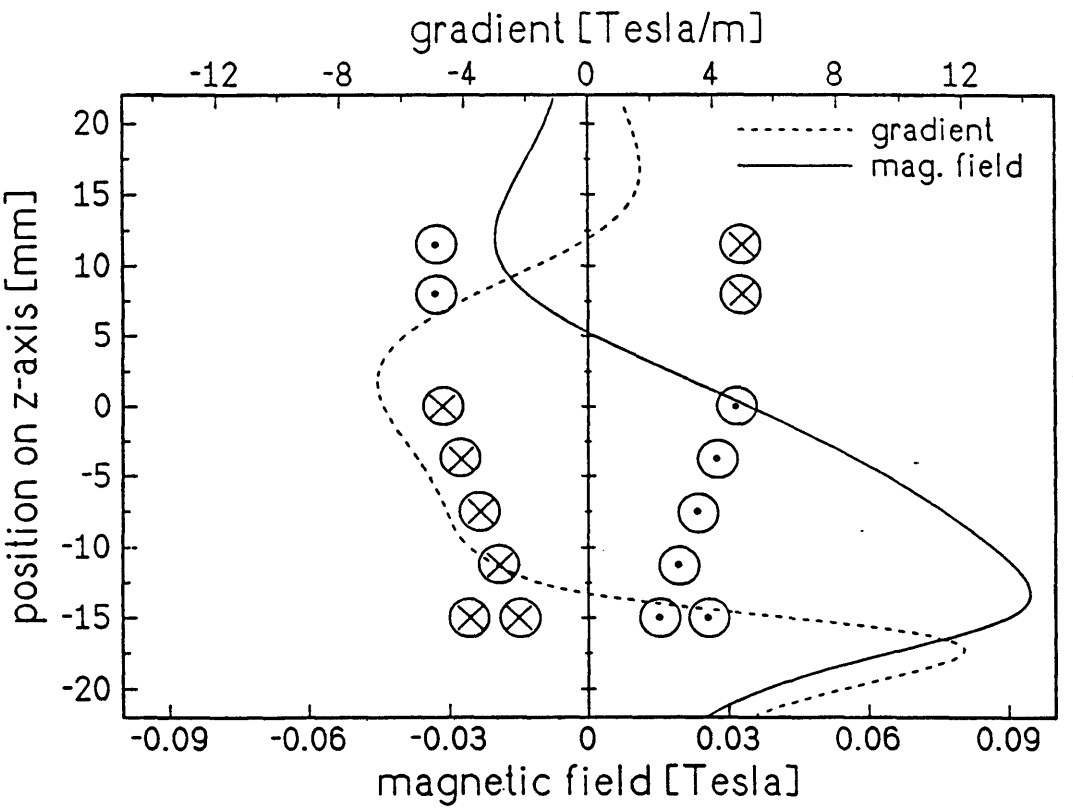

Figure 3.3 Conical coil arrangement with field strength and gradient along symmetry axis for peak applied current of I_0=405 A.

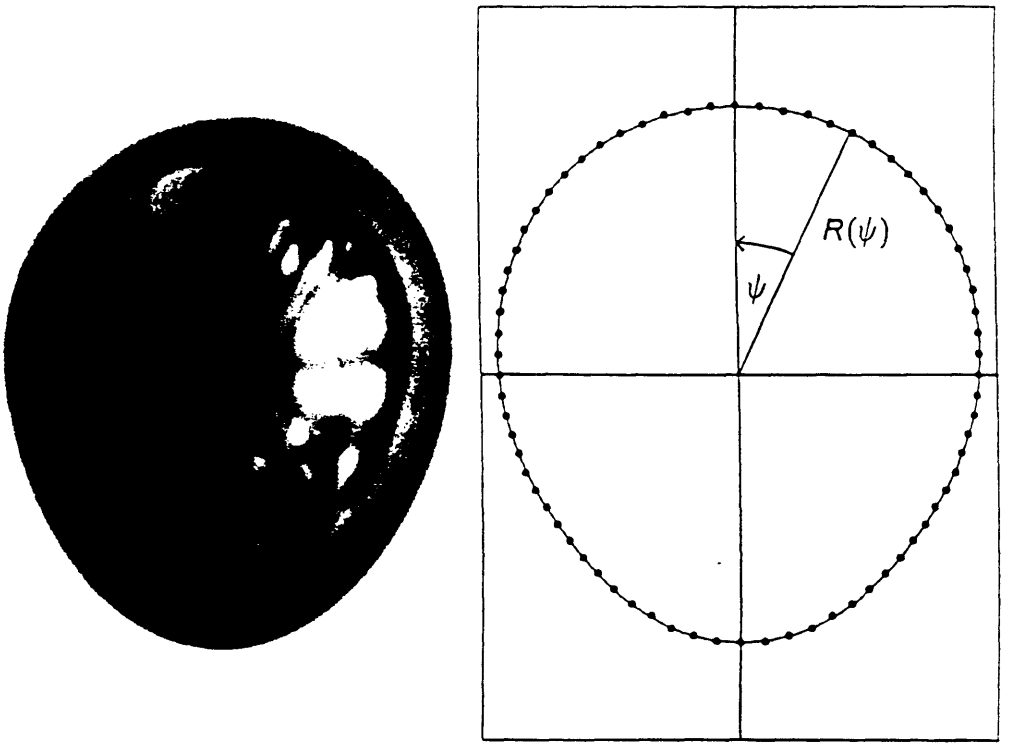

Figure 3.4 Fit of spherical harmonics to experimental shape.

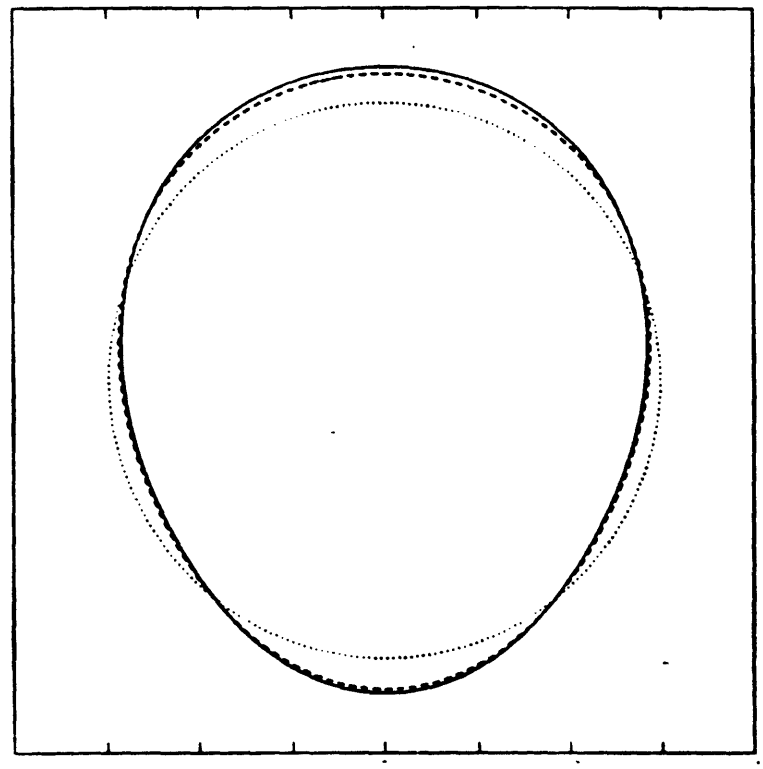

Figure 3.5 Comparison of calculated and experimental Cu droplet shapes.

..... Spherical shape

— Experimentally-determined shape

---- Calculated deformed shape

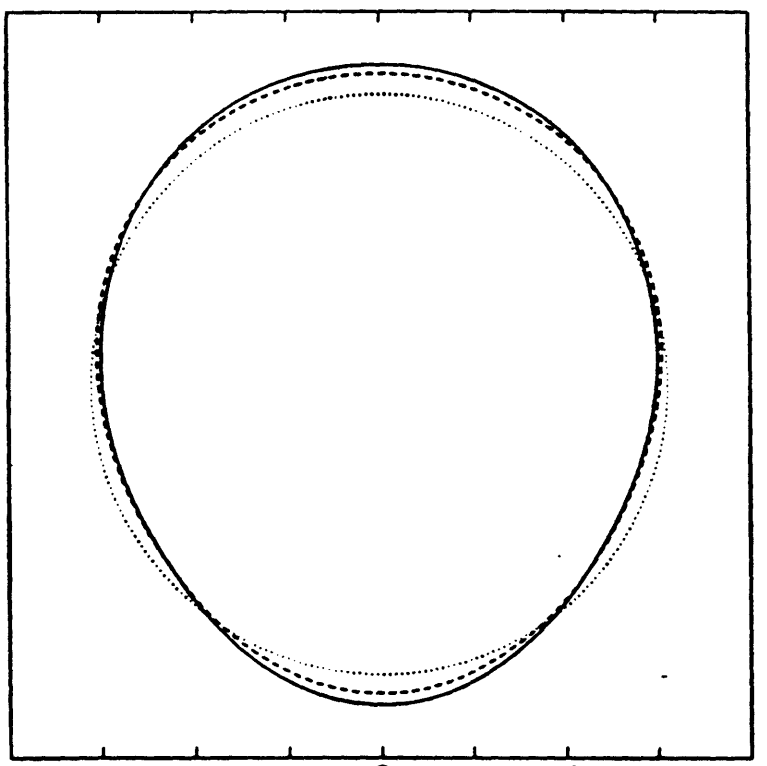

Figure 3.6 Comparison of calculated and experimental Ni droplet shapes.

..... Spherical shape

— Experimentally-determined shape

---- Calculated deformed shape

Table 3.1 Expansion coefficients of $R(\psi)$ for fit of experimental shape with spherical harmonics

l	ε_l	$\Delta\varepsilon_l$
0	3.545	0.007
1	0.088	0.006
2	0.141	0.006
3	-0.048	0.005
4	0.015	0.006
5	-0.004	0.006

Table 3.2 Comparison of experimental and theoretical splitting of oscillation modes

Mode n=2	$\nu_{2,0}/\nu_R$	$\nu_{2,\pm1}/\nu_R$	$\nu_{2,\pm2}/\nu_R$
Experimental	0.928	0.979	1.057
Theoretical	0.914	0.974	1.089

Table 3.3 Input parameters used for equilibrium free surface shape calculations

Parameter	Cu	Ni
Applied current (A)	310	405
Frequency (kHz)	333	333
Radius of sphere (mm)	2.982	3.11
Elec. cond. $(\Omega m)^{-1}$	5×10^6	1.205×10^6
Density (kg/m^3)	8106	8080
Surface tension (N/m)	1.45	1.82

CHAPTER 4

THE FREE SURFACE SHAPE AND TEMPERATURE DISTRIBUTION PRODUCED IN LIQUID METAL DROPLETS BY HEATING COIL PULSES IN THE TEMPUS EML

ABSTRACT

We present the results of analytical and numerical calculations of the free surface shape and temperature distribution produced in liquid metal droplets processed in the TEMPUS electromagnetic levitation (EML) facility. The mathematical models were developed to predict the behavior of liquid metal droplets in containerless experiments to determine measure thermophysical properties aboard the Space Shuttle during the IML-2 mission in July 1994. The normal stress balance model was used to numerically calculate the equilibrium free surface shape for various samples effected by a number of induction coil voltages. Analytical and numerical calculations were performed to model the heat transfer in liquid metal samples during and following the heating coil pulses. The work illustrates the use of mathematical modeling in the design of microgravity experiments.

4.1 INTRODUCTION

The purpose of this work was to develop mathematical models that made it possible to intelligently design a recent Spacelab IML-2 experiment performed to measure the viscosity and surface tension of undercooled metals. The experiment was performed in TEMPUS, an electromagnetic containerless processing facility which provides containerless positioning, heating, and melting of metallic samples. Thermophysical property measurements were made using the oscillating drop technique [1]. The surface tension could be deduced from the frequency of the oscillations [2], and the viscosity could be determined from the damping constant [3].

Figure 4.1 shows a schematic sketch of TEMPUS. It is seen that there are two sets of coils, an outer set used for positioning and an inner set employing higher frequencies to be used both for heating and for deforming the sample once it is molten. In the performance of an experiment, the sample was introduced from below into the space within the coils. The positioning coils were turned on first, and once the sample rested in a stable position, the

heating coils were turned on to melt the sample and bring it to a predetermined desired temperature above the melting point. At this point the heating coil voltage was switched off or reduced and the sample was allowed to cool. It was then squeezed and deformed by pulsing the inner, or heating, coils for 0.1 s. After the heating coil voltage was switched off again, the droplet relaxed to its original shape in an oscillatory fashion. These damped oscillations were observed and recorded for a period of 5 s, during which the sample continued to cool. The pulsing and observation procedure was repeated until the sample solidified in order to obtain thermophysical property measurements over a temperature range including temperatures in both the superheated and the undercooled regimes [4].

One of the key design parameters for the experiment was the heating coil pulse voltage. The normal stress balance model, detailed in [5], was developed to calculate the equilibrium free surface shape of an axisymmetric droplet of given material properties and volume produced by induction coils of arbitrary axisymmetric geometry, peak current, and frequency. As demonstrated in [5], the model provides a good estimate of the extent of deformation of liquid metal droplets.

Understanding of the non-uniform temperature distribution produced in a given droplet by the heating coil pulse was also important to the design of the experiment. The temperature gradients within a droplet are important for two major reasons:

(1) Significant temperature gradients along the droplet surface could induce Marangoni (surface tension-driven) flow. Because of the uncertain effect of fluid flow within the droplet on thermophysical property measurements and nucleation and solidification studies, any possible contribution to the flow field needed to be considered.

(2) In these containerless processing experiments, pyrometry was to be used to measure the temperature of the sample. Because each pyrometer, which has either a top or side view of the sample, focused on only a small area of the sample, it was important to know how well the measured temperature would represent the temperature of the droplet as a whole and at various points in the droplet.

4.2 FORMULATION AND COMPUTATIONAL METHODOLOGY

The two major computational tasks considered here are the calculation of the equilibrium free surface shape and the internal temperature distribution of various samples to be flown in TEMPUS as a function of the heating coil voltage.

(i) Free surface shape calculations

The normal stress balance model was used to calculate the equilibrium free surface shapes of samples to be processed in TEMPUS as a function of the heating coil voltage. According to this model, which is explained thoroughly in [5], the equilibrium shapes are calculated iteratively subject to an equilibrium condition of zero net normal stress at a number of discrete points along the free surface. The key feature of this approach is that all of the phenomena which together determine the droplet shape (hydrostatic pressure, gravity, magnetic field, and surface tension) are only evaluated at the droplet surface. In other words, only the surface of the droplet is considered, while the interior of the droplet is neglected.

This approach therefore makes the assumption that the electromagnetic skin depth

$$\delta = \sqrt{\frac{2}{\mu_o \sigma_{el} \omega}} \tag{4.1}$$

which quantifies the distance into a conducting material with electrical conductivity σ_{el} that an applied magnetic field of angular frequency ω diffuses, is much smaller than the radius of the droplet. The ratio of electromagnetic skin depth to the characteristic length (droplet radius) indicates the portion of the droplet that is subject to significant electromagnetic forces. For the samples processed in TEMPUS, the skin depth is on the order of 10% of the droplet radius, indicating that the applied field is shielded from much of the interior of the droplet. Consequences of this zero skin depth approximation were discussed in [6] and will be addressed later in this paper.

The normal component of the stress balance at the free surface is given by

$$(p - p_a) + p_m - \gamma\left(\frac{1}{R_1} + \frac{1}{R_2}\right) = 0 \tag{4.2}$$

The first term represents the difference between the fluid pressure p and the atmospheric pressure p_a. The second term represents the magnetic pressure p_m, which depends on the temporal average of the tangential component of the magnetic flux density. The final term is the pressure due to surface tension γ, where R_1 and R_2 are the principal radii of curvature [5].

In each iteration the magnetic flux density (and magnetic pressure) distribution is re-calculated using the method of mutual inductances [7-9] and the Biot-Savart law. The equilibrium shape is calculated iteratively by radial movement of discrete points on the surface along spines.

(ii) Heat transfer calculations

The temperature distribution in the droplet throughout the duration of the heating coil pulse and following it are calculated with the transient thermal energy balance equation. The governing equation, with internal fluid flow (convective heat transfer within the droplet) neglected, takes the form

$$\frac{\partial T}{\partial t} = \alpha \nabla^2 T + \frac{Q(r,\theta)}{\rho C_p}, 0 \le t \le 0.1s \tag{4.3}$$

$$\frac{\partial T}{\partial t} = \alpha \nabla^2 T, t > 0.1s \tag{4.4}$$

where T is the temperature, α and C_p are the thermal diffusivity and heat capacity of the molten metal droplet, and $Q(r,\theta)$ is the heat generated in the droplet per unit volume by induction from the heating coils. The heat generated in the droplet comes from dissipation of energy from the induced currents. The time-averaged distribution of induction (Joule) heating per unit volume is given by [4]

$$Q(r,\theta) = \frac{1}{\tau}\int_0^{\tau} \frac{\vec{J}\cdot\vec{J}}{\sigma_{el}} dt = \frac{1}{2}\mathrm{Re}\frac{\hat{\vec{J}}\cdot\hat{\vec{J}}^*}{\sigma_{el}} \tag{4.5}$$

where $\vec{J}$ is the current density, expressed as in Equation 2.64, τ is the period of the applied alternating current, Re indicates the real part of the complex quantity, and an asterisk designates the complex conjugate.

Substantial heating occurs only when the higher-frequency, or heating, coils are on, which is the voltage pulse of the 0.1 s duration. The heat generated by lower-frequency, or positioning, coils is less than 10% of that generated by the heating coils are is therefore not considered here. Constant values for the material properties were used because of the small temperature range being considered and the weak temperature dependence of the properties.

The boundary condition at the free surface of the droplet expresses heat losses by conduction to the inert gas surrounding the droplet and by radiation:

$$-k_s \frac{\partial T}{\partial n} = (h_{cond} + h_{rad})(T - T_c) \tag{4.6}$$

where k_s is the thermal conductivity of the molten metal sample, n is the curvilinear coordinate normal to the free surface, h_{cond} is the conduction heat transfer coefficient, h_{rad} is the radiation heat transfer coefficient, and T_c is the temperature of the water-cooled coils.

Heat is lost by conduction from the hot surface of the droplet through the inert gas to the water-cooled coils. In order to develop an expression for h_{cond}, the coils were modeled as a spherical shell surrounding the approximately-spherical droplet. Calculation of the Fourier number indicates whether a steady-state approximation for the temperature distribution in the inert gas is appropriate. The Fourier number represents the ratio of the heat conduction rate to the rate of thermal energy storage in the gas [10]. The Fourier number is

$$Fo = \frac{\alpha t}{L^2} \tag{4.7}$$

where α is the thermal diffusivity of the gas, t is the period of time being considered, and L is the average distance between the sample surface and the water-cooled coils. For the atmosphere of very low pressure (2 mbar) Ar gas used in some of the TEMPUS experiments, the Fourier number is on the order of 10^3, indicating that the fast conduction keeps the temperature in the gas next to the hot sample surface virtually the same as the temperature of the sample surface at any given time. The fact that there is no lag behind the changing surface temperature permits a steady-state approximation of the temperature distribution in the gas.

Because of the very low gas pressure, it was also necessary to determine whether a continuum approach to the steady-state conduction problem was possible. The Knudsen number

$$Kn = \frac{\lambda}{L} \tag{4.8}$$

compares the molecular mean free path λ with the characteristic length L, which is again taken to be the average distance between the sample surface and the coils. Because the Knudsen number is less than 0.05 for the temperatures of interest, continuum theory is in fact appropriate [11].

The analytical result for radial conduction between concentric spheres is

$$ODE: \quad \frac{d}{dr}\left(r^2 \frac{dT}{dr}\right) = 0 \tag{4.9}$$

$$BC1: \quad T = T_s, R = R_s \tag{4.10}$$

$$BC2: \quad T = T_c, R = R_c \tag{4.11}$$

$$Solution: \quad T(r) = T_s + \frac{R_c(r - R_s)}{r(R_c - R_s)}(T_c - T_s) \tag{4.12}$$

$$Flux: \quad q_{cond} = -k_f \frac{dT}{dr}, R = R_s \tag{4.13}$$

where T_s is the temperature of the sample at its surface, R_s is the radius of the sample, T_c is the temperature of the coils, R_c is the average radial distance of the coils from the center of the sample, and k_f is the thermal conductivity of the inert gas. The heat flux at the surface is related to the heat transfer coefficient by the expression

$$q = h(T - T_c) \tag{4.14}$$

Using the expression obtained from Equation 4.13, an expression for the conduction heat transfer coefficient was obtained.

The radiative heat flux from the droplet surface is

$$q_{rad} = \varepsilon\sigma_{SB}(T_S^4 - T_C^4) \tag{4.15}$$

where ε is the total hemispherical emissivity and σ_{SB} is the Stefan-Boltzmann constant. Using Equation 4.14 an expression for the radiation heat transfer coefficient was obtained.

Calculation of the Biot number provides an immediate sense of the magnitude of temperature differences within a body undergoing transient heat conduction. The Biot number represents the ratio of internal thermal resistance to boundary layer thermal resistance [10], i.e., the ratio of the resistance to conduction within the concerned body to the resistance to heat transfer to the surroundings. The Biot number is

$$Bi = \frac{h_{tot}L}{k_s} \tag{4.16}$$

where h_{tot} is the total heat transfer coefficient, the sum of the conduction and radiation heat transfer coefficients shown above, L is the characteristic length for conduction within the body, and k_s is the thermal conductivity of the conducting body. For samples processed in TEMPUS, the Biot number is on the order of 0.01, indicating that temperature differences within the sample are quite small and that a lumped parameter approach can be used to develop an approximate analytical solution for the droplet temperature.

By performing a heat balance, we can estimate the temperature of the droplet during the heating coil pulse by considering that the rate of energy accumulation in the droplet is equal to the difference between the power absorbed by induction and the rate of energy lost at the surface. From the expression

$$\Delta T = \frac{Q - (q_{cond} + q_{rad})A}{mC_p} \Delta t \tag{4.17}$$

where A is the surface area and m is the mass of the droplet, it could be determined that the average temperature of droplets increases about 1-2°C from the heating coil pulse. The lumped-parameter approach could also be used to estimate the cooling rate after the heating coils are shut off. From the first-order differential equation

$$mC_p \frac{dT}{dt} = -(h_{cond} + h_{rad})A(T - T_c) \tag{4.18}$$

the cooling rate of samples processed in TEMPUS was estimated to be on the order of 10°C/s.

Other considerations:

(1) Forced convection

The time scale for conductive heat transfer under laminar flow conditions is

$$\tau_{cond} = \frac{L^2}{\alpha} \tag{4.19}$$

For samples processed in TEMPUS, this time scale is on the order of 1 s. However, if the flow is turbulent and the momentum transfer involves laminarization, estimation of the time scale is much more involved. A lower limit for the time scale can be obtained by using an effective thermal diffusivity in Equation 4.19 [10]. Using an effective value of the quantities that is from 10 to 50 times greater than the laminar values yields a conduction

time scale on the order of 0.01-0.1 s. This time scale is of the same order of magnitude as the time scale for forced convection

$$\tau_{conv} = \frac{L}{U} \tag{4.20}$$

when U is the magnitude of the maximum velocity driven by electromagnetic forces created by the heating coil pulse.

The Peclet number provides a comparison of heat transfer by forced convection with heat transfer by conduction within a moving fluid. The Peclet number

$$Pe = \frac{UL}{\alpha} \tag{4.21}$$

varies significantly for samples processed in TEMPUS because of the variable flow conditions. When the flow becomes turbulent at the end of the 0.1 s heating coil pulse, the value of the Peclet number is unclear because the conduction is enhanced by the turbulence along with the convection. In any case, the electromagnetically-driven flow should cause homogenization of the temperature distribution within the droplet.

(2) Natural convection

The Rayleigh number

$$Ra = Gr\,\mathrm{Pr} = \frac{gL^3\beta\Delta T}{\nu\alpha} \tag{4.22}$$

where β and ν are the thermal expansion coefficient and the kinematic viscosity of the molten metal and ΔT is the maximum temperature difference within the sample, compares the heat transfer by natural convection with that by conduction. The Rayleigh number plays the same role in natural convection as the Peclet number plays in forced convection [10]. Under microgravity conditions and with the small samples being processed, the Rayleigh number for samples processed in TEMPUS aboard the Space Shuttle

is less than 10^{-5}, indicating that heat transfer by natural convection is negligible.

(3) Reflected radiation

As stated above, one of the mechanisms of heat transfer from the sample is radiation. Some of the emitted heat must be reflected off the surrounding induction coils and absorbed by the sample. In order to assess whether the absorbed power is significant, view factor and radiosity calculations were performed. Two different geometrical representations of the coils as cylindrical bands surrounding the spherical sample, shown in Figure 4.2, were developed so that view factors could be calculated. The ratio of absorbed power H_B to emitted power W_B for the sample is

$$\frac{H_B}{W_B} = \frac{\sum_{j=1}^{n} F_{ij} B_j}{\varepsilon_i \sigma_{SB} T_i^4} \tag{4.23}$$

where F_{ij} represents the matrix of view factors and the radiosity, or total heat flux leaving a surface j, is defined by

$$B_j = \varepsilon_j \sigma_{SB} T_j^4 + \left(1 - \varepsilon_j\right) \sum_{k=1}^{n} F_{jk} B_k \tag{4.24}$$

For the samples processed in TEMPUS, the absorbed power was found to be less than 10% of the emitted power when using either of the geometrical models, which means that the power absorbed by the sample is not very significant.

4.3 COMPUTED RESULTS

The equilibrium free surface shapes of molten metal droplets produced by various heating coil voltages in TEMPUS were calculated using a FORTRAN program based on the normal stress balance model. The amount of deformation produced is expressed by the quantity percentage deformation from a spherical shape, as calculated by the formula

$$\%def. = \frac{\left(z_{top} - z_{bottom}\right) - 2R}{2R} \times 100\% \tag{4.25}$$

where R is the radius of the undisturbed sphere of equal volume.

The material properties of the samples used as parameters in the free surface shape calculations were the surface tension, electrical conductivity, and density of each liquid metal at the melting point. The radius of a sphere of equal volume was also an input parameter. The values of these parameters for each of the five samples considered are shown in Table 4.1. Other input parameters for the calculations were the gravitational acceleration thought to exist during the Space Shuttle experiment (3×10^{-3} g_o), the frequencies of the positioning coils (148 kHz) and heating coils (388 kHz), as well as the peak current corresponding to the heating coil voltage for the given case.

The free surface shapes for Cu, $Au_{56}Cu_{44}$, Au, and Ni samples in the TEMPUS system with a positioning coil voltage of 6 V and heating coil voltages of 0 V, 2 V, 3.5 V, and 5 V were calculated. The computational results for each of the four samples are presented in Figures 4.3-4.6. The results are summarized in terms of the percentage deformation, as listed in Table 4.2.

The finite element computational package FIDAP was used to perform the numerical solution of the transient thermal energy balance subject to the boundary condition at the free surface. The distribution of power absorbed by induction was supplied to FIDAP through the user-supplied subroutine USRSRC for the duration of the heating coil pulse. The conduction and radiation heat transfer coefficients for each element along the free surface were re-calculated for each time step in the user-supplied subroutine USRCNV.

Figures 4.7-4.10 show calculated temperature-time profiles for four samples subjected to a 3 V heating coil pulse of 0.1 s duration in TEMPUS. The initial condition used in each case was that of a liquid droplet at its melting temperature. The temperature was taken to be uniform throughout the

droplet at t=0 s, the start of the heating coil pulse. The temperature of the droplet at its center, top, and equator was calculated as a function of time during and after the heating coil pulse. The results of the analytical solution shown in Equations 4.17 and 4.18 represent the average temperature of the sample and provide a confirmation of the sensibility of the numerical results. The calculated temperature profile at the end of the heating coil pulse for the nickel droplet is shown in Figure 4.11.

4.4 DISCUSSION

As explained in [5], the ratio of electromagnetic skin depth to droplet radius is the key parameter to the accuracy of the results obtained from the normal stress balance model. Because the model implicitly assumed that all phenomena that affect the equilibrium free surface shape, including the magnetic field, only need to be considered at the surface, the model is only exact in the case of a sample with infinite electrical conductivity (zero skin depth). In the cases considered here, the ratio of skin depth to droplet radius is nonzero, a point that was considered when the results of the equilibrium shape calculations were evaluated with the intent of planning the in-flight experiment.

In both cases presented in [5], the calculated shape was less deformed than the experimentally-determined shape, with the agreement between calculation and experiment being better in the case with the smaller skin depth-to-radius ratio, the case that was closer to "ideal". In the case of a sample with a ratio of 25.55%, the predicted extent of deformation was 7%, while the actual deformation was 10.5%. In the case of sample with a ratio of 13.08%, which is larger than that for all but one of the cases considered here, the predicted extent of deformation was 11%, while the actual extent of deformation was 13%. The skin-depth-to-radius ratios for the samples are given in Table 4.2.

Keeping in mind that the actual deformation will be greater than that predicted by calculations using the normal stress balance model, the heating coil voltage needed to effect the desired extent of deformation from a spherical shape of approximately 10% was sought. The results in Table 4.2

suggest that a heating coil voltage of 3 V would be sufficient, in the five cases considered here, to achieve the desired extent of deformation.

Figures 4.7-4.10 illustrate the temperature distribution produced in each sample by a 3 V heating coil pulse of duration 0.1 s. Due to the concentration of induced currents in the skin depth region at the equator of the droplet, where the magnetic field is strongest, the temperature at the equator increases during the heating coil pulse. At the top of the droplet, less power is induced, therefore, the temperature increases less strongly or even decreases (as in the case of Ni) there even during the heating coil pulse. Because of the time required for heat to be conducted from the center of the droplet to the surface and the lack of induced power at the center, the temperature there during the heating coil pulse is always less than that at the equator and greater than that at the top.

After the heating coil pulse ends, heat is conducted from the hottest area of the droplet (the equator) to the colder areas (the center and top). The temperature at the center of the droplet can be seen to increase slightly after the end of the heating coil pulse due to this temperature homogenization. After a time on the order of 1 s, the effect of the heating coil pulse has disappeared and the isotherms within the droplet are concentric spheres. This is why the temperature at the equator and top of the droplet are nearly identical and slightly lower than the temperature at the center of the droplet at any given time.

The largest possible temperature difference within the sample exists at the end of the heating coil pulse. Without considering convective heat transfer from the electromagnetically-driven flow in the droplet, the maximum temperature difference in all cases considered is less than 10°C. As stated above, the fluid flow contributes to homogenization of the temperature distribution within the droplet, therefore, it can be concluded that the temperature differences in molten droplets processed in TEMPUS are very small.

For a spherical droplet the magnitude of the fluid velocity induced by Marangoni convection has been approximated by [12-13]

$$U_r = \frac{\Delta\gamma}{8\mu} \tag{4.26}$$

where $\Delta\gamma$ is the difference in surface tension between the "cold" and "hot" portions of the droplet. For droplets processed in TEMPUS, because of the small temperature differences, the magnitude of this velocity is on the order of 1 cm/s. This result suggests that Marangoni convection is not likely to be important in this system. In addition, the small temperature differences within the sample suggest that the temperature measured by the pyrometers will accurately depict the temperature of the entire droplet when it is molten.

4.5 ACKNOWLEDGEMENTS

The authors acknowledge the financial support provided by the National Aeronautic and Space Administration under contract numbers NAG8-815, NAG8-970, and NAG8-1078. One of the authors also gratefully acknowledges useful discussions with Prof. Andreas Alexandrou of WPI and Dr. Tom Josinski of Creare, Inc.

4.6 REFERENCES

[1] I. Egry and J. Szekely, "The Measurement of Thermophysical Properties in Microgravity Using Electromagnetic Levitation", Adv. Space Res., 11 (7) (1991), 263-266.

[2] J. W. S. Rayleigh, "On the Capillary Phenomena of Jets", Proceedings of the Royal Society of London, 29 (1879), 71-97.

[3] H. Lamb, "On the Oscillations of a Viscous Spheroid", Proceedings of the London Math. Society, 13 (1) (1881), 51-66.

[4] E. Schwartz and J. Szekely, "Mathematical Modeling: An Essential Component of the Design of Space Experiments", to be published in Materials Processing in the Computer Age II, TMS, Las Vegas, 1995.

[5] E. Schwartz, S. Sauerland, J. Szekely, and I. Egry, "On the Shape of Liquid Metal Droplets in Electromagnetic Levitation Experiments", Containerless Processing: Techniques and Applications, TMS, Denver, 1993, 57-64.

[6] E. Schwartz and J. Szekely, "The Shape of Liquid Metal Droplets in Electromagnetic Levitation Experiments Considering Internal Fluid Flow", Experimental Methods for Microgravity Materials Science, TMS, San Francisco, 1994, 73-79.

[7] N. El-Kaddah and J. Szekely, "The Electromagnetic Force Field, Fluid Flow Field, and Temperature Profiles in Levitated Metal Droplets", Metallurgical Transactions B, 14 (1983), 401-410.

[8] J-H. Zong, J. Szekely, and E. Schwartz, "An Improved Computational Technique for Calculating Electromagnetic Forces and Power Absorptions Generated in Spherical and Deformed Body in Levitation Melting Devices", IEEE Transactions on Magnetics, 28 (3) (1992), 1833-1842.

[9] J. A. Dantzig and S. P. Midson, "Billet Heating for Semi-Solid Forming", Proceedings of the Second International Conference on the Processing of Semi-Solid Alloys and Composites, TMS, 1992, 105-118.

[10] F. P. Incropera and D. P. DeWitt, Fundamentals of Heat and Mass Transfer, Third Edition, John Wiley & Sons, New York, 1990.

[11] G. K. Bienkowski, Kinetic Theory Analysis of Problems in the Transitional Range of Knudsen Numbers, Ph.D. Thesis, MIT, 1962.

[12] D. M. Herlach, R. F. Cochrane, I. Egry, H. J. Fecht, and A. L. Greer, "Containerless Processing in the Study of Metallic Melts and Their Solidification", International Materials Reviews, 38 (6) (1993), 273-347.

[13] Y. Malmejac and G. Frohberg, "Mass Transport by Diffusion", Fluid Sciences and Materials Science in Space, edited by H. U. Walter, , New York, 1987, 159-190.

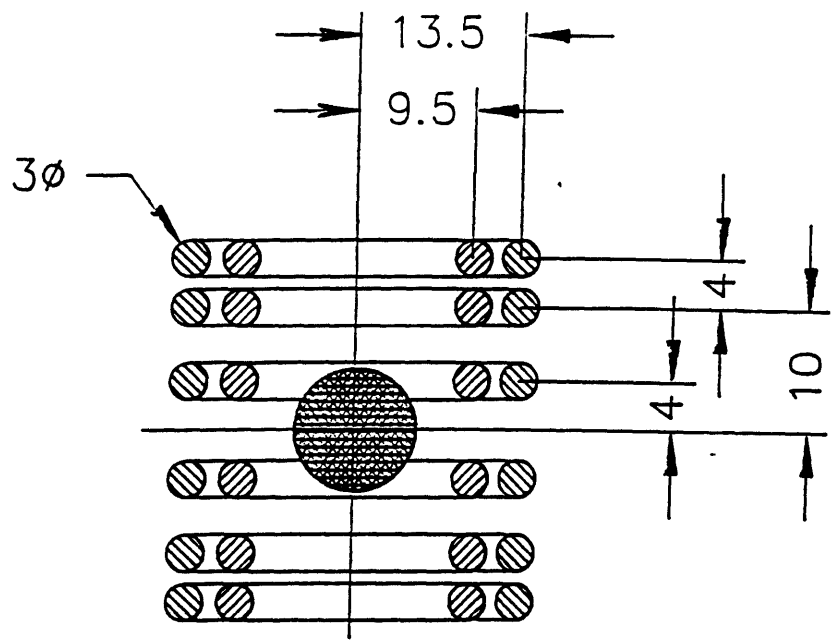

Figure 4.1 Schematic cut-through of TEMPUS coil geometry (distances in mm). Inner four coils produce dipole field for heating and deforming samples. Outer eight coils produce quadrupole for positioning. Figure provided by I. Egry et al.

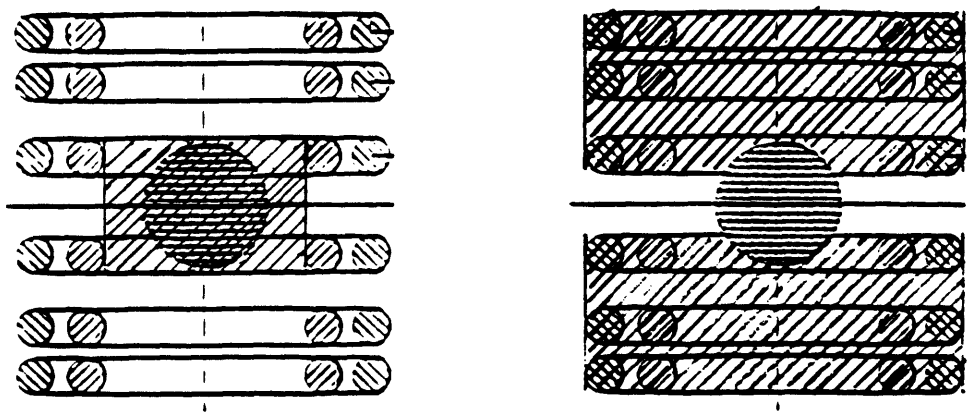

Figure 4.2 Geometrical representations of coils as (a) single heating coil band and (b) two cylindrical bands composed of coils above and below sample for view factor and radiosity calculations to compare absorbed power to emitted power.

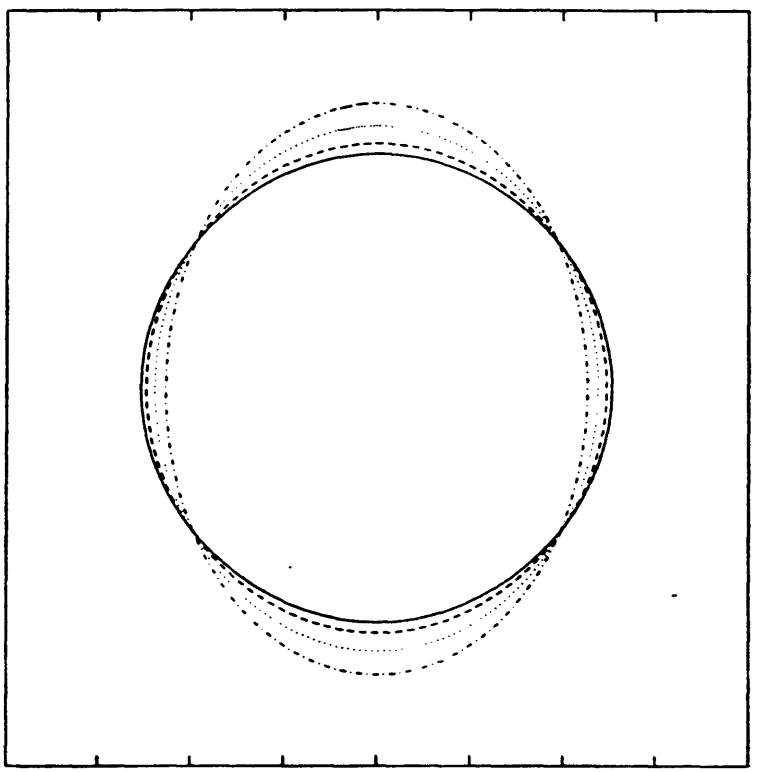

Figure 4.3 Calculated equilibrium free surface shapes of 10 mm diameter Cu sample levitated in TEMPUS with heating coil voltages of 0 V(solid line), 2 V (dashed line), 3.5 V (dotted line), and 5 V (dashdot line). Positioning coil voltage is 6 V for all cases. The percentage deformation for each case appears in Table 4.2.

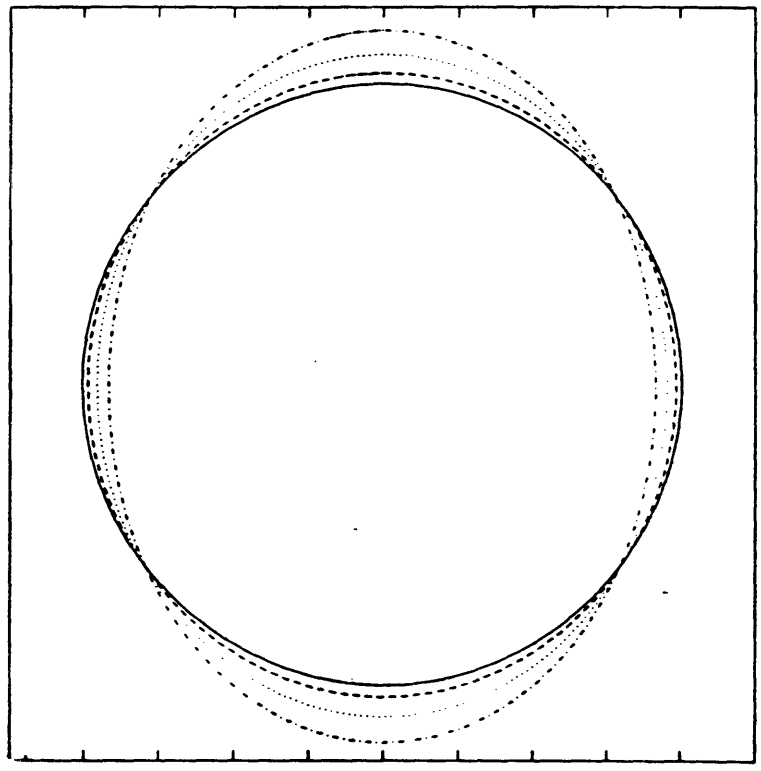

Figure 4.4 Calculated equilibrium free surface shapes of 8 mm diameter $Au_{56}Cu_{44}$ sample levitated in TEMPUS with heating coil voltages of 0 V (solid line), 2 V (dashed line), 3.5 V (dotted line), and 5 V (dashdot line). Positioning coil voltage is 6 V for all cases). The percentage deformation for each case appears in Table 4.2.

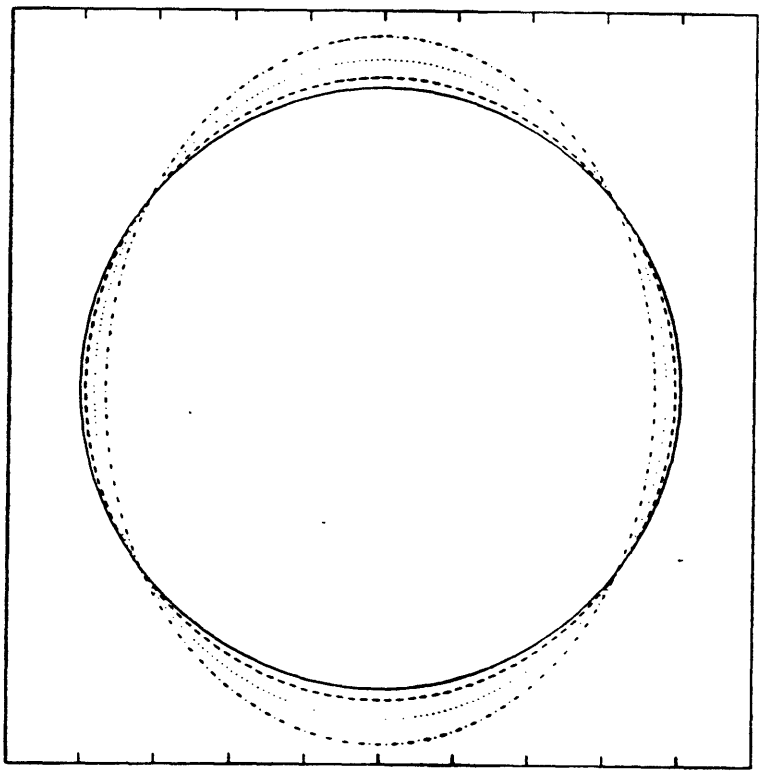

Figure 4.5 Calculated equilibrium free surface shapes of 8 mm diameter Au sample levitated in TEMPUS with heating coil voltages of 0 V (solid line), 2 V (dashed line), 3.5 V (dotted line), and 5 V (dashdot line). Positioning coil voltage is 6 V for all cases. The percentage deformation for each case appears in Table 4.2.

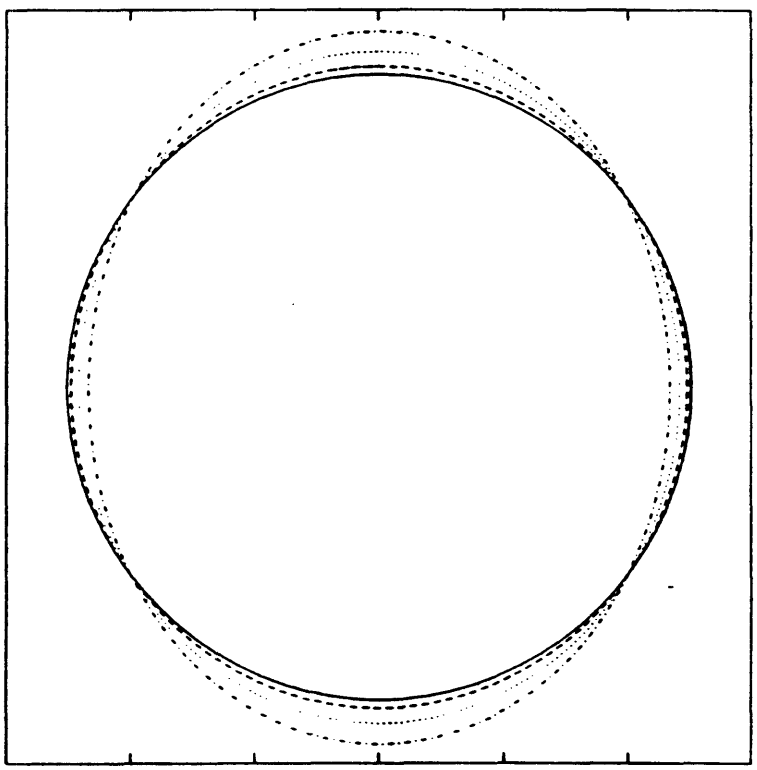

Figure 4.6 Calculated equilibrium free surface shapes of 10 mm diameter Ni sample levitated in TEMPUS with heating coil voltages of 0 V (solid line), 2 V (dashed line), 3.5 V (dashed line), and 5 V (dashdot line). Positioning coil voltage is 6 V for all cases. The percentage deformation for each case appears in Table 4.2.

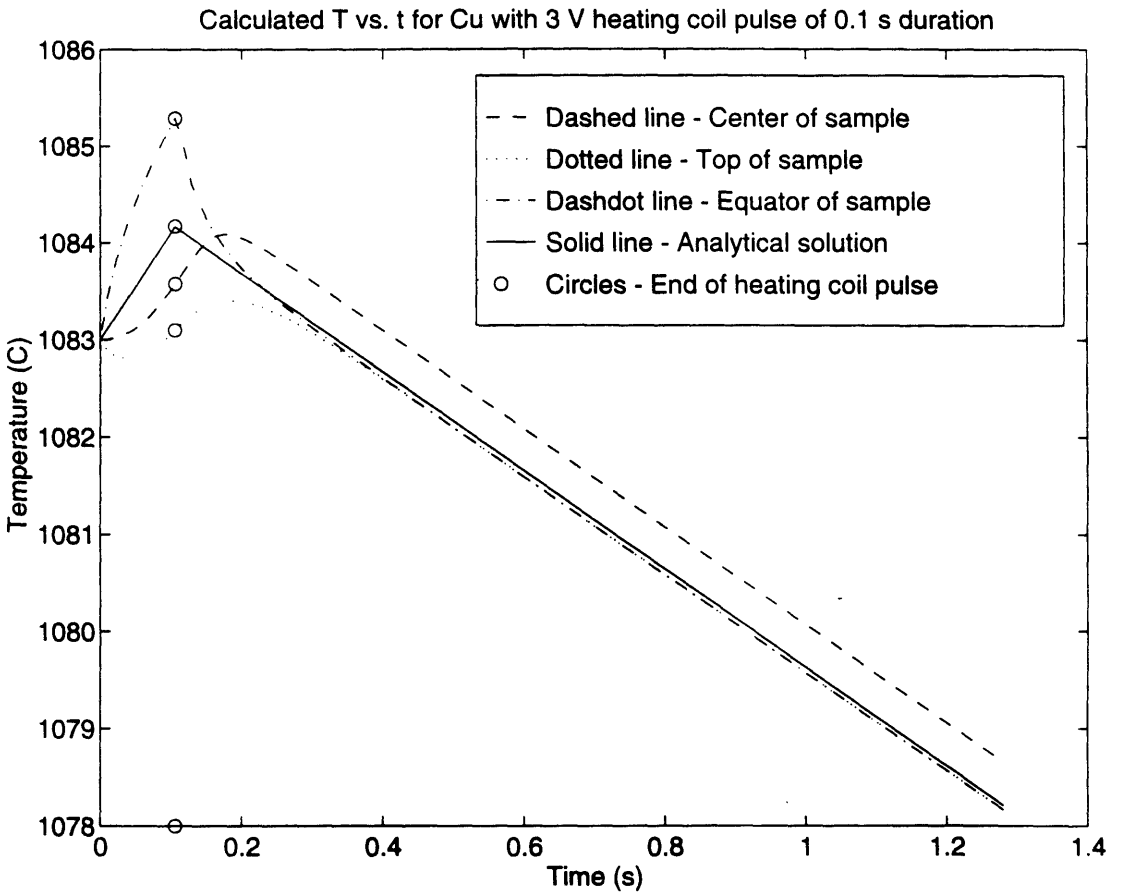

Figure 4.7 Calculated temperature vs. time profiles at center, top, and equator of 10 mm diameter Cu sample during and after 3 V heating coil pulse of 0.1 s duration in TEMPUS. Analytical results provided for comparison. Maximum temperature difference calculated is 2.19°C.

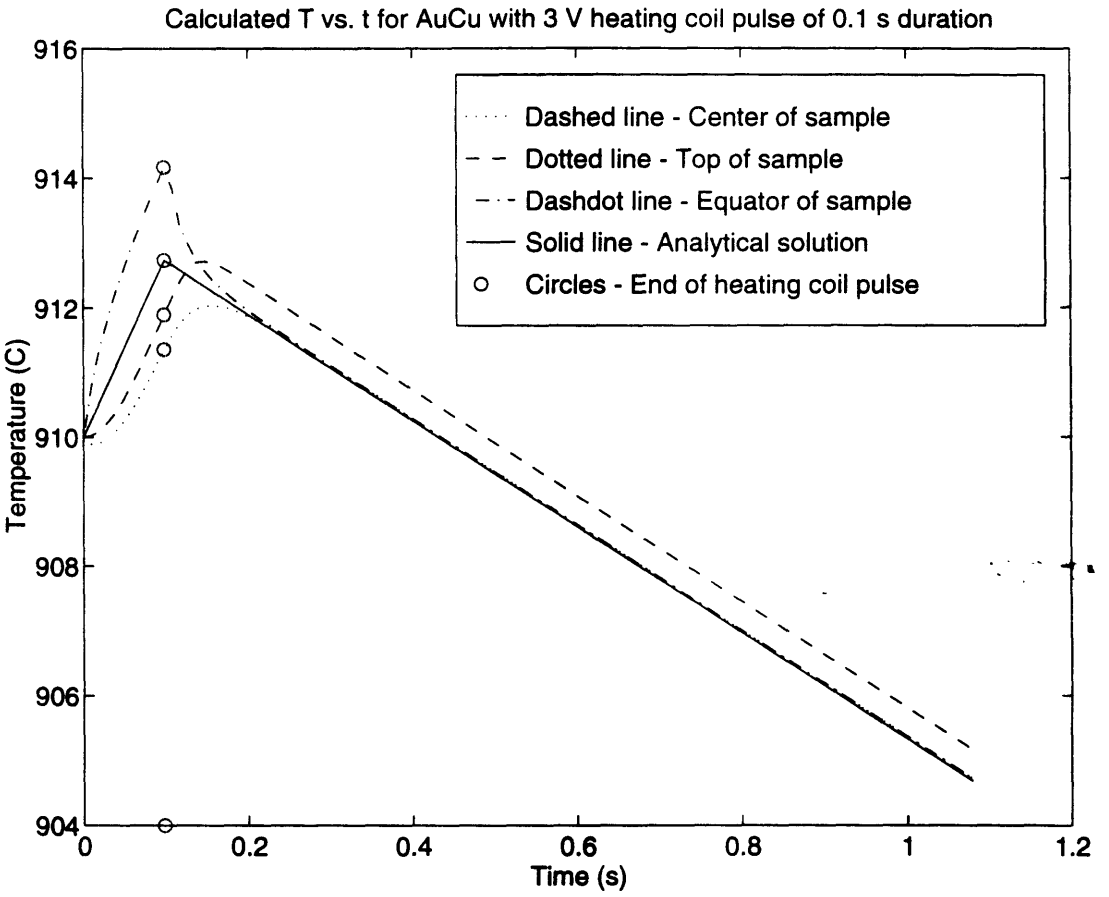

Figure 4.8 Calculated temperature vs. time profiles at center, top, and equator of 8 mm diameter $Au_{56}Cu_{44}$ sample during and after 3 V heating coil pulse of 0.1 s duration in TEMPUS. Analytical results provided for comparison. Maximum temperature difference calculated is 2.81°C.

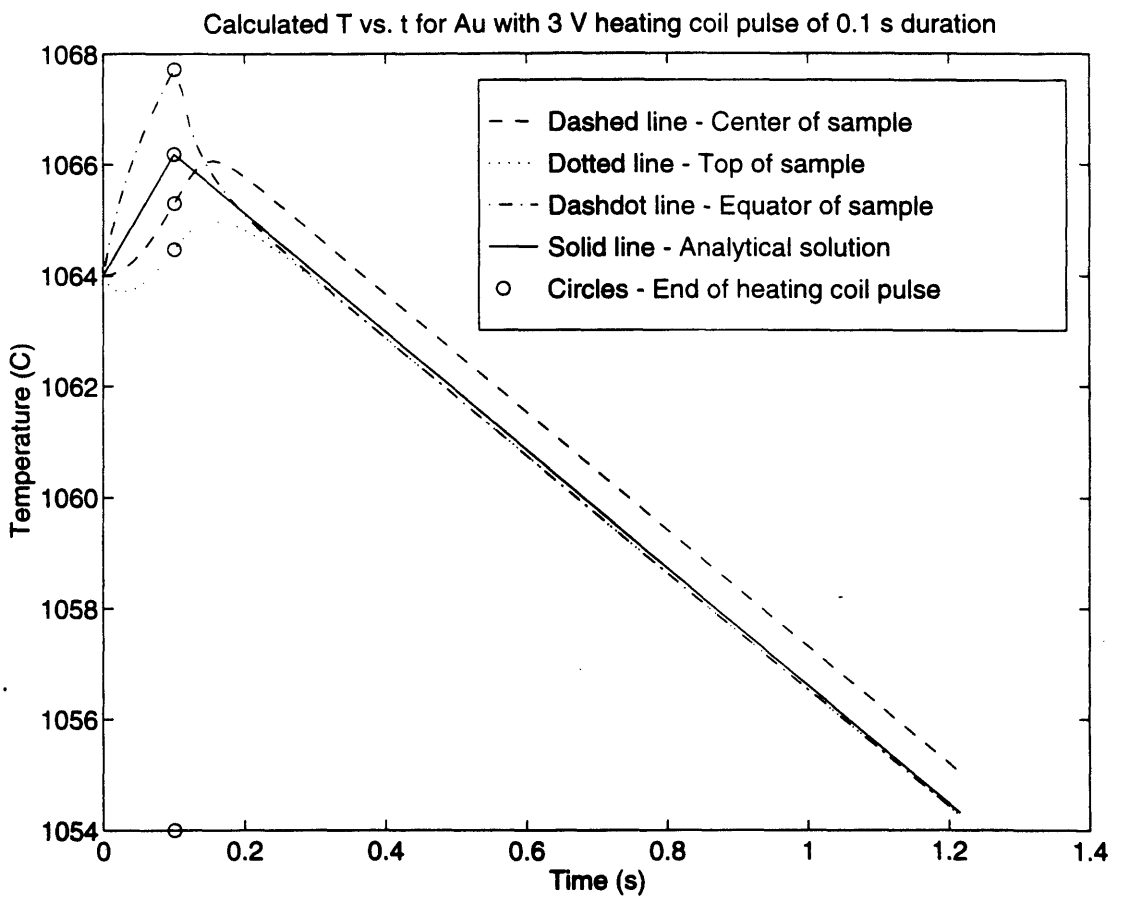

Figure 4.9 Calculated temperature vs. time profiles at center, top, and equator of 8 mm diameter Au sample during and after 3 V heating coil pulse of 0.1 s duration in TEMPUS. Analytical results provided for comparison. Maximum temperature difference calculated is 3.25°C.

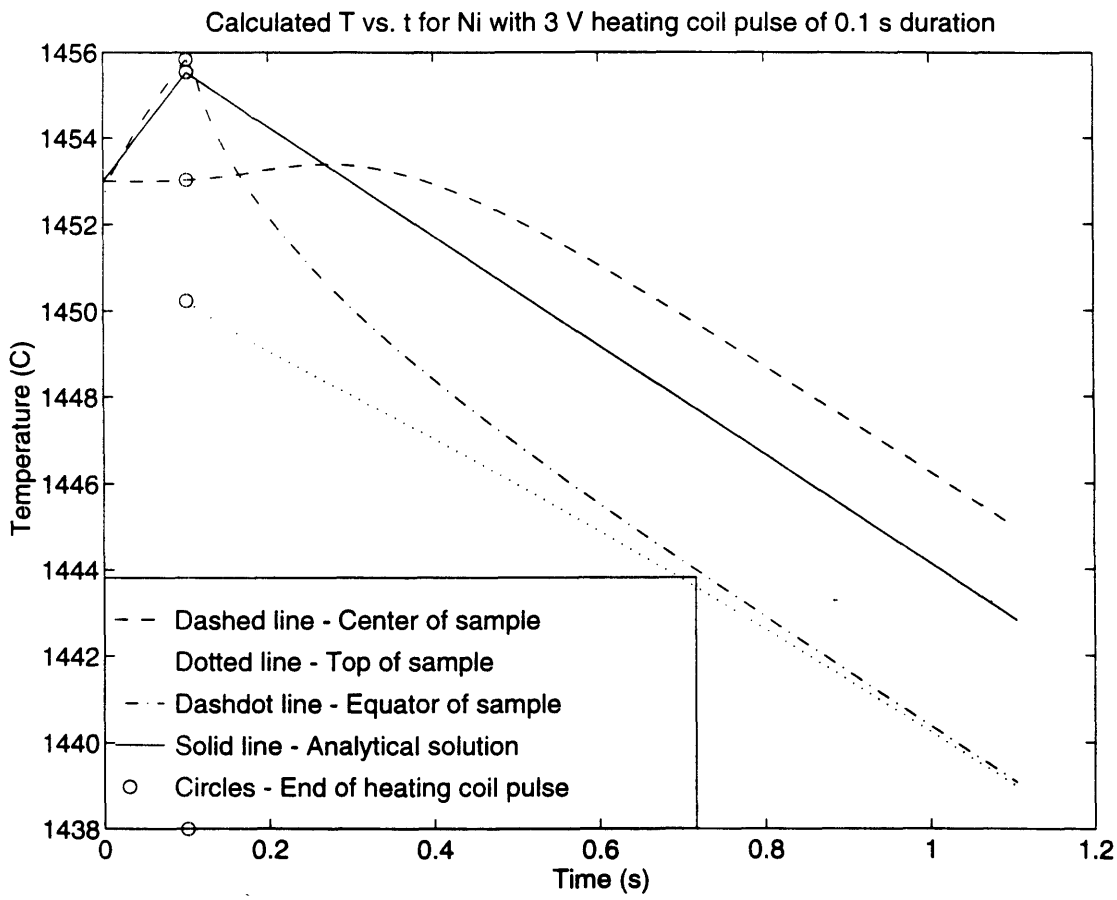

Figure 4.10 Calculated temperature vs. time profiles at center, top, and equator of 10 mm diameter Ni sample during and after 3 V heating coil pulse of 0.1 s duration in TEMPUS. Analytical results provided for comparison. Maximum temperature difference calculated is 5.59°C.

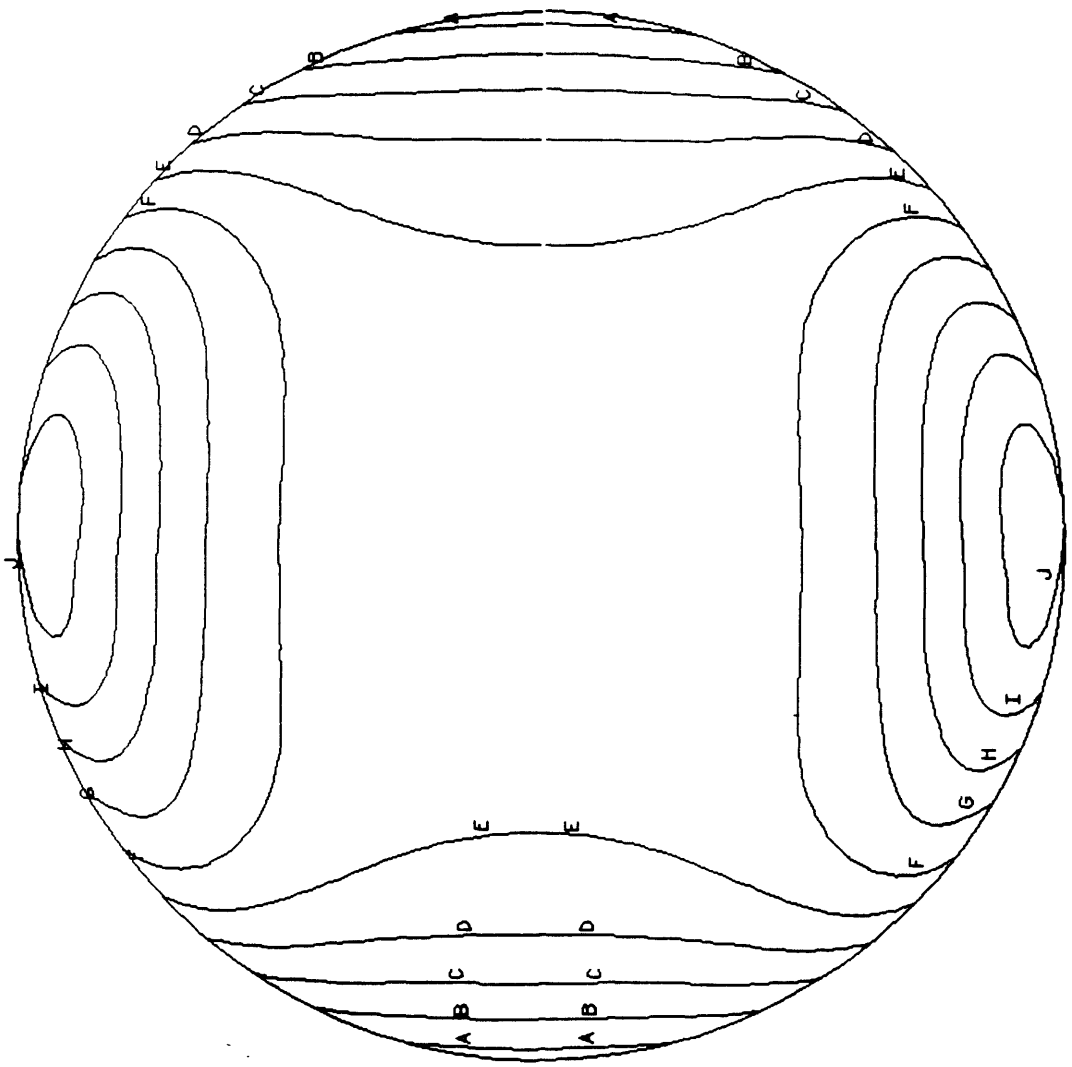

Figure 4.11 Calculated isotherms in 10 mm Ni sample at end of 3 V heating coil pulse of 0.1 s duration in TEMPUS. Maximum temperature is at equator (isotherm J) and minimum temperature is at top and bottom (isotherm A).

Table 4.1 Material properties used in calculations

Properties @ T_m	Cu	$Au_{56}Cu_{44}$	Au	Ni
Melting temp. (°C)	1083	910	1064	1453
Surface tension (N/m)	1.285	1.125	1.140	1.778
Electrical cond. $(\Omega m)^{-1}$	$5x10^6$	$4x10^6$	$3.2x10^6$	$1.18x10^6$
Density (kg/m^3)	7860	15500	17300	7800
Sample radius (m)	0.005	0.004	0.004	0.005

Table 4.2 Calculated equilibrium free surface shapes

Percentage deformation	Cu	$Au_{56}Cu_{44}$	Au	Ni
Heater voltage = 0 V	-0.72%	-0.20%	-0.18%	-0.27%
Heater voltage = 2 V	+3.71%	+3.48%	+3.34%	+2.30%
Heater voltage = 3.5 V	+11.32%	+9.84%	+9.45%	+7.05%
Heater voltage = 5 V	+21.18%	+18.19%	+17.50%	+13.58%
Skin depth/radius X 100%	7.23%	10.10%	11.29%	14.88%

CHAPTER 5

THE SHAPE OF LIQUID METAL DROPLETS IN ELECTROMAGNETIC LEVITATION EXPERIMENTS CONSIDERING INTERNAL FLUID FLOW

ABSTRACT

We present the results and an analysis of calculations of the shape of liquid metal droplets in electromagnetic levitation experiments. Previously a mathematical model was developed to predict the behavior of liquid metal droplets in containerless experiments to determine the surface tension of liquid metals and microgravity experiments on the IML-2 mission to measure the viscosity and surface tension of undercooled metals. In the new mathematical model presented here we consider the electromagnetic forces distributed throughout the droplet as body forces in the Navier-Stokes equations which govern fluid flow rather than as a magnetic pressure acting on the surface of the droplet, as is done in the case of the normal stress balance model of the droplet shape. The computational results of the mathematical model are compared with the actual measured shapes of droplets levitated in ground-based experiments, as well as with the computational results previously obtained using the normal stress balance model. The results of the two models are compared and cases for which the normal stress balance model is sufficient are identified.

5.1 INTRODUCTION

The purpose of this work is to provide mathematical modeling support for the Spacelab IML-2 mission aimed at the experimental determination of the viscosity and surface tension of undercooled metals. A key component of this work is the prediction of the shape of liquid metal droplets in electromagnetic levitation experiments. A model of the shape of an axisymmetric droplet of given volume and material properties subject to induction coils of arbitrary coil geometry, frequency and current was developed in order to determine the peak current that would effect the desired equilibrium shape. The development of a mathematical model for the shape of liquid metal droplets in electromagnetic levitation experiments also makes it possible to achieve correct interpretation of the experimental results and precise measurement of thermophysical properties.

Papers on this topic were presented at the the 1992 and 1993 TMS Annual Meetings [1-2]. These two papers used the normal stress balance model to calculate the equilibrium free surface shape of liquid metal droplets in electromagnetic levitation experiments. In the normal stress balance model we consider only the surface of the droplet and neglects the interior, thereby requiring the assumption that the internal fluid flow is either inviscid (μ=0) or non-existent ($\vec{u} = \vec{0}$). The ideal case for this model would then involve a droplet of infinite conductivity (zero skin depth), in which electromagnetic forces would not be able to penetrate the droplet and drive fluid flow.

The results of the previously-presented calculations on the shapes of molten copper and nickel droplets using the normal stress balance model [2] agreed quite well with the experimentally-determined equilibrium shapes. In both cases the calculations correctly depicted the teardrop shape produced by the conical coil arrangement, but underestimated the extent of deformation from a spherical shape. A consideration of the skin depth-to-droplet radius ratios for the two cases suggested the result that shapes calculated using the normal stress balance model match the experimental shape better in the case of copper than in the case of nickel.

The model presented in this paper constitutes a substantial extension of the previous work by considering the electromagnetically-driven flow within the droplet. This is accomplished by solving the Navier-Stokes equations subject to electromagnetic body forces and a free surface boundary condition.

Fukumoto et al. [3] used an analogous approach to predict the meniscus shape in an electromagnetic caster. It was found that the results of simulations in which flow was considered and in those which flow was neglected were similar in the cases of currents applied at high frequencies. It is well known that at higher frequencies, the skin depth is reduced, indicating that the electromagnetic forces driving the flow would be active over a more limited region.

5.2 FORMULATION AND COMPUTATIONAL METHODOLOGY

There are two major computational tasks associated with modeling the equilibrium shape of an electromagnetically-levitated molten metal droplet through solution of the Navier-Stokes equations with an electromagnetic force source term and a free surface boundary condition. The distribution of electromagnetic (Lorentz) forces, which effects deformation of the free surface (magnetic pressure component) and internal fluid flow (stirring component) in the droplet, must first be calculated. This distribution of electromagnetic forces is then used as the body force in the numerical solution of the transient Navier-Stokes equations. The equilibrium free surface shape of the droplet is then determined from an analysis of the results of the transient calculations.

(i) Electromagnetic calculations

The distribution of induced current density (vector field $\vec{J}$) in the levitated droplet is calculated using the method of mutual inductances presented by, among others, El-Kaddah and Szekely [4], Zong et al. [5], and Dantzig and Midson [6]. The refinements made for the work presented in this paper are detailed in [2]. The axisymmetric droplet is discretized into a set of annular electrical circuits under the implicit assumption that the induced electric current is constant over the approximately rectangular cross-section of each circuit. The distribution of magnetic flux density (vector field $\vec{B}$) in the droplet is then calculated from the induced current density distribution and the applied currents through the induction coils using the Biot-Savart Law. The distribution of electromagnetic (Lorentz) force is given by

$$\vec{F}_{EM} = \vec{J} \times \vec{B} \tag{5.1}$$

and is calculated from the distributions of induced current density and magnetic flux density.

The discretization of the droplet domain for the calculation of the electromagnetic phenomena uses an exponential distribution of grid points in order to better represent the exponential decay from the value at the

surface with normal distance into the droplet (skin effect). The mutual inductances are calculated using Lyle's method of equivalent filaments [7-8] to account for the rectangular cross section of the annular elemental circuits. The method was further adapted to account for the fact that the sides of the elements were usually not oriented parallel and perpendicular to the axis of symmetry.

(ii) Free surface shape calculations

The governing equations for the calculation of the equilibrium free surface shape are the transient Navier-Stokes equations, which assume an incompressible Newtonian fluid (constant density and viscosity). Because the internal fluid flow in liquid metal droplets levitated in ground-based experiments is turbulent due to the strong electromagnetic forces required for levitation [4], an effective viscosity is used. The use of such a "zero-equation" model is by no means exact, but is thought to be a useful first step given the lack of a turbulence model (including two-equation models such as the k-ε model) that accurately models turbulent flow in a system with both recirculating flow and a free surface. Given the use of an effective viscosity which is uniform throughout the volume of the fluid, the Navier-Stokes equations, expressed as a single vector equation are given by:

$$\rho\frac{\partial\vec{u}}{\partial t}+\rho\vec{u}\cdot\vec{\nabla}\vec{u}=-\vec{\nabla}p+\mu_{eff}\nabla^2\vec{u}+\rho\vec{g}+\vec{F}_{EM} \tag{5.2}$$

where $\vec{u}$ is the velocity vector field, which represents the internal fluid flow in the droplet, p is the pressure scalar field, $\vec{g}$ is the gravitational acceleration vector, ρ is the density of the fluid, and μ_{eff} is the effective viscosity of the fluid. The effective viscosity is equal to the sum of the laminar (or molecular) viscosity μ and a turbulent viscosity μ_t.

The Navier-Stokes equations are solved subject to the equation of continuity and a stress continuity free surface boundary condition. For an incompressible fluid, the equation of continuity, a statement of mass conservation, is given by

$$\vec{\nabla} \cdot \vec{u} = 0 \tag{5.3}$$

For axisymmetric geometries, the free surface boundary condition is a balance of components of stress normal to the free surface [9]:

$$p - p_a = \gamma\left(\frac{1}{R_1} + \frac{1}{R_2}\right) + 2\mu_{eff}\frac{\partial u_n}{\partial n} \tag{5.4}$$

where the difference between the fluid pressure and the atmospheric pressure p_a is equal to the sum of the pressure due to surface tension and the normal component of viscous stress at the free surface. In the pressure due to surface tension, the first term on the right-hand side of the equation, γ is the surface tension of the fluid, and R_1 and R_2 are the principal radii of curvature, defined as positive for the outward-bulging surface [10]. In the last term of the Equation 5.4, n represents the curvilinear coordinate normal to the surface. In static fluids, the Equation 5.4 reduces to Laplace's formula.

Comparison of the form of the free surface boundary condition in Equation 5.4 with that in Equation 3.2 illustrates the principal differences between this model and the normal stress balance model, which was presented in Chapter 3. The normal component of the jump in Maxwell stress tensor T_{nn} across the interface, which is equal to the magnetic pressure p_m, appears in Equation 3.2 because the assumption of infinite sample conductivity requires zero magnetic field inside the droplet, thus a surface current density and a jump in the Maxwell stress tensor at the interface. Because finite sample conductivity and electromagnetic body forces are considered in this model, the magnetic field is continuous across the interface so that there is no surface current and the Maxwell stress tensor is also continuous across the free surface. As a result, the Maxwell stress tensor (magnetic pressure) does not appear in Equation 5.4. The normal component of the viscous stress which appears in Equation 5.4 had been neglected in Equation 3.2 based on the assumption of either inviscid or non-existent fluid flow.

The initial condition for each time step is the flow field, pressure field, and free surface shape calculated for the previous time step. The initial condition

used for the first time step of the entire solution process is a spherical shape with no internal fluid flow and a compatible pressure field.

It is customary to recast the differential equations in a dimensionless form. Non-dimensionalized variables, indicated below by an asterisk, are obtained by dividing each variable by an appropriate reference quantity having the correct units. The reference length R is the radius of a spherical droplet of equal volume and the reference velocity is U. The reference quantities for time, pressure, and force are derived from the reference length and reference velocity. The gravitational acceleration vector is non-dimensionalized by dividing by the magnitude of gravitational acceleration g_o.

The dimensionless Navier-Stokes vector equation takes the form

$$\frac{\partial \vec{u}^*}{\partial t^*} + \vec{u}^* \cdot \vec{\nabla}^* \vec{u}^* = -\vec{\nabla}^* p^* + \frac{1}{\mathrm{Re}} \nabla^{*2} \vec{u}^* + \frac{1}{Fr} \vec{g}^* + \vec{F}^* \tag{5.5}$$

where the Reynolds number is defined as

$$\mathrm{Re} = \frac{\rho R U}{\mu_{eff}} \tag{5.6}$$

and the Froude number is defined as

$$Fr = \frac{U^2}{g_o R} \tag{5.7}$$

The dimensionless free surface boundary condition takes the form

$$p^* - p_a^* = \frac{1}{We}\left(\frac{1}{R_1^*} + \frac{1}{R_2^*}\right) + 2\frac{1}{\mathrm{Re}}\frac{\partial u_n^*}{\partial n^*} \tag{5.8}$$

where the Weber number is defined as

$$We = \frac{\rho U^2 R}{\gamma} \tag{5.9}$$

In addition to facilitating computation, the dimensionless forms of the equations provide useful physical insight. The dimensionless groups of system and material parameters present in the dimensionless forms of the governing equations indicate the relative importance of the key phenomena present. The Reynolds number Re represents the ratio of inertial forces to viscous forces, thereby characterizing the nature of the fluid flow within the droplet. The Froude number Fr represents the ratio of inertial forces to gravitational forces and indicates the degree to which gravity influences the fluid flow. The Weber number We represents the ratio of inertial forces to surface tension and indicates the deformability of the free surface of the liquid droplet.

The equilibrium free surface shape is calculated as follows:

(i) The electromagnetic (Lorentz) force distribution inside the droplet is calculated using the method of mutual inductances and the Biot-Savart Law, as described above, for the initial shape, a sphere.

(ii) The electromagnetic force distribution is then supplied as a source term in the fluid flow equations of fluid flow to FIDAP, a computational fluid dynamics package, which numerically solves the non-dimensionalized Navier-Stokes equations subject to the non-dimensionalized free surface boundary condition for axisymmetric geometries at a given time step. The position of the free surface is treated as a degree of freedom at each node on the free surface. This position degree of freedom is introduced as an unknown in the global system of unknowns for which FIDAP solves. Using a Newton-Raphson iteration method, the position of the node on the free surface and the velocity and pressure field variables at the new nodal position are the solution of the iterative solution technique when convergence is attained. Distortion of the finite elements is prevented by constraining the nodes on the free surface to move along spines, specified lines along which the nodes are allowed to move subject to the forces acting on the free surface. [11]

(iii) The flow field, pressure field, and free surface shape are then used as the initial condition of the following time step.

(iv) The droplet undergoes translational and surface oscillations, the amplitudes of which decay through viscous damping. After a sufficiently long time the oscillations damp out and the steady-state solution (free surface shape, velocity field, and pressure field) could be obtained. However, because the computational time required to reach this solution, particularly in the case of high Reynolds number (low viscosity), is very large, the equilibrium free surface shape is identified through analysis of the velocity field at each time step. The equilibrium free surface shape is identified as the droplet shape for which the velocity field satisfies the kinematic boundary condition of no component of velocity normal to the free surface, i.e., no flow across the free surface.

In the calculation of the electromagnetic phenomena, it is assumed that the internal fluid flow in the droplet does not affect the magnetic field. This assumption is thought to be permissible because of the low value of the magnetic Reynolds number that characterizes the system. The electromagnetic forces throughout the droplet in each time step are interpolated from the distribution calculated for a spherical shape because of the considerable computational time that would be required to re-calculate it at each time step. Once some deformation from the original spherical shape used in the calculations is obtained, the distribution of forces for the experimental droplet shape is used. The forces used in each time step are then interpolated until the equilibrium free surface shape is identified. This approach is thought to be acceptable because the extent of deformation that the droplet experiences is sufficiently small, approximately 10% deviation from a spherical shape.

5.3 COMPUTED RESULTS

The experiment was performed on a pure nickel droplet (Johnson Matthey, 99.99%) with mass of approximately 1 g at the German Aerospace Research Establishment in Cologne, Germany. A sketch of the conical coil arrangement, as well as the magnitude of the external magnetic field and magnetic field gradient along the symmetry axis of the coils for a peak applied current of 405 A, as was used in the levitation of the nickel droplet, is shown

in Figure 5.1. The input parameters for the calculations, listed in Table 5.1, correspond to the experimental conditions.

The equilibrium free surface shape of the liquid nickel droplet was calculated using Reynolds numbers of 1, 10, and 25 in order to investigate the influence of the effective viscosity on the calculated shape. The streamline pattern (left side), which illustrates the path of fluid particles within the droplet, and velocity vector field (right side) for the droplet shapes calculated for Reynolds numbers 1, 10, and 25 are shown in Figures 5.2, 5.3, and 5.4, respectively. In each case the calculated shape correctly depicts the teardrop shape produced by the conical coil arrangement required to levitate liquid metal droplets under earthbound conditions.

The fluid flow field is characterized by a two-loop circulation pattern, as can be seen in Figures 5.2, 5.3, and 5.4. The flow along the symmetry axis within the upper circulation loop is toward the top of the droplet and the flow along the symmetry axis within the lower circulation loop is toward the bottom of the droplet. The flow pattern illustrates the fact that the steady-state droplet shape represents an equilibrium between the inertial forces (motion of the fluid) acting to deform the droplet and the surface tension forces acting to resist deformation.

As explained above, at equilibrium the droplet shape is such that there is no flow normal to the free surface. This condition is perfectly satisfied in the case depicted in Figure 5.3, but a small component of flow normal to the free surface can be seen in the cases depicted in Figures 5.2 and 5.4. This is a result of the discrete time steps at which the system of equations are solved. The kinematic boundary condition is exactly satisfied at the time for which results are shown in Figure 5.3, while in the cases in Figures 5.2 and 5.4 this condition is satisfied at a time that occurs between consecutive time steps. The droplet shape and internal flow field presented as the equilibrium droplet shape and flow field are those for the time step at which the kinematic boundary condition is most nearly satisfied.

The calculated droplet shapes are compared with the actual droplet shape using the quantity percentage deformation, which is given by

$$\%def. = \frac{\left(z_{top} - z_{bottom}\right) - 2R}{2R} x100\% \tag{5.10}$$

The percentage deformation for the actual shape, the shape calculated using the normal stress balance model, and for the shapes calculated using the new electromagnetically-driven flow model are summarized in Table 5.2. The magnitude of the maximum velocity in each case using the electromagnetically-driven flow model is also listed. A visual comparison of the actual and calculated shapes is provided in Figure 5.5. From Figure 5.5 it can be seen that the shapes calculated with both models agree quite well with the experimentally-determined shape, but it is important to realize that the visual comparison is quite flattering because the deformation of the droplet is relatively small.

5.4 DISCUSSION

In the normal stress balance model, the free surface shape of the droplet was calculated by considering only the surface and neglecting the interior of the droplet. The calculations produced the same teardrop shape as was observed experimentally, but underestimated the extent of deformation. The reason for this was that there is some penetration of electromagnetic forces into the interior of the droplet; the ratio of skin depth-to-droplet radius was nonzero (25.55% in the case of the nickel droplet) and consideration of the droplet surface therefore cannot provide a completely accurate model of the droplet shape.

From the results listed in Table 5.2 it can be seen that the percentage deformation for all shapes calculated using the electromagnetically-driven flow model, including that for the case with Re = 1, was higher than that for the shape calculated using the normal stress balance model. The fact that consideration of the internal fluid flow yields calculated shapes with a greater extent of deformation helps explain previous experimental results. During parabolic flights on a KC-135 airplane intended to test the TEMPUS facility, which is the electromagnetic levitation facility that will be used on the IML-2

mission, an FeNi sample was found to deform to a significantly greater extent than had been expected.

The percentage deformation increased with the value of the Reynolds number used in the calculations, a logical result given that a higher Reynolds number corresponds to stronger inertial forces. A comparison of the percentage deformation for the actual shape with that of the shapes calculated with the EM-driven flow model indicates that calculation of the actual shape using that model requires a Reynolds number between 10 and 25. These Reynolds numbers correspond to ratios of turbulent viscosity to laminar viscosity of 50 and 20, respectively. Given that the actual shape would be obtained by calculation with the EM-driven flow model for a value of the Reynolds number between 10 and 25, the results correspond well with those obtained by El-Kaddah and Szekely for a liquid iron sphere of mass 1 g [4]. Using the k-ε model to calculate the internal turbulent flow, El-Kaddah and Szekely obtained ratios of turbulent viscosity to laminar viscosity ranging between 10 and 40. The values of maximum flow velocity obtained with the EM-driven flow model also compare favorably with the experimental results of Robertson and Jenkins, who observed a maximum velocity of 10-20 cm/s for a system similar to that studied by El-Kaddah and Szekely [12].

The results obtained illustrate the need for considering the interior of the droplet as well as the surface in calculating the droplet shapes in cases where the electromagnetic forces penetrate the droplet to a significant degree. In addition to providing a more accurate model of the droplet shape, the EM-driven flow model provides valuable information about the internal flow which is important to the performance of thermophysical property measurements in microgravity experiments.

The methodology that has been developed for modeling the free surface shape of liquid metal droplets in electromagnetic levitation experiments is readily applicable to industrial systems involving electromagnetic shaping. In order to model the free surface shape of a large pool of molten metal subjected to electromagnetic forces, consideration of the surface is sufficient. In cases where the ratio of skin depth-to-sample dimensions is larger, as in

meniscus control in electromagnetic casting and electromagnetic shape control of liquid metal jets, the interior of the droplet must be considered.

The dependence of the calculated equilibrium droplet shape on the value of the Reynolds number (effective viscosity) used and the lack of an appropriate turbulence model illustrate the need for direct simulation of turbulent flow in order to have an exact model of the droplet shape and internal fluid flow. This need also extends to a host of industrial problems involving turbulent recirculating flows and free surfaces.

5.5 ACKNOWLEDGEMENTS

The authors acknowledge the financial support provided by the National Aeronautic and Space Administration under contract number NAG8-970. The authors acknowledge use of the FIDAP computational fluid dynamics package, property of Fluid Dynamics International, Inc., Evanston, Illinois, and the assistance of the technical support staff. The FIDAP calculations were performed on the MIT Cray X-MP and the authors acknowledge the efforts of the staff of the MIT Supercomputer Facility.

5.6 REFERENCES

[1] E. Schwartz, J. Szekely, O. J. Ilegbusi, J-H. Zong, and I. Egry, "The Computation of the Electromagnetic Force Fields and Transport Phenomena in Levitated Metallic Droplets in the Microgravity Environment", Magnetohydrodynamics in Process Metallurgy, TMS, San Diego, 1992, 81-87.

[2] E. Schwartz, S. Sauerland, J. Szekely, and I. Egry, "On the Shape of Liquid Metal Droplets in Electromagnetic Levitation Experiments", Containerless Processing: Techniques and Applications, TMS, Denver, 1993, 57-64.

[3] H. Fukumoto, Y. Hosokawa, K. Ayata, and M. Morishita, "Numerical Simulation of Meniscus Shape Considering Internal Flow Effects", Magnetohydrodynamics in Process Metallurgy, TMS, San Diego, 1992, 21-26.

[4] N. El-Kaddah and J. Szekely, "The Electromagnetic Force Field, Fluid Flow Field, and Temperature Profiles in Levitated Metal Droplets", Metallurgical Transactions B, 14(1983), 401-410.

[5] J-H. Zong, J. Szekely, and E. Schwartz, "An Improved Computational Technique for Calculating Electromagnetic Forces and Power Absorptions Generated in Spherical and Deformed Body in Levitation Melting Devices", IEEE Transactions on Magnetics, 28(3)(1992), 1833-1842.

[6] J. A. Dantzig and S. P. Midson, "Billet Heating for Semi-Solid Forming", Proceedings of the Second International Conference on the Processing of Semi-Solid Alloys and Composites, TMS, 1992, 105-118.

[7] R. Dudley and P. E. Burke, "The Prediction of Current Distribution in Induction Heating Installations", IEEE Transactions on Industry Applications, IA-8(5)(1972), 565-571.

[8] P. E. Burke, P. P. Biringer, P. F. Ryff, and E. Solger, "The Prediction and Measurement of Current Distribution in Coaxial Circular Geometries", 6th PICA Conference Proceedings (1969), 464-482.

[9] FIDAP Theoretical Manual, Revision 6.0, Fluid Dynamics International, Inc., (1991), 2-19.

[10] L. M. Racz, J. Szekely, and K. A. Brakke, "A General Statement of the Problem and Description of a Proposed Method of Calculation for Some Meniscus Problems in Materials Processing", ISIJ International, 33(2)(1993).

[11] FIPREP Users Manual, Revision 6.0, Fluid Dynamics International, Inc. (1991), 8-2.

[12] D. G. C. Robertson and A. E. Jenkins, "The Reaction of Liquid Iron and Its Alloys in Pure Oxygen", Heterogeneous Kinetics at Elevated Temperatures, Plenum Press, New York (1970), 393-408.

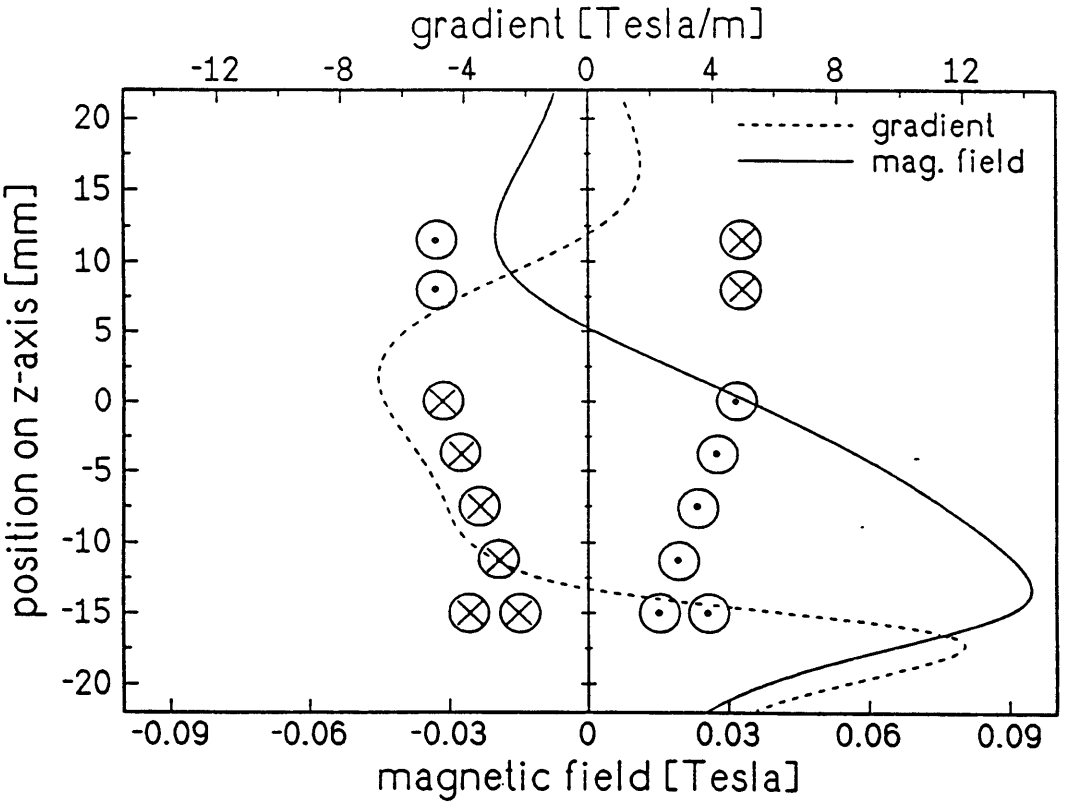

Figure 5.1 Conical coil arrangement with field strength and gradient along symmetry axis for peak applied current of I_0=405 A.

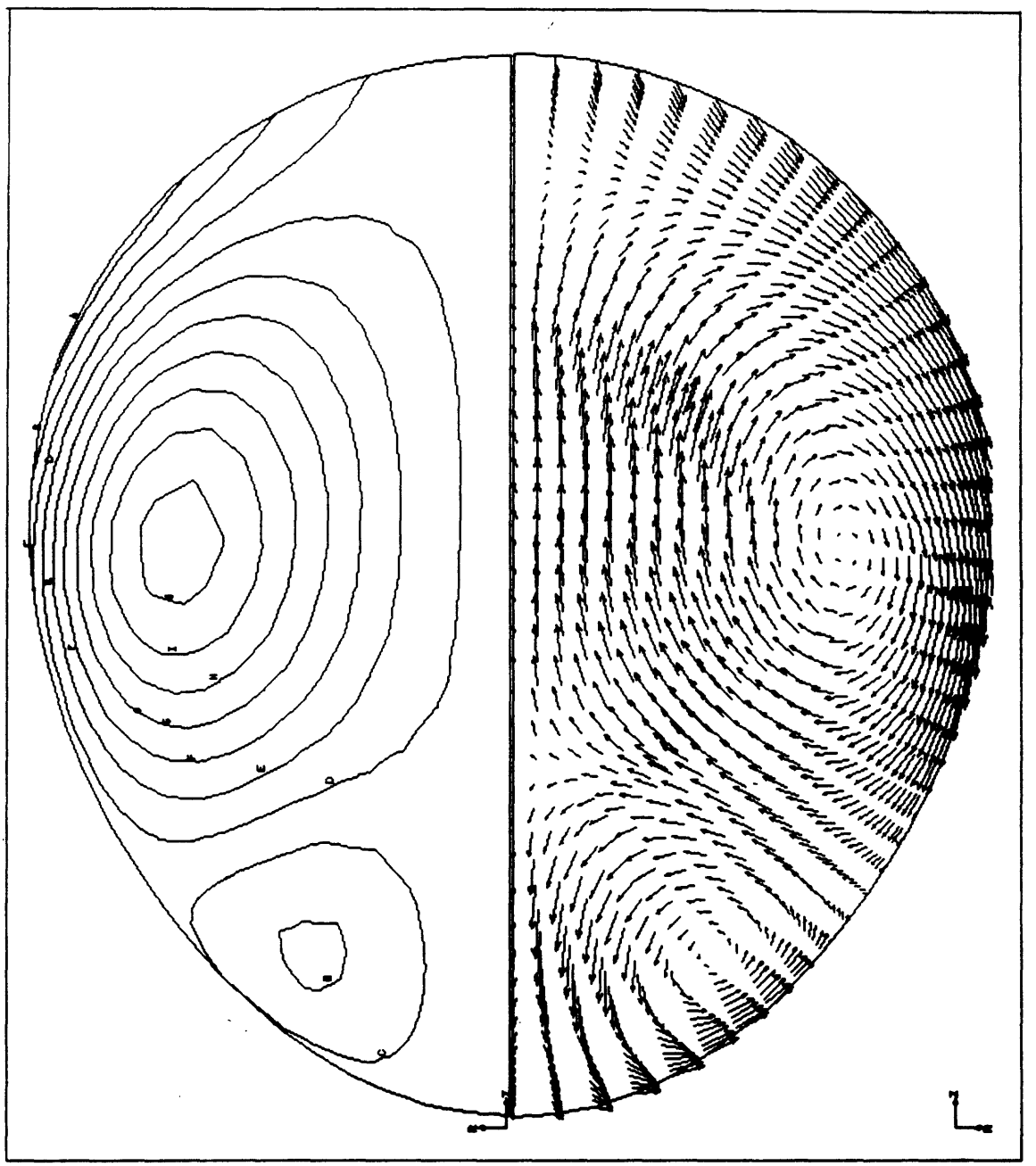

Figure 5.2 Streamline pattern (left side) and velocity vector field (right side) for equilibrium shape of Ni droplet calculated using EM-driven flow model with Re=1. Magnitude of maximum velocity is 1.39 cm/s and extent of deformation is 7.55%.

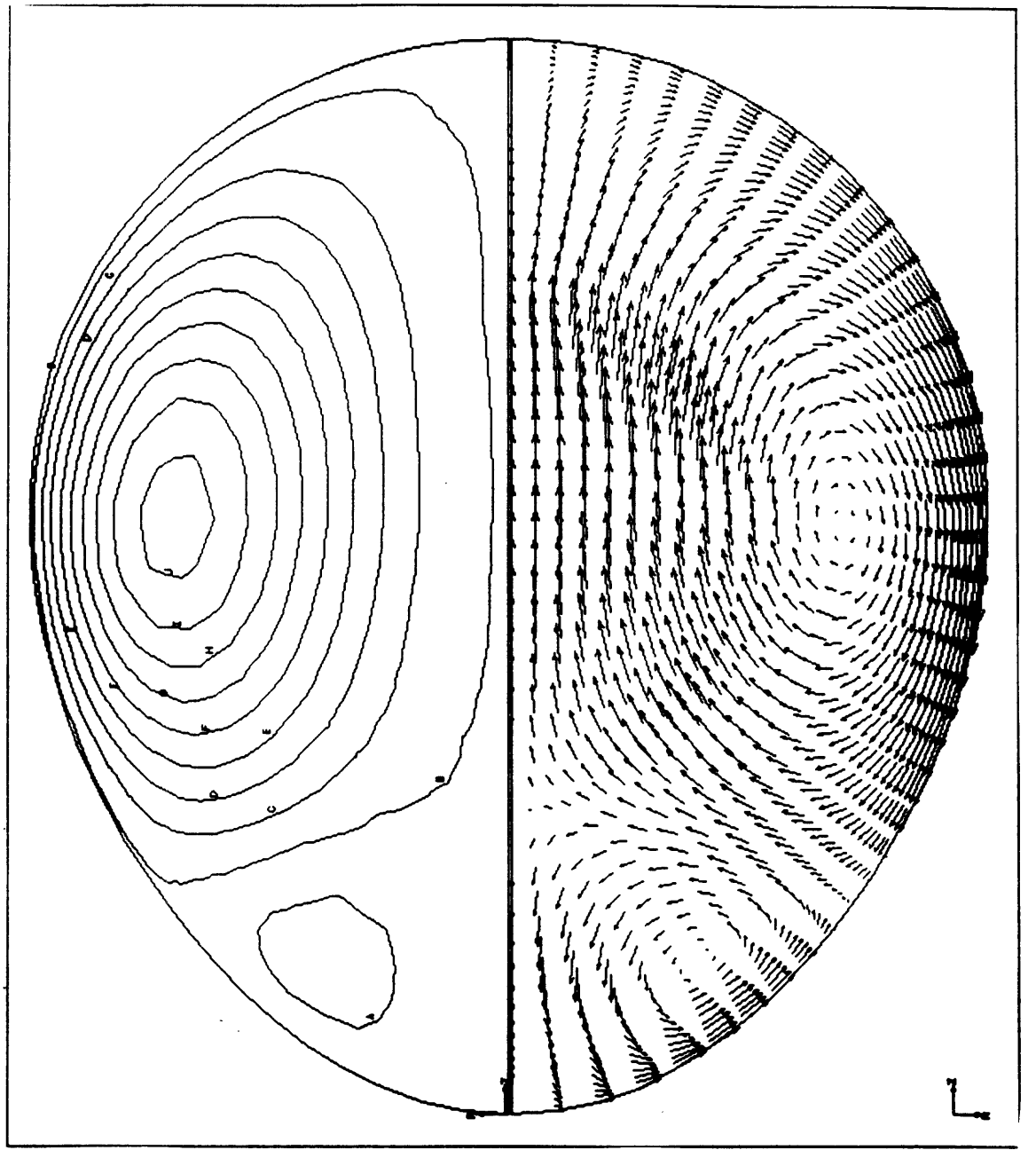

Figure 5.3 Streamline pattern (left side) and velocity vector field (right side) for equilibrium shape of Ni droplet calculated using EM-driven flow model with Re=10. Magnitude of maximum velocity is 14.51 cm/s and extent of deformation is 9.13%.

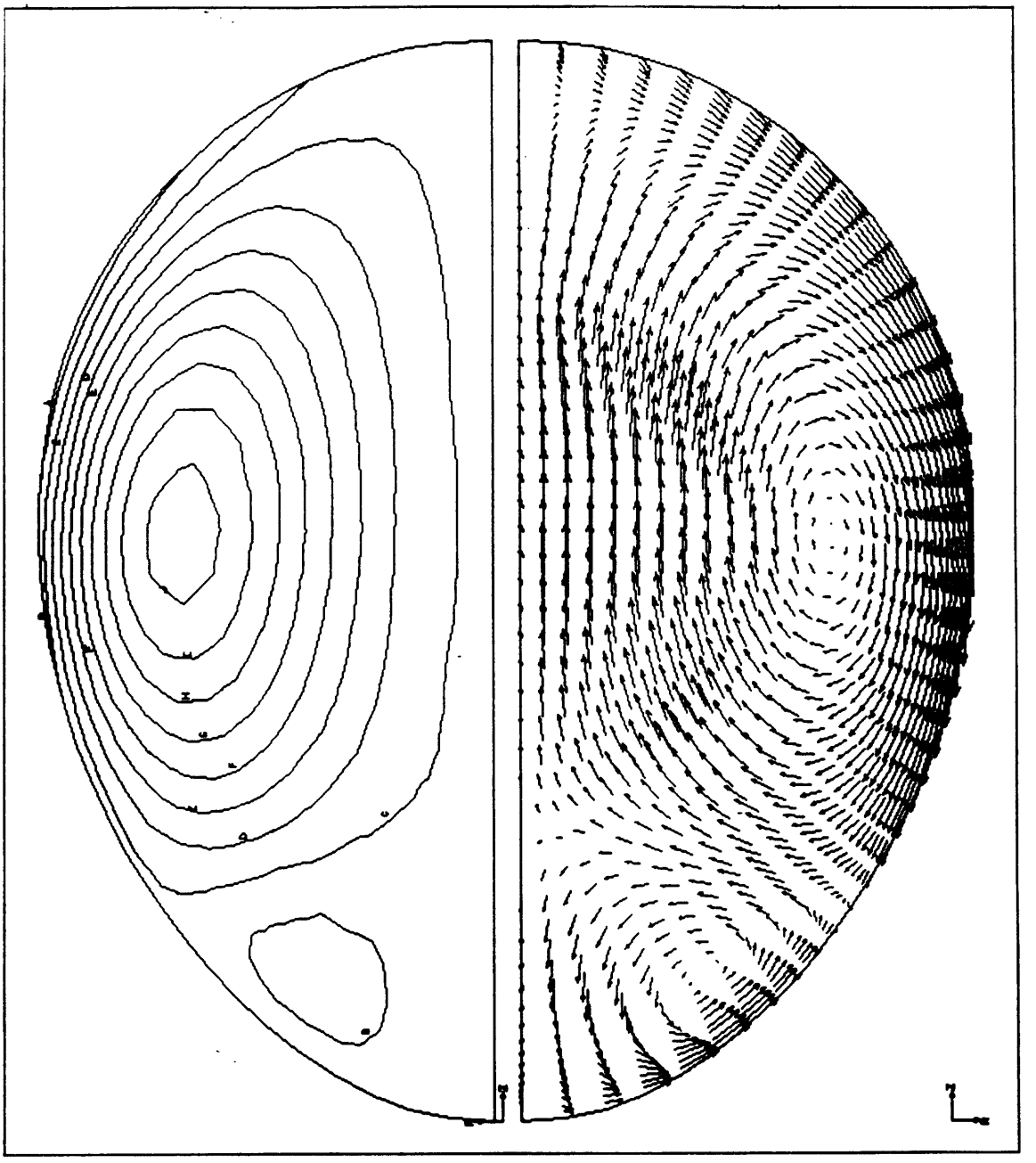

Figure 5.4 Streamline pattern (left side) and velocity vector field (right side) for equilibrium shape of Ni droplet calculated using EM-driven flow model with Re=25. Magnitude of maximum velocity is 25.48 cm/s and extent of deformation is 12.55%.

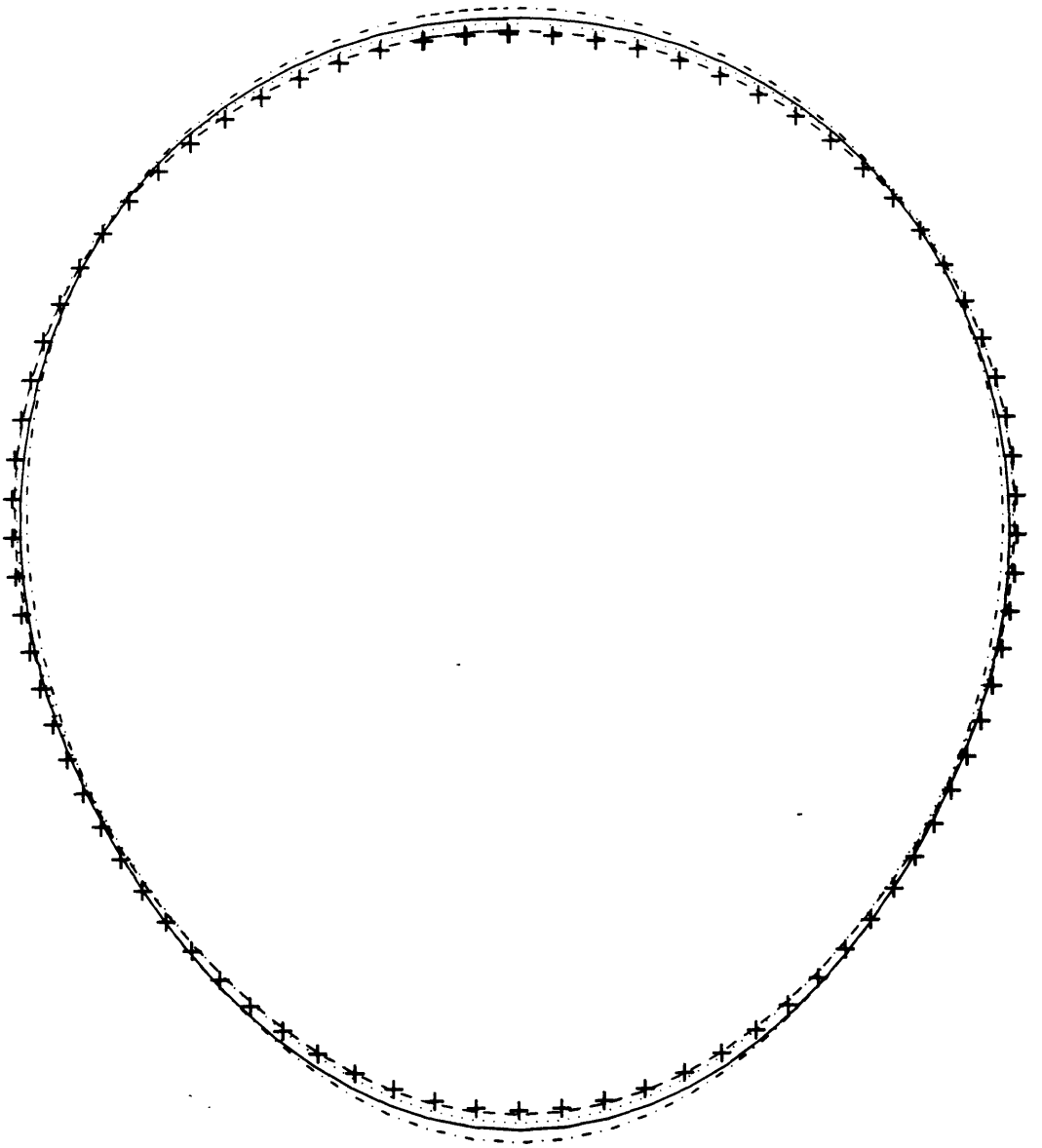

Figure 5.5 Comparison of results for Ni droplet shapes.

—— Experimentally-determined (10.22% def.)

+++ Normal stress balance model (6.84% def.)

----- EM-driven flow model, Re=1 (7.55% def.)

..... EM-driven flow model, Re=10 (9.13% def.)

-.-.- EM-driven flow model, Re=25 (12.55% def.)

Table 5.1 Input parameters for equilibrium free surface shape calculations

Parameter	Ni
Applied current (A)	405
Frequency (kHz)	333
Radius of sphere (mm)	3.11
Elec. cond. $(\Omega m)^{-1}$	1.205×10^6
Density (kg/m^3)	8080
Surface tension (N/m)	1.82

Table 5.2 Percentage deformation and magnitude of maximum velocity for actual and calculated Ni droplet shapes

Case	%def.	U(max)
Experimental	10.22%	N/A
Normal stress balance model	6.84%	N/A
EM-driven flow model (Re=1)	7.55%	1.39 cm/s
EM-driven flow model (Re=10)	9.13%	14.51 cm/s
EM-driven flow model (Re=25)	12.55%	25.48 cm/s

CHAPTER 6

SURFACE TENSION MEASUREMENTS ON LIQUID METALS IN MICROGRAVITY

ABSTRACT

The results of surface tension measurements on liquid metals performed in microgravity aboard the Space Shuttle Columbia are presented. It is shown that there is excellent agreement between the results obtained and with both data obtained from experiments performed on the earth and theoretical predictions. The results show that surface tension measurements made with the oscillating drop technique using electromagnetic levitation are accurate and can be improved by performing the experiments in microgravity. A brief discussion of possible experimental evidence of dynamic nucleation is also presented.

6.1 INTRODUCTION

Interest in the surface tension of liquid metals and alloys stems both from scientific considerations, because understanding these properties is essential to validating theories of the liquid state, and from practical considerations, such as their applications in processing, chemical, and metallurgical industries [1]. The surface tension is critical in casting, molding, crystal growth operations, smelting, and refining, brazing, sintering, zone refining, and fiber formation [2]. The dependence of surface tension on temperature is also important because it leads to Marangoni convection, which is particularly important in such processes as welding and crystal growth [3-4].

With the advent of powerful mathematical modeling techniques for metallurgical phenomena, there is renewed interest in reliable data on the physical properties of liquid metals. Presently, the knowledge and accuracy of these data are the limiting factors in the models [5]. The property database for liquid metals is incomplete and the conventional measurement techniques are not entirely satisfactory.

The electromagnetic levitation technique is a widespread method for containerless processing of liquid metals. A major advantage of the method

is the avoidance of sample contamination through the use of high-purity processing gas and contact-free measuring techniques [3]. The oscillating drop technique involves observation of the oscillations of a levitated droplet about its equilibrium shape. The restoring force for surface oscillations is the surface tension, which can be related to the frequency of the oscillations [6].

There has been some skepticism about the results obtained by the oscillating drop technique because this method tends to yield higher values for the surface tension than those from conventional methods. Although some authors have attributed this to the better purity of the sample's surface, it may also be a systematic error due to the presence of the electromagnetic levitation field, which produces a magnetic pressure at the surface and leads to an apparent increase of the surface tension. Using a correction formula derived by Cummings and Blackburn [7], Egry et al. obtained surface tension values for gold which were independent of sample mass and in agreement with values derived by conventional techniques [8]. This work demonstrated that the oscillating drop technique could produce very accurate results and would be the preferred method for determining the surface tension of reactive metals [9].

Surface tension measurements made with the oscillating drop technique using electromagnetic levitation can be improved by performing the experiments in a microgravity environment. Residual accelerations aboard the Space Shuttle are on the order of one thousand to one hundred thousand times less than the magnitude of gravitational acceleration on the earth, therefore, much weaker electromagnetic fields are necessary. This offers three primary benefits to surface tension measurements.

(1) The sample remains nearly spherical, which greatly facilitates the oscillation analysis.

(2) The magnetic pressure on the surface of the sample is reduced.

(3) The induced heat in the sample is reduced, making processing in ultra-high vacuum and at lower temperatures feasible [10-11].

The experiments were conducted using TEMPUS (Tiegelfreies Elektromagnetisches Prozessieren Unter Schwerelosigkeit), the electromagnetic containerless processing facility. TEMPUS uses

electromagnetic levitation for containerless positioning and heating of metal samples and can be used under microgravity conditions. TEMPUS was built by Dornier, a company based in Friedrichshafen, Germany, under contract from DARA, the German space agency. Team TEMPUS includes representatives from NASA, DARA, Dornier, and eight teams of Principal Investigators from the United States and Germany. The results of the TEMPUS team are presented in [12].

The experiments took place from July 8 to July 23, 1994, aboard the Space Shuttle Columbia as part of the Spacelab IML-2 (Second International Microgravity Laboratory) mission. The experiments were monitored and telecommanded from the Payload Operations Command Center (POCC) at NASA Marshall Space Flight Center in Huntsville, Alabama.

In this paper we present experimental results for Au, Au-44 at%. Cu (gold with 44 atomic per cent copper), and Zr-36 at%. Ni (zirconium with 36 atomic per cent nickel). Wherever possible comparisons are made with prior measurements.

6.2 EXPERIMENTAL

Using the oscillating drop technique, we measured the frequency of oscillations of levitated droplets about their equilibrium shapes. Lord Rayleigh calculated the frequencies of small-amplitude oscillations of an inviscid spherical liquid droplet of mass M due to surface tension γ. The relationship between the frequency of oscillation mode n and the surface tension is given by [13]

$$\nu_n = \sqrt{\frac{1}{3\pi} n(n-1)(n+2)\frac{\gamma}{M}} \tag{6.1}$$

The mode n=2 is the fundamental mode of surface oscillations. For aspherical, rotating droplets, the n=2 mode is shifted and split into five peaks (m = -2, -1, 0, +1, +2) [4]. In an earthbound experiment on a liquid nickel droplet performed by Egry et al. [14], such a frequency shift and splitting was observed. In order to determine the five different frequencies for the n=2

modes, they developed a method of oscillation detection based on inspection of certain geometrical parameters by digital image processing. A frequency sum rule derived by Cummings and Blackburn [7] to obtain the Rayleigh frequency from the split modes was used in order to calculate the surface tension from Equation 6.1.

In microgravity, due to the reduced electromagnetic fields needed to position the samples, it was thought that reduced deformation due to the reduced magnetic pressure and lesser rotation due to weaker electromagnetic forces would eliminate the frequency shift and splitting seen in ground-based experiments. This would offer the benefit of eliminating the need for correction formulae to calculate the Rayleigh frequency.

A schematic sketch of the experimental arrangement for TEMPUS is shown in Figure 6.1. The TEMPUS coils were designed to provide independent control of heating and positioning. By switching off or reduced the voltage in the heating coils, the power input into the sample can be greatly reduced, thereby allowing cooling without forced gas cooling of the sample. A more detailed description of the TEMPUS facility and its subsystems is given in [12].

In the microgravity experiment, the solid sample was introduced from below into the space within the coils. The positioning coils were turned on first, and once the sample rested in a stable position, the heating coils were turned on to melt the sample and bring it to a predetermined, desired temperature above the melting point. The heating coil control voltage was then substantially reduced to allow the sample to cool by radiation and by conduction to the surrounding very-low-pressure Ar gas environment (in the case of the Au and AuCu samples). The sample was then squeezed and deformed by applying a heating coil control voltage of amplitude 2-3 V for 0.1 s. After the heating coil control voltage was reduced again, the oscillations of the droplet were observed and recorded on video for a period of 5 s, during which time the sample continued to cool.

The pulsing and observation procedure was repeated until the droplet solidified in order to make surface tension measurements over a large temperature range. After the droplet solidified, it was reheated, melted,

cooled, squeezed, and observed as described. This procedure was performed for as many experiment cycles (heating and cooling) as possible, or until the sample hit the sample cage, terminating the experiment. In the case of the gold sample, the heating coil pulse was only applied once in each cycle. A profile of temperature, heating coil control voltage, and positioning coil control voltage vs. time for a cycle of the experiment on Zr-36 at.% Ni is shown in Figure 6.2. Note that only one heating coil pulse is visible because the 1 Hz data can only show one of every ten pulses of duration 0.1 s.

The oscillating drop was observed from the side by a video camera and recorded on videotape at a sampling rate of 120 Hz. Because of obstruction from the heating coils in the horizontal direction and the sample cage wires in the vertical direction as shown in Figure 6.3, only a portion of the oscillating sample was visible in each frame. The images were therefore analyzed for the visible area in each frame. Each group of data points was taken from the 5 s period between heating coil pulses. Subsequent Fourier analysis using a 512-point Fast Fourier Transform (FFT) yielded the frequency spectra. Figure 6.4 shows one such spectrum for the gold-copper sample.

It can be seen from the figure that in the microgravity experiments the splitting of the n=2 mode that is seen in earthbound experiments did not occur. The Rayleigh frequency ν_R in each case was therefore taken to be the frequency corresponding to the highest peak in the frequency spectrum. From Equation 6.1, the surface tension value could then be calculated from the Rayleigh frequency using the equation

$$\gamma = \frac{3}{8}\pi M \nu_R^2 \tag{6.2}$$

Using the method described above, we measured the surface tension of liquid pure gold, the alloy Au-44 at.% Cu, and the eutectic alloy Zr-36 at%. Ni. Temperature measurement was performed from the top view of the sample using a two-color broadband pyrometer which was equipped with an InAs detector and had a sampling rate of 100 Hz.

6.3 RESULTS

6.3.1 Gold

We measured the surface tension of liquid gold of mass 5.21 g in the temperature range 1225-1330°C, which corresponds to temperatures 160-265°C above the melting point. The oscillation amplitudes of the surface immediately after the heating coil pulses were less than 10%, which means that application of the linearized theory and use of Equation 6.1 is justified. The data obtained were fitted to the linear relation

$$\gamma(T) = \gamma(T_m) + (d\gamma / dT)(T - T_m) \tag{6.3}$$

and are shown in Figure 6.5. The linear fit of the measured surface tension of liquid gold as a function of the Celsius temperature T, also shown in the figure, is

$$\gamma_{Au}(T) = 1.149 - 0.14 \cdot 10^{-3}(T - 1064) N / m \tag{6.4}$$

The filled points on the plot are data points obtained from the microgravity experiments. The different symbols represent different experiment cycles. For comparison, data obtained by Sauerland et al. [8] in earthbound levitation experiments on a gold sample of mass 0.72 g are given. The "1 g-results" indicate uncorrected surface tension values, and the "1 g-results extrapolated to 0 g" indicate the surface tension values obtained using the correction formula of Cummings and Blackburn [7].

6.3.2 Au-44 at.% Cu alloy

The surface tension of liquid $Au_{56}Cu_{44}$ was measured in the temperature range 970-1080°C using a sample of mass 4.2066 g. The oscillation amplitudes immediately after the heating coil pulses were less than 10%. Figure 6.6 shows the large number of data points and a regression line corresponding to Equation 6.3. The temperature dependence of $Au_{56}Cu_{44}$ is given by

$$\gamma_{AuCu}(T) = 1.196 - 0.02 \cdot 10^{-3}(T - 910) N / m \tag{6.5}$$

6.3.3 Zr-36 at.% Ni alloy

The surface tension of liquid $Zr_{64}Ni_{36}$ was measured in the temperature range 980-1150°C, which corresponds to undercooling of ΔT=30°C and heating 140°C above the melting point, using a sample of mass 1.9366 g. The oscillation amplitudes immediately after the heating coil pulses were less than 10%. Figure 6.7 shows the data points and a regression line corresponding to Equation 6.3. The temperature dependence of $Zr_{64}Ni_{36}$, assuming that the surface tension of the undercooled liquid follows the same linear dependence on temperature as the superheated liquid, is given by

$$\gamma_{ZrNi}(T) = 1.545 + 0.08 \cdot 10^{-3}(T - 1010) N/m \tag{6.6}$$

6.4 DISCUSSION

6.4.1 Results on gold

The linear fit of the data obtained by Sauerland et al. is

$$\gamma(T) = 1.121 - 0.09 \cdot 10^{-3}(T - 1064) N/m \tag{6.7}$$

Figure 6.5 and a comparison of the relations in Equations 6.4 and 6.7 shows that our values agree very well with the "1 g-results extrapolated to 0 g" obtained by Sauerland et al. in earthbound experiments. The value of surface tension at the melting point of 1.149 N/m obtained in this study compares remarkably well with the mean value for the surface tension of liquid gold published by Keene in his review article [15], 1.145 N/m. The value of $d\gamma/dT$=-0.14x10^{-3} N/mK obtained from a linear fit of the data obtained in this study is closer to the mean value of $d\gamma/dT$ given in [15] of -0.20x10^{-3} N/mK. It should be noted that the temperature dependence of the surface tension of liquid gold is relatively weak, which can partially account for the difference in the temperature coefficient.

The resolution in the frequency spectrum obtained from the FFT of the data on visible area determines the experimental error. By taking the differential of Equation 6.2, it can be seen that the error in the value of the surface tension

$\Delta\gamma$ from the error in the Rayleigh frequency $\Delta\nu_R$ is given by

$$\Delta\gamma = 2\gamma\frac{\Delta\nu_R}{\nu_R} \tag{6.8}$$

The error in surface tension, indicated in Figure 6.5 by the error bars on the points corresponding to the data obtained in the microgravity experiments, is less than 3% of the surface tension value. There is also a finite error resulting from the fact that the sample continues to cool during the time that the sample is oscillating, the data sampling period. However, because of the weak temperature dependence of the surface tension, this error is less than 1% of the surface tension value. The experimental error is approximately the same for all three materials considered here.

6.4.2 Results on Au-44 at.% Cu

As can be seen in Figure 6.6, the addition of Cu to Au increases the surface tension slightly, but the temperature dependence of the surface tension is even weaker than it is for pure gold. Au-Cu is a congruent-melting alloy, a system in which the liquidus and solidus lines go through a minimum. The composition $Au_{56}Cu_{44}$ is the composition at which this minimum occurs, which means that it behaves just like a pure metal; solidification begins and ends at a constant temperature of 910°C with no change in composition [16]. Because it behaves like a pure metal, the temperature dependence of liquid $Au_{56}Cu_{44}$ was modeled using an ideal solution model developed by Gorges et al. [17]. The relation predicted by the ideal solution model for the temperature of liquid alloys is given by

$$\gamma_{Ideal}(T) = 1.193 - 0.11\cdot 10^{-3}(T - 910)N/m \tag{6.9}$$

The agreement in the surface tension at the melting point determined experimentally and calculated with the model is remarkably good. The temperature coefficients are somewhat different, but both suggest that the temperature dependence of the surface tension of liquid gold-copper is very weak.

The experimental data of Gallois and Lupis [18] for the surface tension of liquid gold-copper alloys at 1108°C suggest a value of approximately 1.12 N/m at that temperature. The value of 1.192 N/m obtained from the linear fit of our experimental data at that temperature compares well with the value obtained by Gallois and Lupis.

6.4.3 Results on Zr-36 at.% Ni

There are no data available on the surface tension of the liquid of this eutectic alloy. The increase of the surface tension of liquid $Zr_{64}Ni_{36}$ with increasing temperature suggested by the linear fit of the data points must be confirmed, but the temperature dependence is not very strong. Surface analysis of IML-2 samples of pure zirconium processed in TEMPUS indicated that oxygen, which is surface-active, was present. If this was also true for the $Zr_{64}Ni_{36}$ sample, which has not yet been analyzed, this could explain the increase in surface tension with temperature. It is even possible, given the error bars on the data points, that the temperature coefficient of the surface tension is negative, as it is for Au and $Au_{56}Cu_{44}$.

It should be mentioned that one of the problems faced during the TEMPUS microgravity experiments was significant sample contamination [12]. However, this problem is thought to not have a large influence on the surface tension results for gold because of its insensitivity to impurities. Gold is surface active in copper [18], therefore, the impurities should also not significantly affect the surface tension results for gold-copper. The solubility of oxygen in zirconium is high, therefore, impurities may not have affected the quality of the surface of the zirconium-nickel sample. The surface of the sample must be analyzed in order to determine this.

6.5 CONCLUSIONS

We have successfully performed measurements of the surface tension of the melts of a pure metal, a congruent-melting alloy, and a eutectic alloy. The accuracy of these results was shown by comparison with prior experimental results. For the first time we have demonstrated the viability of the oscillating drop technique in the measurement of the surface tension of

liquid metals. We have also demonstrated the advantages and unique possibilities offered by microgravity experimentation and the power of mathematical modeling in planning and replanning very complex processes.

We have shown that the measurement of the surface tension of liquid metals in microgravity using the oscillating drop technique with electromagnetic levitation is extremely accurate. The data for gold are in excellent agreement with those obtained in earthbound experiments and with expected results and shows that we can eliminate the need for correction formulae to account for the applied magnetic field by performing the experiments in microgravity. The agreement between the microgravity data and the corrected data from earthbound experiments also shows that the correction formula accurately accounts for the effects of the magnetic field and sample mass. The data for gold-copper very closely follow the predictions of the ideal solution model for the surface tension of alloy melts. Data points in the undercooled regime were obtained for zirconium-nickel and the values are between the surface tension values for pure zirconium and pure nickel.

We have demonstrated the ability to perform accurate thermophysical property measurements with TEMPUS. Furthermore, if TEMPUS is given another opportunity to fly with a Spacelab mission, the results already obtained suggest that it will be possible to make accurate measurements of the surface tension of deeply undercooled metals.

6.6 DYNAMIC NUCLEATION

The coincidence of the 3.5 V (130 A) heating coil pulse and recalescence in cycle 6 of the $Zr_{64}Ni_{36}$ experiment can be seen in Figure 6.2. This phenomenon occurred during many cycles of the experiment, suggesting that the pulses may have triggered nucleation without any contact with the sample. Experimental evidence and theoretical arguments concerning dynamic nucleation in undercooled liquids does exist [19-21].

One possible explanation for the dynamic nucleation that is presented is a change in melting temperature ΔT_m with pressure ΔP, which is quantified by the Clapeyron equation [20]

$$\Delta T_m = \frac{T\Delta V}{\Delta H}\Delta P \tag{6.10}$$

where ΔV and ΔH are the volume and enthalpy changes on melting and T is the absolute temperature. The pressure required to change the melting point in liquid metals enough to trigger nucleation is many orders of magnitude greater than the magnetic pressure of 420 Pa exerted on the undercooled liquid sample by the 3.5 V heating coil pulse. The publications on the subject of dynamic nucleation [19-21] suggest that the collapse of small bubbles created by cavitation in the liquid was responsible for the change in melting point sufficient to cause nucleation. Frawley and Childs [21] achieved dynamic nucleation by what they termed acoustical cavitation in undercooled bismuth with 20,000 cps vibrations.

Given the heating coil frequency of approximately 400 kHz used in TEMPUS, acoustical cavitation could have caused nucleation in the ZrNi sample. However, the molten sample is always subject to a positioning coil field of frequency 144 kHz and a heating coil field of lower magnitude than that provided by the heating coil pulse. Another important consideration is that undercoolings of several hundred degrees have been obtained in metal droplets levitated in AC fields in the same frequency range on earth without the occurrence of dynamic nucleation. Confirmation of the dynamic nucleation events during the IML-2 experiment and the possible mechanisms if the phenomenon did occur require further study.

6.7 ACKNOWLEDGEMENTS

The authors acknowledge the cooperation and efforts of the TEMPUS Team, in particular, Prof. Hans Fecht of the Technical University in Berlin for the use of his ZrNi sample. The authors gratefully acknowledge NASA and DARA for their financial support and for the opportunity to perform the microgravity experiments.

6.8 REFERENCES

[1] R. P. Chhabra and D. P. Sheth, "Viscosity of Molten Metals and its Temperature Dependence", Zeitschrift fuer Metallkunde, 81 (1990), 264-271.

[2] J. L. Margrave, "Determination of thermophysical properties of liquid metals at high temperatures by levitation methods", Materials Science and Engineering, A178 (1994), 83-88.

[3] S. Sauerland, Messung der Oberflaechenspannung an levitierten fluessigen Metalltropfen, Ph.D. Thesis, DLR Cologne/University of Aachen, Germany (1993).

[4] S. Sauerland, G. Lohoefer, and I. Egry, "Surface tension measurements on levitated liquid metal drops", Journal of Non-Crystalline Solids, 156-158 (1993), 833-836.

[5] I. Egry, "On the Relation between Surface Tension and Viscosity for Liquid Metals", Scripta Metallurgica et Materialia, 28 (1993), 1273-1276.

[6] W. H. Reid, "The Oscillations of a Viscous Liquid Drop", Quarterly of Applied Mathematics, 18 (1960), 86-89.

[7] D. L. Cummings and D. A. Blackburn, "Oscillations of magnetically levitated aspherical droplets", Journal of Fluid Mechanics, 224 (1991), 395-416.

[8] S. Sauerland, R. F. Brooks, I. Egry, and K. Mills, "Magnetic Field Effects on the Oscillation Spectrum of Levitated Drops", Containerless Processing: Techniques and Applications, TMS, Denver (1993), 65-69.

[9] S. Sauerland, G. Lohoefer, and I. Egry, "Surface Tension Measurements on Levitated Aspherical Liquid Nickel Drops", 11th Symposium on Thermophysical Properties, Boulder, Colorado, 1991.

[10] I. Egry and J. Szekely, "The Measurement of Thermophysical Properties in Microgravity using Electromagnetic Levitation", Adv. Space Res., 11(7) (1991), 263-266.

[11] I. Egry, "Surface tension measurements of liquid metals by the oscillating drop technique", Journal of Materials Science, 26 (1991), 2997-3003.

[12] Team TEMPUS, "Materials Sciences on IML-2: The results of the TEMPUS Team", to be published.

[13] J. W. S. Rayleigh, "On the Capillary Phenomena of Jets", Proceedings of the Royal Society of London, 29 (1879), 71-97.

[14] S. Sauerland, K. Eckler, and I. Egry, "High-precision surface tension measurements on levitated aspherical liquid nickel droplets by digital image processing", Journal of Materials Science Letters, 11 (1992), 330-333.

[15] B. J. Keene, "Review of data for the surface tension of pure metals", International Materials Reviews, 38(4) (1993), 157-192.

[16] S. H. Avner, Introduction to Physical Metallurgy, 2nd ed., McGraw-Hill Book Company, New York, 1974.

[17] E. Gorges, unpublished.

[18] B. Gallois and C. H. P. Lupis, "Surface Tensions of Liquid Ag-Au-Cu Alloys", Metallurgical Transactions, 12B (1981), 679-689.

[19] B. Chalmers, "Dynamic Nucleation", Liquids: Structures, Properties, Solid Interactions, T. Hughes, ed., Elsevier, 1965, 308-325.

[20] J. D. Hunt and K. A. Jackson, "Nucleation of Solid in an Undercooled Liquid by Cavitation", Journal of Applied Physics, 37(1) (1966), 254-257.

[21] J. J. Frawley and W. J. Childs, "Dynamic Nucleation of Supercooled Metals", Transactions of the Metallurgical Society of AIME, 242 (1968), 256-263.

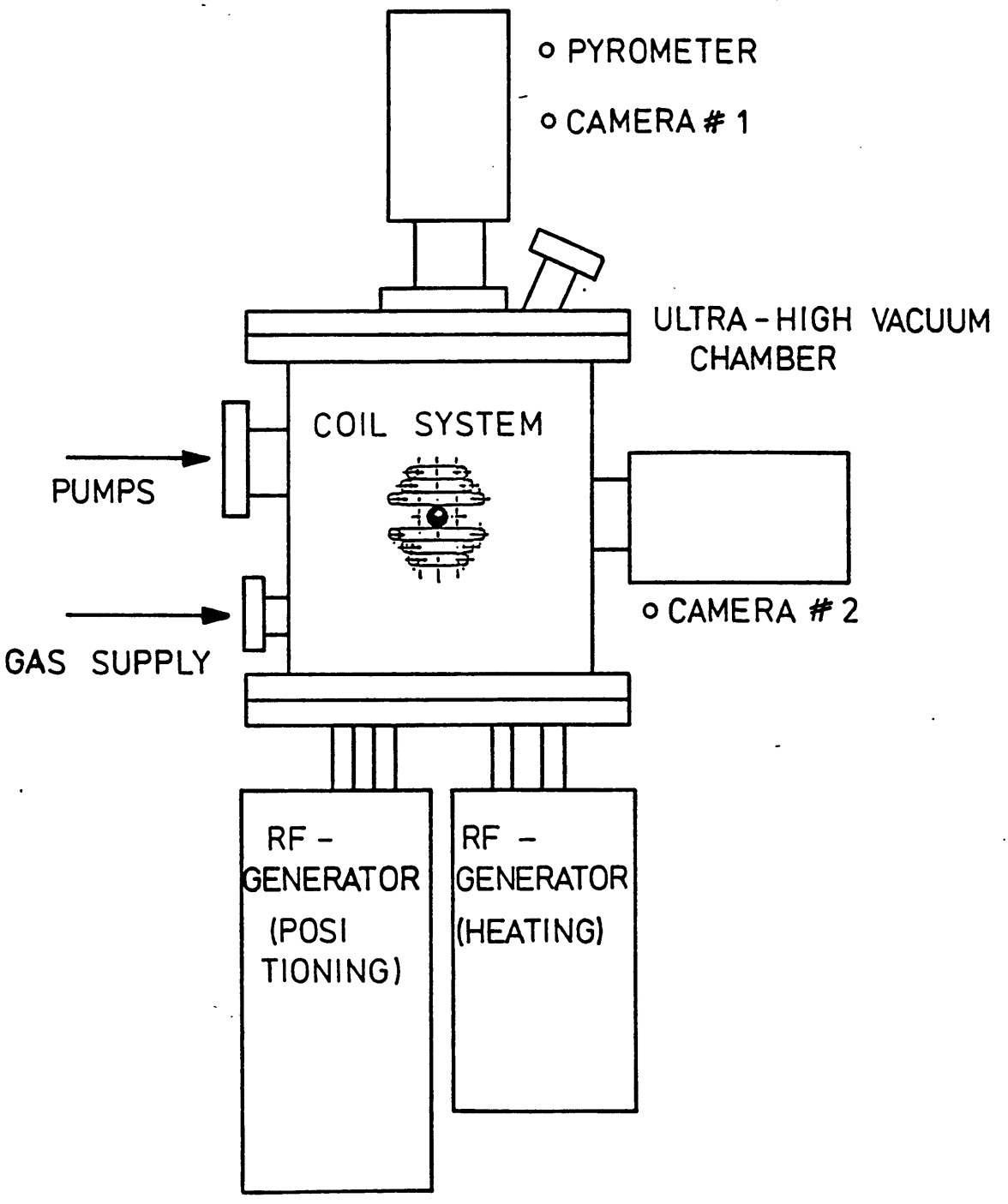

Figure 6.1 Schematic sketch of the TEMPUS experimental arrangement showing main subsystems.

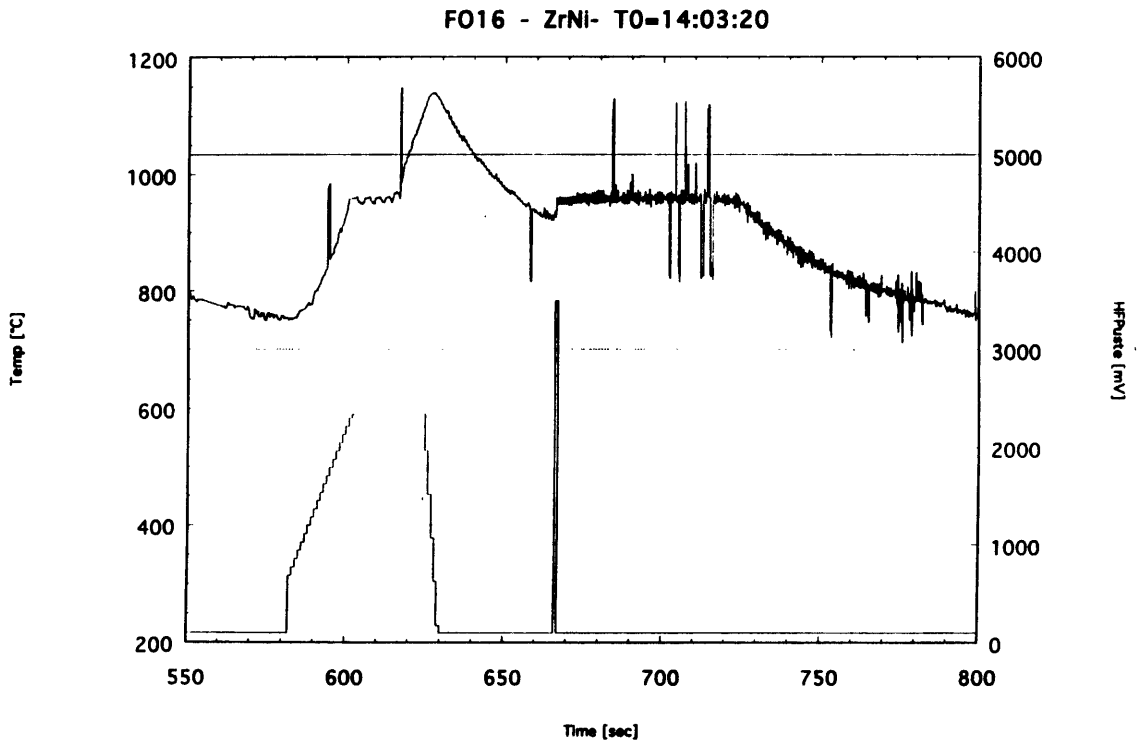

Figure 6.2 Plot of temperature (jagged line), heating coil control voltage (plot at bottom), and positioning coil control voltage (constant value of 5000 mV) vs. time for cycle 6 of $Zr_{64}Ni_{36}$ experiment.

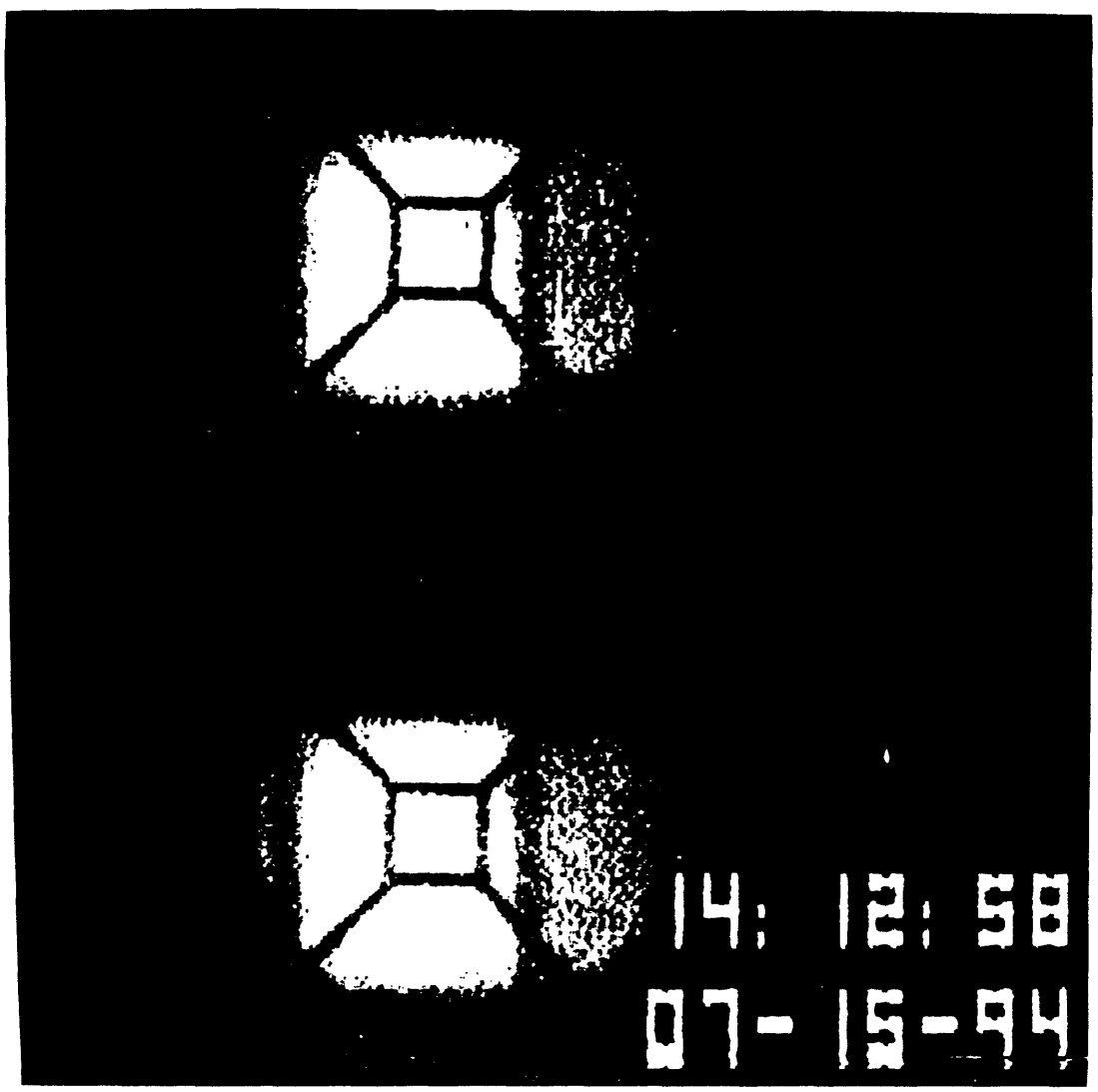

Figure 6.3 Video still of two frames of the side view of the oscillating $Zr_{64}Ni_{36}$ droplet. The visible portion of the droplet is flat at the top and the bottom because of the obstruction provided by the heating coils. The obstruction from the sample cage wires causes the vertical lines. The cross hairs come from the camera.

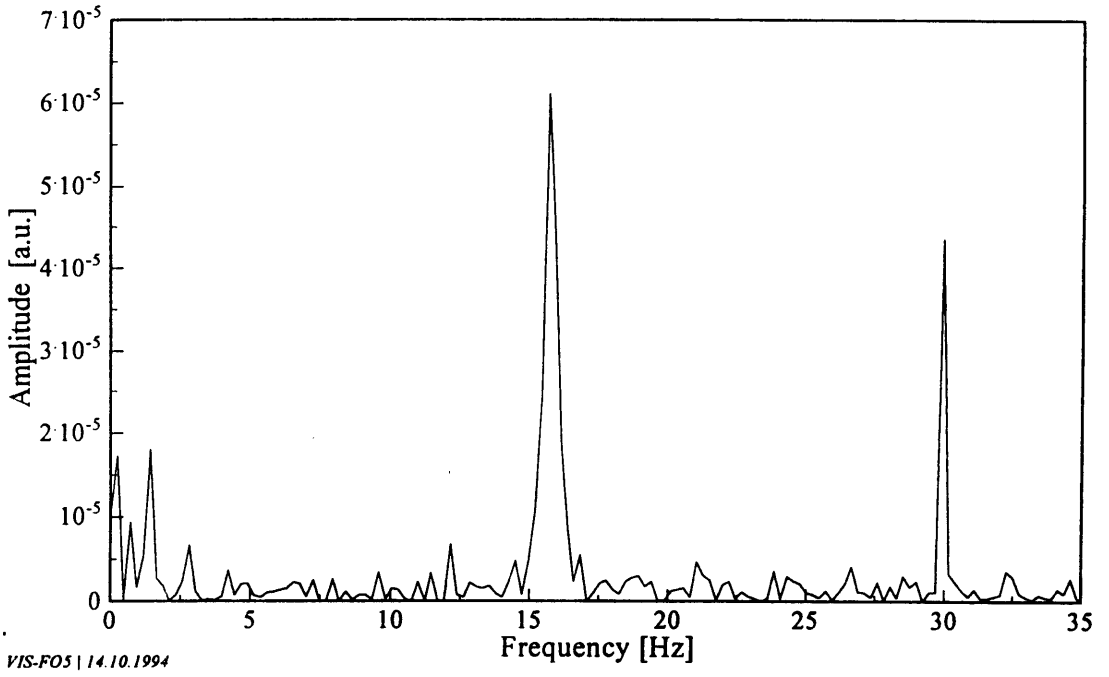

Figure 6.4 Frequency spectrum for surface tension measurement of $Au_{56}Cu_{44}$. The peaks in the region of 0-5 Hz come from translational oscillations. The high peak at about 15 Hz is the surface oscillation peak used to measure the surface tension. The peak at 30 Hz comes from the commercial frame rate.

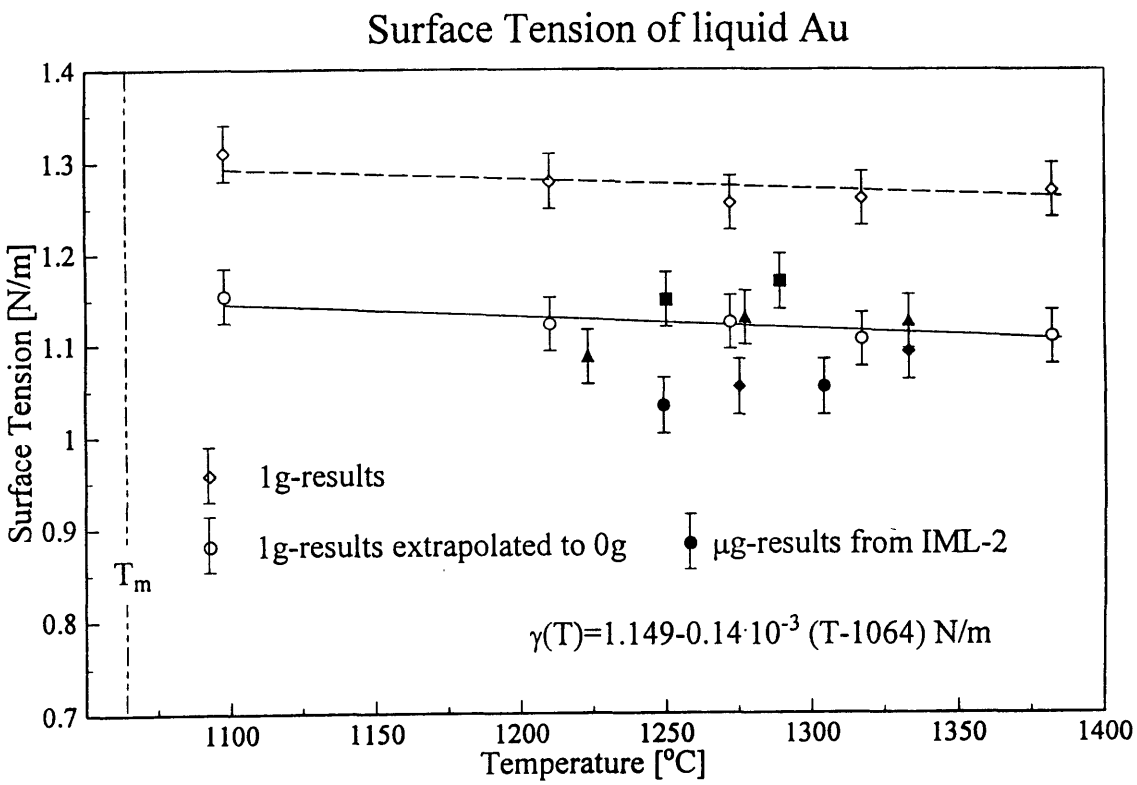

Figure 6.5 Surface tension data for liquid Au, with linear fit of the data points. For the purpose of comparison, the "1 g-results" are uncorrected data obtained by Sauerland et al. [15] in earthbound levitation experiments. The "1 g-results extrapolated to 0 g" are surface tension values obtained using the Cummings and Blackburn correction formula.

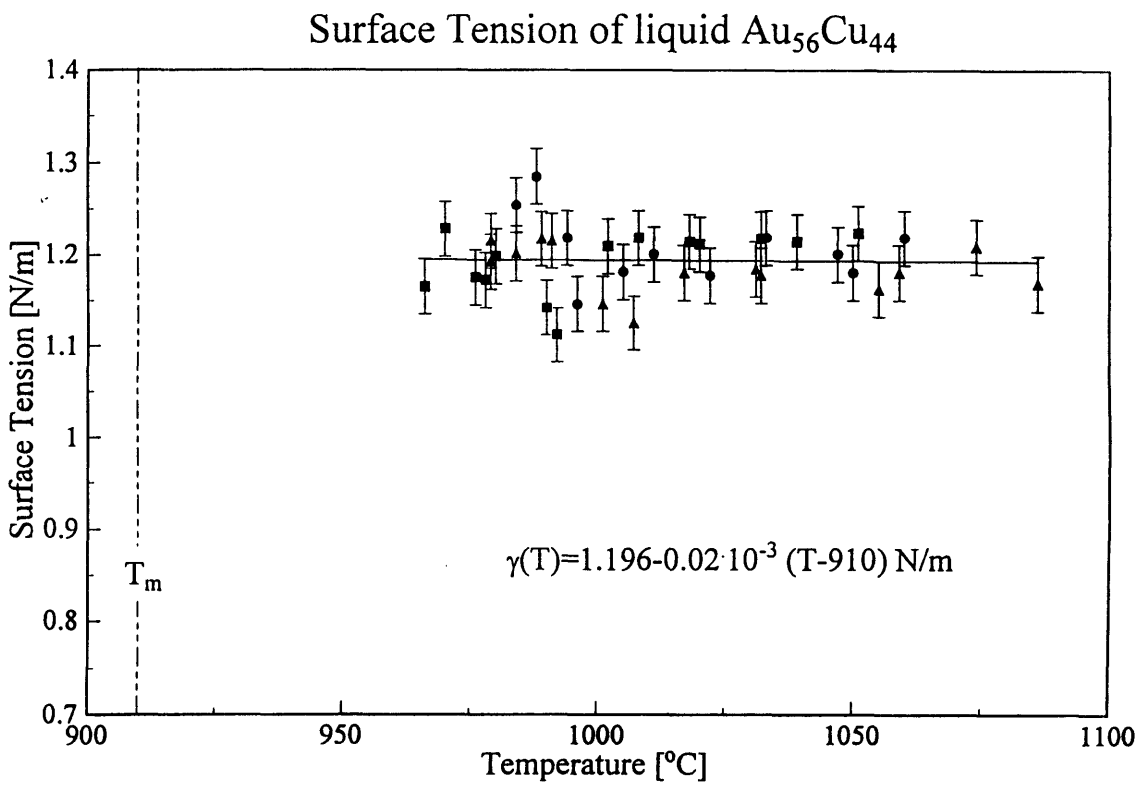

Figure 6.6 Surface tension data for liquid $Au_{56}Cu_{44}$, with linear fit of the data points.

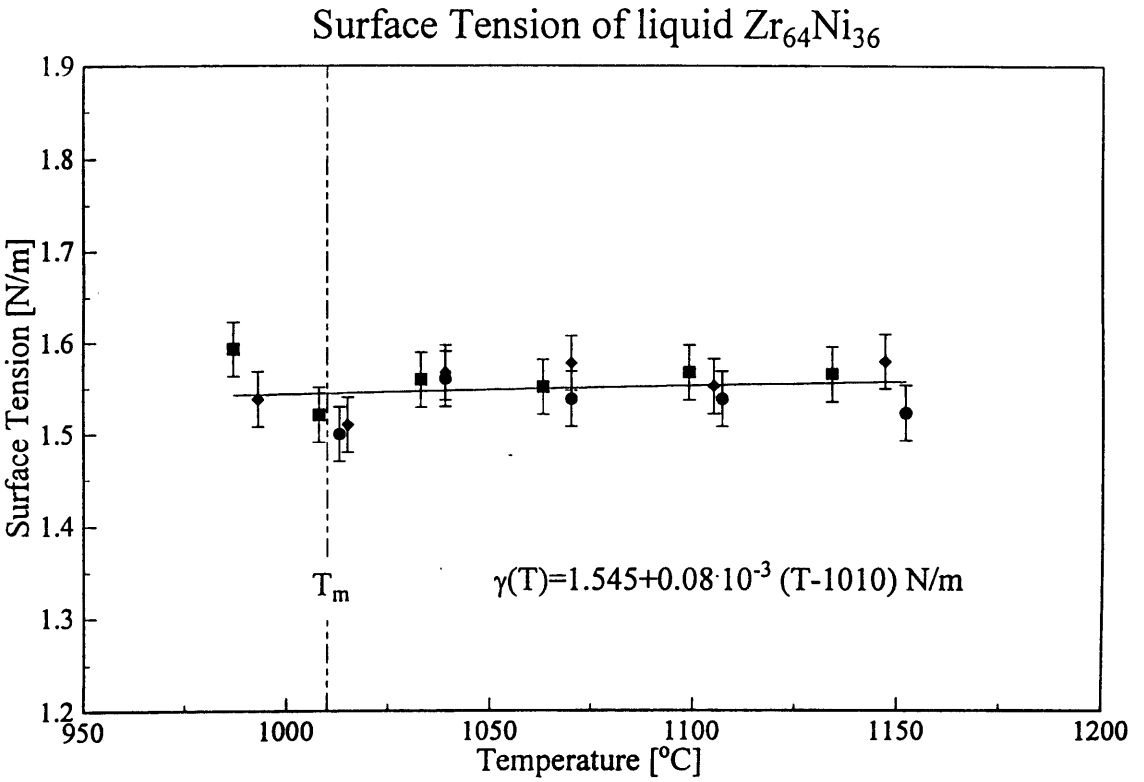

Figure 6.7 Surface tension data for liquid $Zr_{64}Ni_{36}$, with linear fit of the data points.

CHAPTER 7

CONCLUDING REMARKS

The most important achievement of this work is the development of a computational methodology that was used to design a series of successful Space Shuttle experiments to measure the viscosity and surface tension of superheated and undercooled melts. Specifically, the following phenomena have been modeled using both self-developed codes and adapted commercial software packages:

- Electromagnetic forces and induced power
- Free surface deformation without fluid flow considered
- Free surface deformation considering internal fluid flow
- Heat transfer

Electromagnetic Forces and Induced Power

Calculation of the electromagnetic phenomena in an axisymmetric sample of arbitrary cross section in a rotationally symmetric coil system made it possible to calculate the magnetic pressure exerted on the free surface, the lifting and stirring forces, and the induced power (Joule heating) in the sample. The accuracy of the formulation was confirmed by comparison of the total lifting force with experimental results, testing with the case of a spherical coil, the classical "flux ball", and comparison of the total power induced in a spherical sample with analytical results. Precise calculation of the local distribution of electromagnetic quantities had not been done prior to the work presented in this thesis.

Free Surface Deformation Without Fluid Flow Considered

The mathematical model of the free surface shape considering magnetic pressure, surface tension, hydrostatic pressure, and gravity at the surface of the sample was used to determine the heating coil voltage needed to effect the desired extent of sample deformation. The accuracy of the formulation was confirmed by comparison of calculated shapes with the shapes of droplets in earthbound levitation experiments and by the fact that the droplets processed in microgravity were in fact deformed to the prescribed extent.

Free Surface Deformation Considering Internal Fluid Flow

In order to improve upon the model of the free surface shape, we developed a model that considered free surface deformation and internal fluid flow simultaneously. Because of the difficulty associated with treating the position of the free surface as an unknown in the solution of the Navier-Stokes equations to calculate the internal fluid flow field, previous models of the shape of levitated droplets concentrated on the phenomena at the surface and neglected the interior. The accuracy of the model of the free surface shape was confirmed by comparison with the same earthbound experimental results. It was not possible to quantitatively confirm the calculation of the internal fluid flow field, but the flow pattern was qualitatively confirmed by comparison with the path of oxygen particles in a molten iron droplet.

Heat Transfer

The temperature distribution in levitated liquid metal droplets was modeled by considering the conduction within the sample, the induced power distributed throughout the sample, and the temperature-dependent heat losses by radiation and conduction at the surface. With this work it was possible to confirm that the temperature gradients in the samples processed in the microgravity experiments would be negligible, assuring the accuracy of temperature measurement at the sample surface and eliminating concern about surface tension-driven fluid flow. The accuracy of the model was confirmed by comparison of the calculated results with relatively simple analytical calculations.

It is important to reiterate that the mathematical modeling effort culminated in a successful series of microgravity experiments. Some experiments were performed successfully based on the extensive preparation and mathematical modeling before the mission, while other experiments were planned entirely during the mission based on experience and understanding of the key phenomena gained from mathematical modeling. At the time of the submission of this thesis, surface tension values had been obtained and the possible proof of the phenomenon of dynamic nucleation had been achieved. While viscosity results had not yet been attained, simulations based on the mathematical models presented in this thesis were being used as a significant part of the effort to extract viscosity results from the experiment data.

A methodology for the rational design of experiments in a microgravity environment based on mathematical modeling of the levitation forces, electromagnetically-driven flows, deformation, and heat transfer was presented in this thesis. Many of the calculations made using the models developed were validated by ground-based experiments, but the ultimate confirmation of the usefulness of the models was provided by the successful Space Shuttle experiments.

The successful microgravity experiments demonstrated the power of mathematical modeling of materials processes. Mathematical modeling provides quantitative understanding of the key physical phenomena and is much less expensive than trial-and-error experimentation. In addition to facilitating the success of microgravity experiments, the power of mathematical modeling suggests that it could be used to design experiments that could be performed on the ground rather than in space. Given the prohibitive cost of microgravity experiments and the lack of flight opportunities, mathematical modeling should be used as much as possible to find ways of performing experiments without going to space.

The techniques developed for modeling the behavior of levitation-melted metallic droplets could be readily adapted to a broad range of problems where metallic surfaces are being shaped, deformed, or simply held in position though the application of electromagnetic forces; some current applications of these techniques include electromagnetic casting, electromagnetic dams in near net shape casting operations, and the moldless melting of titanium. While major advances are being made in the application of electromagnetic theory to advancing our understanding of these systems, it is possible that the techniques described here could find applications in these areas as well.

The comprehensive MHD model of the free surface shape and electromagnetically-driven flow in a levitated droplet is a ready example. A model which considers only the surface is sufficient to model the free surface shape when the electromagnetic skin depth is much smaller than the sample dimensions, as with a large pool of molten metal subjected to electromagnetic forces. However, in cases where the ratio of skin depth to the sample dimensions is larger, as in meniscus control in electromagnetic casting and

electromagnetic shape control of liquid metal jets, the interior of the droplet must be considered. The ratio of the skin depth to the characteristic length has been identified as the key parameter in determining when the free surface shape and the internal fluid flow must be calculated simultaneously.

The most glaring need in the mathematical modeling of electromagnetic shaping and electromagnetically-driven flow is in the area of turbulence modeling. In fact, the various zero-equation, two-equation, and other turbulence models which exist are not appropriate for a recirculating flow pattern that is bounded entirely by a free surface. In order to be able to develop fully comprehensive models of the fluid flow, free surface shape, and heat transfer in electromagnetic levitation experiments and processes involving electromagnetic shaping, the calculation of the internal fluid flow pattern is required. Various research groups are working on the simulation of such complex turbulent flows. Two approaches that are being developed are large eddy simulations, which still involve averaging over a finite volume, and direct numerical simulation of turbulence. The Materials Process Modeling Group, specifically Mr. Robert Hyers and Prof. Szekely, is developing a solver based on the direct numerical simulation of turbulence. With the great advances in computation that have been made in the last few years, such as the emergence of parallel computing, this approach offers great possibilities.

BIOGRAPHICAL NOTE

Elliot Schwartz was born on April 26, 1967, in Brooklyn, New York, to Yvette and Gordon Schwartz. He attended elementary school at Raritan Valley School in Hazlet, New Jersey, where he was the valedictorian. He graduated from Raritan High School, Hazlet, New Jersey, as valedictorian of the class of 1985. He graduated in 1989 from MIT with Bachelor of Science degrees in both Materials Science and Engineering and Mathematics, with an option in applied mathematics.

With the financial support of the National Defense Science and Engineering Graduate Fellowship, he began his graduate studies in the Department of Materials Science and Engineering at MIT in the fall semester of 1989 under the supervision of Professor Julian Szekely. He served as the teaching assistant for the undergraduate course "Transport Phenomena in Materials Engineering", during the fall semester of 1990, and subsequently received the John Wulff Award for excellence in teaching from the Department of Materials Science and Engineering.

As a graduate student, he also served as a tutor for various engineering courses with the Office of Minority Education and as a graduate resident/tutor at 500 Memorial Drive (Next House), an undergraduate dormitory at MIT. He received the Karl Taylor Compton Prize from MIT in 1993 "in recognition of outstanding contributions in promoting high standards of achievement and good citizenship within the MIT community".

After completing his studies at MIT, he will work as a Postdoctoral Research Associate in the Materials Technology: Metallurgy group at Los Alamos National Laboratory in New Mexico.